Cavitation and Heat Transfer Over Micro Pin Fins

2019

Arash Nayebzadeh
University of Central Florida

University of
**Central
Florida**

STARS
Showcase of Text, Archives, Research & Scholarship

CAVITATION AND HEAT TRANSFER OVER MICRO PIN FINS

by

ARASH NAYEBZADEH

M.Sc. University of Central Florida, 2015

M.Sc. Sharif University of Technology, 2008

B.Sc. Amirkabir University of Technology, 2005

A dissertation submitted in partial fulfillment of the requirements
for the degree of Doctor of Philosophy
in the Department of Mechanical and Aerospace Engineering
in the College of Engineering and Computer Sciences
at the University of Central Florida
Orlando, Florida

Summer Term

2019

Major Professor: Yoav Peles

ABSTRACT

With the dramatic increase in the usage of compact yet more powerful electronic devices, advanced cooling technologies are required to maintain delicate electronic components below their maximum allowable temperatures and prevent them from failure. One solution is to use innovative pin finned heat sinks. This research is centered on the evaluation of hydrodynamic cavitation properties downstream pin fins and extended toward single-phase heat transfer enhancement of array of pin fins in microchannel.

In this work, transparent micro-devices capable of local wall temperature measurements were micro fabricated and tested. Various experimental methods, numerical modeling and advanced data processing techniques are presented. Careful study over cavitation phenomena and heat transfer measurement downstream pin fins were performed.

Hydrodynamic cavitation downstream a range of micro pillar geometries entrenched in a microchannel were studied. Three modes of cavitation inception were observed and key parameters of cavitation processes, such as cavity length and angle of attachment, were compared among various micro pillar geometries. Cavity angle of attachments were predominantly related to the shape of the micro pillar. Fast Fourier transformation (FFT) analysis of the cavity image intensity revealed transverse cavity shedding frequencies in various geometries and provided an estimation for vortex shedding frequencies.

Experimental and numerical heat transfer studies over array of pin fins were carried out to find out the influence of lateral interactions of fluid flow on the enhancement of heat transfer. Local temperature measurements combined with a conjugate fluid flow and heat transfer modeling revealed the underlying heat transfer mechanisms over pin fin arrays.

To:

My wife, Hanieh

My daughter, Eva

ACKNOWLEDGEMENT

I sincerely thank my advisor, Prof. Peles for his patience, support and knowledge. He has been playing a key role in shaping my academic career.

My committee members at UCF; Prof. Louis Chow, Prof. Alain Kassab, and at RPI Prof. Joel Plawsky were very supportive through the course of my PhD. I thank them for their feedback about my research plan and my dissertation.

I am very fortunate to have a great network of friends. Thanks to my friends from Amirkabir, Sharif and UCF. Also a thank you to all my lab-mates at UCF, for their help and support over these years.

A special thank you to Hanieh, my better half and lab mate; your constant emotional and intellectual support and help made the entire journey far easier.

I would like to thank my little daughter, Eva; your birth is the most amazing event in my entire life. I can't thank you enough as you made me a better person.

TABLES OF CONTENTS

LIST OF FIGURES

LIST OF TABLES

LIST OF ACRONYMS/ABBREVIATIONS

C_p= Pin fin pressure coefficient based on P_{pf} and $\bar{V}_p$

$C_{p,Min.}$= Pin fin minimum pressure coefficient

D = Pin fin diameter (m)

D_h = Microchannel hydraulics diameter

L= Pin fin length (m)

$L_{c,Max.}$= Maximum length of cavity (m)

AR = Aspect ratio(L/D)

P_1= Average microchannel inlet pressure (Pa)

P_2= Average microchannel outlet pressure (Pa)

P_{in}= Pressure measured by upstream transducer (Pa)

P_{out}= Pressure measured by downstream transducer (Pa)

P_{mc} = Pin fin upstream pressure (Pa)

P_{pf} = pin fin pressure measured at the center of pin fin (Pa)

P_v = Vapor pressure of water (Pa)

$\bar{V}$ = Mean pin fin upstream velocity (m/s)

$\bar{V}_p$ = Mean velocity between pin fin and sidewalls area (m/s)

W = Microchannel width (m)

$W_{c,Max.}$= Maximum width of cavity (m)

r = Confinement ratio(D/W)

t = time (s)

Re = Reynolds number based on $\bar{V}$ and channel hydraulic diameter

- Greek letters

Δ = Distance between pin fin center and adjacent wall (m)

ρ = Water density (kg/m^3)

γ = Gap parameter (Δ/D)

σ_i = Cavitation inception number based on P_{pf} and $\bar{V}_p$

θ = Angle measured clockwise from upstream stagnation point on pin fin (degree)

$\theta_{Cav.}$ = Cavitation angle (degree)

$\theta_{C_{p,Min.}}$ = Angle at which $C_{p,Min.}$ occurs

$\theta_{Sep.}$ = Angle at which separation occurs

1. INTRODUCTION

Nowadays, microfluidic systems have been utilized widely in various industries such as electronic cooling, drug delivery, lab on a chip, waste water treatment, biotechnology and biodiesel to name a few. Owing to the rapid advancement in material science combined with the incorporation of new microfabrication techniques, an exponential growth in the usage of such systems has been witnessed. The dramatic increase in the usage of compact yet more powerful electronic devices necessitates the realization of advanced cooling technologies to maintain electronic components below their allowable temperature and prevent from failure.

Research on heat sinks for the purpose of electronics cooling has suggested the capability of micro pin fins to dissipate higher heat fluxes. Concurrently, a plethora of research focus has been directed toward introducing two phase flow as a promising strategy to enhance heat transfer and dissipate high heat fluxes. Interestingly, two phase flow can be present in the form of hydrodynamic cavitation behind micro pin fins at favorable flow conditions. The first purpose of this study aims at developing fundamental knowledge in the context of hydrodynamic cavitation behind micro pins at microchannel and assessing its probable consequences in the flow field. The next goal is to find out the effect of lateral configuration of pin fin array on the heat transfer enhancement.

1.1. Cavitation

Phase change from liquid to vapor can take place mainly due to two well-known thermodynamic phenomena — boiling and cavitation (Figure 1). Exerting superheat condition at constant pressure by increasing the temperature to a value above the liquid saturation temperature is called boiling. On the other hand, the process of rupturing liquid by decreasing its pressure at constant temperature is known as cavitation. Any decrease in local pressure of fluid to the extent that it gets close to the fluid vapor pressure may lead to the production of cavitation bubbles.

Liquid vapor pressure (P_v) serves as an important fluid property in cavitation studies as the regions susceptible to cavitation have pressures close to the vapor pressure. To quantify cavitation conditions, a non-dimensional parameter termed cavitation number is defined according to:

$$\sigma = \frac{P_\infty - P_v}{\frac{1}{2}\rho_\infty V_\infty^2} \tag{1}$$
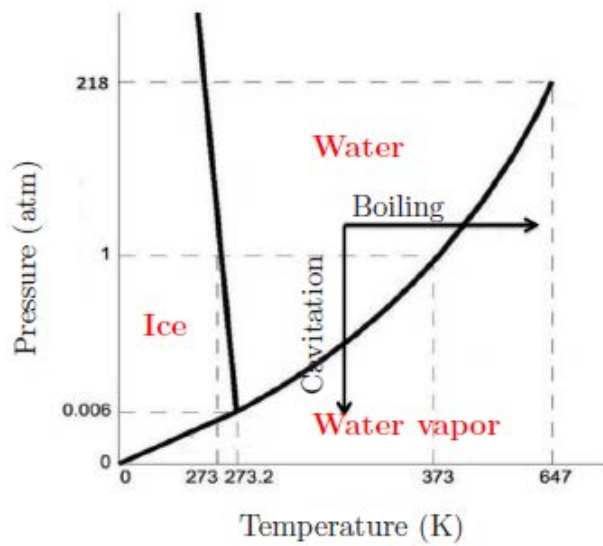
Figure 1: Phase diagram of water depicting different thermodynamic paths for boiling and cavitation [1]

where P_∞ is the free stream pressure, P_v is the liquid vapor pressure, ρ_∞ is the liquid density, and V_∞ is the free stream velocity. This number is widely employed to dynamically quantify cavitation conditions and their intensity. In several studies, such as [2,3], the initial appearance of rapid-moving bubbles followed by sporadic appearance and disappearance of bubbles was defined as cavitation inception. The value of cavitation number when the first bubbles of cavitation initiate is called cavitation inception number (σ_i).

1.1.1. **Classification of cavitation**

A common way to characterize cavitation is to consider how it forms in the flow domain. From this perspective, cavitation can be categorized into four types: hydrodynamic, acoustic, optic, and particle cavitation. Hydrodynamic cavitation is caused by local pressure variation due to changes in the geometry of fluid path. Utilization of acoustics in the field of fluid mechanics emerged primarily with reference to sonar systems; when a travelling high intensity sound wave affects liquid, acoustic cavitation may occur. Local energy deposition by high intensity photons (laser pulse) and charged particles can also produce optic and particle cavitation, respectively.

1.1.1.1. Hydrodynamic cavitation

Hydrodynamic cavitation is often being recognized as an unfavorable phenomenon that can take place in any fluid-handling device causing a range of adverse effects, such as reduced efficiency, decreased power output, vibration, noise, surge stall, and erosion in hydraulics machineries. At the conventional scales numerous studies have been devoted to identify, characterize, and predict cavitation in an effort to prevent its undesirable effects. Studies demonstrated that cavitation can also occur at the micro scale causing damage to silicon surfaces and limiting the performance and operability of micro machines.

In this thesis, hydrodynamic cavitation will be under investigation. Within hydrodynamic cavitation context, three major cavitation types can be classified as follows: travelling, fixed and vortex cavitation [1,4]. This classification is based on the origin of low pressure regions and the behavior of cavity in the fluid flow. A brief description of various hydrodynamic cavitation types is presented in the following.

1.1.1.2. Traveling cavitation

Traveling cavitation occurs when cavity pockets or bubbles form in a liquid and travel along the flow stream (Figure 2). During this transient process, cavity pockets and bubbles may expand when subjected to low pressure regions and collapse when reaching to high pressure regions. Transition from sheet cavity (fixed)

to cloud cavity in the leading edge vicinity of hydrofoil is an example of travelling cavitation in which a portion of attached sheet cavity can break into a vapor cloud and travel along the flow.
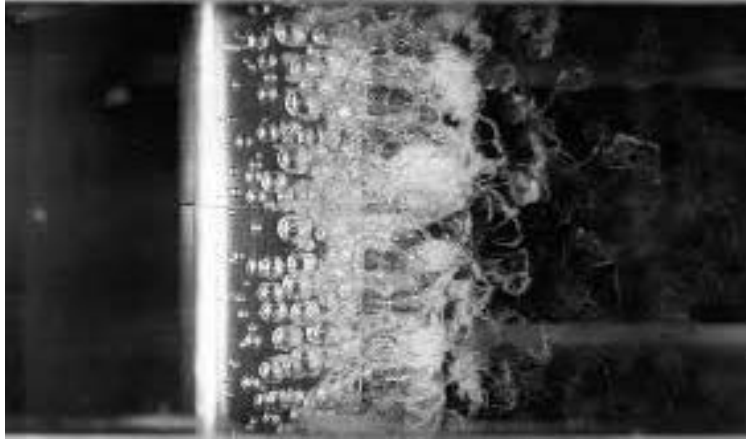
Figure 2: Travelling bubble cavitation on the surface of NACA 4412 hydrofoil at zero angle of attack. The flow is from left to right [2]

1.1.1.3. Fixed cavitation

In a flow stream, when vapor cavity stays attached to nearby rigid body, fixed cavity forms. In some circumstances, the vapor cavity in the liquid interface may pulsate, but the location at which the cavity is attached to a solid structure remained unchanged, thus the entire cavity volume has negligible variation. Sheet cavity is a common illustration of fixed cavitation that forms in hydrofoils (Figure 3). For bluff bodies (Figure 4), the wake region is often filled by vapor-like cavitation called "attached" or "fully developed" cavity [2].
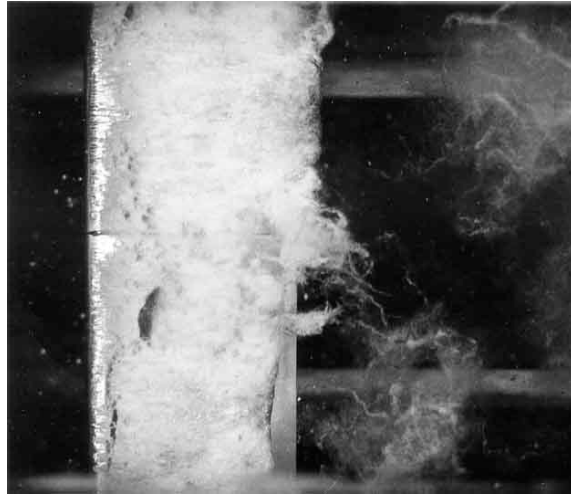
Figure 3: Sheet cavitation on the suction side of a NACA 4412 hydrofoil, the flow is from left to right [2]
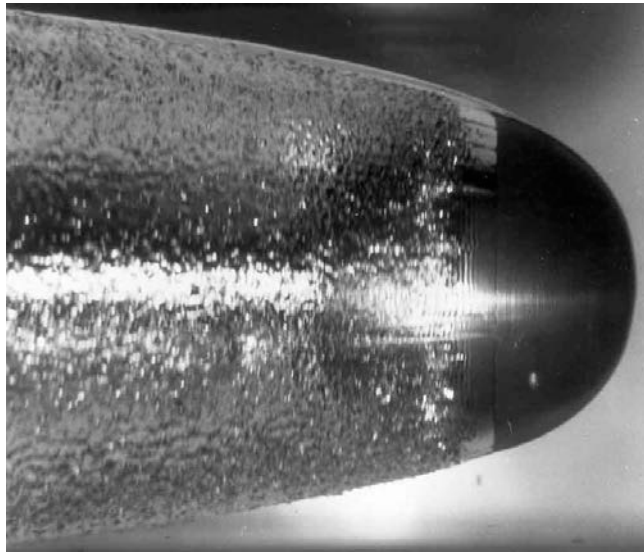
Figure 4: Fully developed cavitation formation behind a 7.62 cm diameter sphere, the flow is from right to left [2]

Vortex cavitation

Another form of hydrodynamic cavitation occurs in the vortex core regions where pressure is substantially lower than nearby area [5]. Tip vortex cavitation at the tip of rotating propeller [2], vortex cavitation along the leading edge of delta hydrofoils (Figure 5), [6], cavitation formed in the vortex cores in turbulent shear layers ,(Figure 6), and finally cavitation at Karman shedding vortices behind bluff bodies are the main

examples of vortex cavitation. This type of cavitation along with fixed cavity will be discussed in detail throughout this dissertation.

(a)   (b)
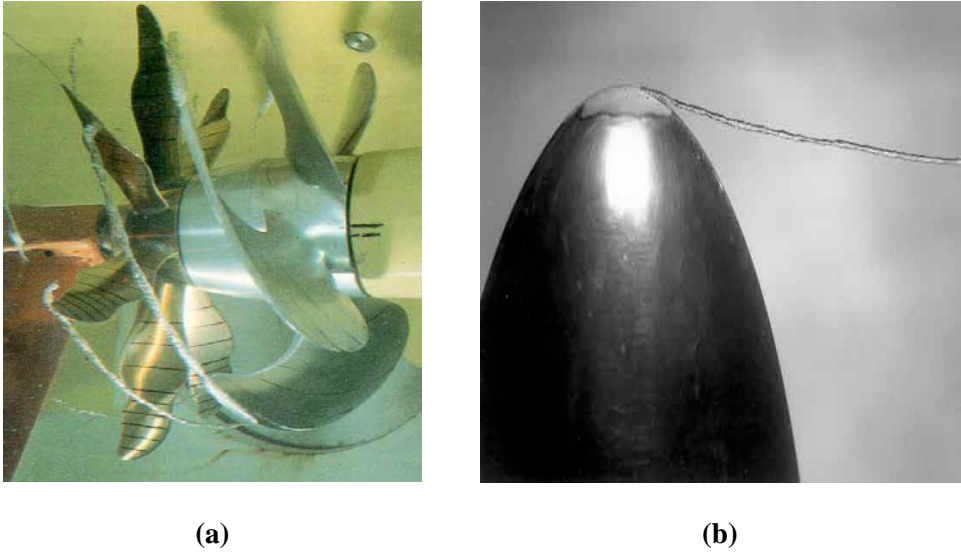
Figure 5: (a) Tip vortices cavitation on a model propeller, (b) Cavitated tip vortices generated by an ellipsoidal planform, the flow is from left to right in both cases [2]
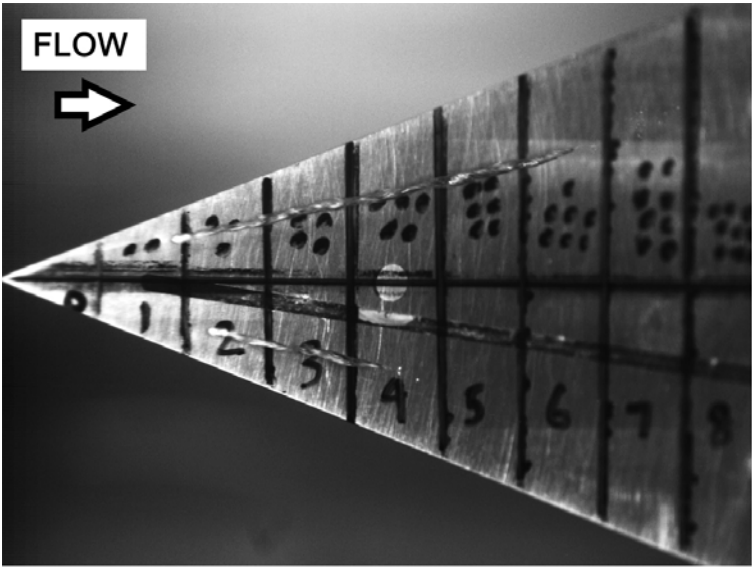
Figure 6: Cavitated vortices on a delta hydrofoil [6]

1.1.2. **Applications of cavitation**

While cavitation is detrimental in many engineering systems, it can be beneficial in others. In electronic cooling applications, cavitation can enhance heat transfer by promoting two-phase flow and leveraging its associated high heat transfer coefficient [7,8]. Cavitation produced behind a micro-orifice in a microchannel can be used to eliminate leukemia cells [9], erode kidney stone [10], and destroy prostate cells [11]. Also, cell membrane disruption [12], intensification of biological wastewater treatment [13–18], food processing [19], and synthesis of biodiesel [20] are some key efforts aimed at utilizing cavitation to enhance chemical mixing within biotechnology/biochemical context. A quick survey in the literature reveals that unlike flow boiling, there are limited studies toward cavitation at the micro scale, whereas abundant applications demand a great deal of fundamental knowledge as to how to characterize its occurrence, control it, and use its potential benefits.

1.1.3. **Scale effects**

Although, the validity of classical fluid mechanics laws for liquids has been proven at the micro scale, appreciable deviations of cavitation in micro domains from the phenomenon in its large scale counterparts indicate the existence of strong scale effects [21–26]. Dominant forces that governs physical phenomena are closely related to the length scale [27]. Body forces are commonly scaled to the third power of the length scale($\propto l^3$), while surface forces and length scale have second power relation($\propto l^2$). Consequently, surface forces often overshadowed body forces as the length scale diminishes [28]. Moreover, it has been proved through experiments that the ratio of body to surface force reaches unity once device dimension is in the vicinity of 1 mm [27], thereby signifying the dominance of surface forces to body forces at such scales. Other factors such as domain shape, Reynolds number, nuclei size and distribution, reduced residence time for bubble growth, type of material used, etc. are key parameters that add more complexity toward relating flow behavior at macro to microscale [29]. For instance, surface tension, which dominates

7

bubble growth [30], is widely affected by surface and free stream nuclei at diminishing scales. A significant delay in the inception of cavitation in micro domains reported by recent studies [3,31] is one of those scale effects. Two factors contribute to this phenomenon: (1) dominance of surface tension effect over vapor pressure in the occurrence of cavitation inception and (2) reduced residence time for bubble growth [32]. It is worth mentioning that viscous effects are known to be very noticeable in conventional cavitation, but because the Reynolds number in high-speed MEMS devices is typically low, another scaling disparity arises in extending cavitation data from conventional scale to microscale. Also, researchers reported unidentified scaling issues in the context of mass and heat transfer that demands further study [28].

1.1.4. **Literature review on cavitation at microscale**

Microfluidics plays a vital role in today's technological advancements in various fields of study [33–38]. Available literature on cavitation in micro domain is limited to micro-hydrofoils, micro-orifices, micro-venturis, and micro-diaphragms. The attempt to explore cavitation in non-conventional domains, albeit in one millimeter scales, was initiated during the micro jet engine project at MIT by [4]. They witnessed the occurrence of cavitation in silicon micro-fabricated turbo pump around 900 µm long chord hydrofoils with working fluids like water and ethanol. They then developed design criteria for microscale turbo pumps and evaluated cavitation influence on micro pump performance. Cavitating flow in micro orifice and in micro venturis entrenched in rectangular silicon microchannel was studied in details by [3,39,40]. They detected various cavitating flow regimes and reported several similarities and deviations between the micro and the macro scales. In particular, they observed low incipient cavitation numbers suggesting a strong scale effect. Medrano et al. conducted experiments on cavitation behind micro venturis and micro diaphragms with deionized water and nanofluids [31,41]. They reported a delay in the onset of cavitation in all of their devices and related it to the metastability of the liquid and lack of wall roughness (i.e., surface nuclei). High-pressure microfluidic systems in the form of T-channel and orifice-channel have been studied by a photo-optical cavitation measurement technique and micro particle image velocimetry *(µPIV)* under

8

pressure drops up to 500 bar and different regimes of hydrodynamic cavitation were characterized [42]. Another effort in the context of characterizing cavitation patterns downstream a cylindrical coaxial orifice has been conducted through high speed imaging and acoustical measurements [43]. More recently, Cioncolini et al. focused on chocked cavitation with circular micro orifice in different geometries and compared their findings with the previous studies in order to find a reliable trend for this type of cavitation [44]. Signal processing techniques, such as fast Fourier transform *(FFT)* by De Giorgi et al. [45] and wavelet decomposition by De Giorgi et al. [46,47], to the pressure and optical signals have been recently carried out in order to detect cavitation regimes in a millimeter-scale cylindrical orifice.

1.1.5. **Flow over short bluff bodies in microchannel**

While flow morphology around conventional free-end bluff bodies and the effect of confinement have always been considered to be classic fluid mechanics problems [48,49], a knowledge gap still exists pertinent to the manner in which small geometries, such as micro pin fins, alter flow behavior inside a microchannel. In the case of a short cylinder confined between a top wall and a bottom wall inside a microchannel, the dynamic of the wake flow is affected mainly by the interaction between the wall shear layer and the pin fin shear layer. Therefore, in addition to the Reynolds number, three other parameters control the wake region: confinement ratio $r = (D/W)$, gap parameter $(\gamma = \Delta/D)$, and aspect ratio $(AR = L/D)$ where D is pin fin diameter, W is channel width, L is channel (pin fin) height and $\varDelta$ is the distance between pin fin center and adjacent wall. Jung et al. [50] used micro particle velocimetry (μPIV) to identify flow patterns behind a bounded circular pin fin with *AR=1.5* centered in a rectangular microchannel with *r = 0.1* and reported a great delay in transition from quasi-steady to unsteady wake flow up to $Re_D = 400$ $(Re_D = \rho \bar{V} D/\mu)$, where ρ is the density of water, $\bar{V}$ is the average upstream velocity in the channel and μ is dynamic viscosity of water. They supported their interpretation by comparing several flow properties like time-averaged and instantaneous velocity filed, vorticity, location of stagnation points, and

turbulent kinetic energy *(TKE)*. Also, shrinkage of the recirculation zone and onset of vortex shedding for $Re_D > 400$ were witnessed.

1.1.6. **Cavitation behind bluff bodies**

As discussed above, available literature provides insight about the nature of cavitation. However, cavitation over other geometries, such as bluff bodies have been received relatively limited attention despite their presence in diverse applications. In recent years, micro pin fins embedded in microchannel have gained considerable attention as a promising passive tools to foster mixing, reduce thermal boundary layer thickness, and enhance heat transfer coefficient [29,51–58]. At certain flow circumstances, the pressure behind a pin fin may reach the vapor pressure of a liquid, giving rise to the emergence of hydrodynamic cavitation. Such cavitating flow could be a potential source of damage and pose limitation to the functionality of the device if supercavitation or choked cavitating flow occurs. Alternatively, cavitation can be exploited as a mean for heat transfer enhancement if thoroughly predicted and controlled. For electronic cooling applications, microchannel-confined pin fins with short aspect ratios and associated flow pattern behind the fin are of great interest.

1.1.7. **Mechanism of cavitation behind bluff bodies**

Cavitation initiation over bluff bodies are majorly influenced by the existence of low pressure regions in the shear layer and also in the shedding vortex cores [2]. Figure 7 illustrates the schematic view of cavitation inception at low Reynolds number flow behind an unconfined circular cylinder (Re is high enough for the existence of vortex shedding) [59]. Low pressures regions form around the cylinder wall in the shear layer. The shear layer then folds up into vortices and under favorable flow condition may lead to the formation of cavitated bubbles in the core of the vortices. The vortices then shed from the bluff body downstream where the recovered pressure is comparatively higher than the region adjacent to the rigid body and as a result, the vapor pockets collapse and generate pressure waves. These pressure waves propagate

10

both upstream and downstream and play a major role in cavitation erosion effect. Occasionally, individual cavitation pockets may merge together and form a large stable vapor cavity. Fry referred to three type of cavitation behind circular cylinder: fixed, cyclic and transitional [60]. Fixed cavity has a similar definition presented previously: attached vapor cavity to rigid body with major pulsations along the flow field. Cyclic cavity refers to periodic shedding from rigid body. Transitional cavity includes both cyclic and fixed cavity.
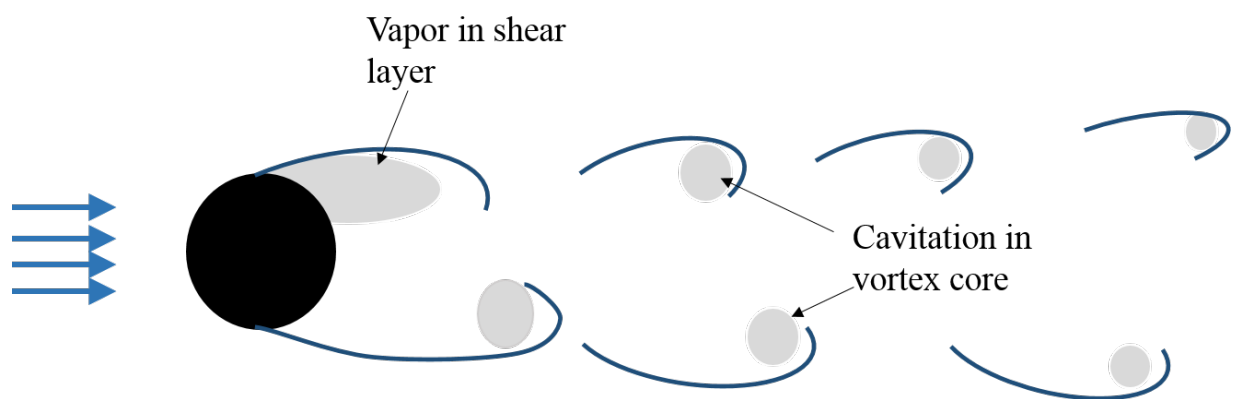
Figure 7: Schematic view of cavitation inception in the presence of vortex shedding in low Re flow over a circular cylinder, reproduced from [59]

1.1.8.   **Literature review on cavitation behind bluff bodies**

In comparison to non-cavitating flow, literature survey reveals relatively fewer studies devoted to flow past bluff bodies in the presence of cavitation. Varga and Sebestyen studied the effects of cavitation number on cavity dimensions and vortex shedding frequency over a circular cylinder for high Reynolds numbers [61]. They measured cavitation noise spectrum to characterize the vapor cavities and also assess cavitation erosion damage. Later, they used acoustic and vibration techniques to distinguish and analysis vortex shedding and cavitation inception frequencies [62]. In a detailed study, Arakeri experimentally studied two axisymmetric bluff body geometries and revealed that laminar boundary layer separation occurred upstream

of cavitation separation [63]. In addition, he proposed a semi-empirical method, although limited to a certain range of Reynolds numbers, for forecasting the location of cavitation separation on smooth-shaped bodies. Rao, and Chandrasekhara characterized cavity length, width and vortex shedding frequency behind circular cylinders in a venturi and evaluated wall effects on the cavity characteristics and vortex shedding [64]. Ramamurthy and Bhaskaran directly measured pressure field to understand the interference effect of wall on drag force and vortex shedding over two-dimensional triangular prisms and circular cylinders [65]. Another study by Fry focused on measuring noise spectra at various distances of cavitation downstream a circular cylinder [60]. The influence of velocity and cavitation number on noise spectra were examined. Matsudaira et al. explored cavitation downstream a circular cylinder and found that the measured high pressure waves in the cavity region were synchronized with the Karman shedding frequency [66]. Tassin Leger et al. utilized two set of sphere and cylinder bluff bodies with hydrophobic and hydrophilic materials and studied the effects of surface energy on cavitation separation and boundary layer separation [67]. A detailed study on cloud cavitation over spherical body carried out by Brandner et al. [68]. They implemented pixel intensity time series data using wavelet analysis for analyzing shedding phenomena and frequency content and reported the appearance of Kelvin-Helmholtz instability at laminar boundary layer. Kumar et al. scrutinized cavitation structure in the near wake of a cylinder using image processing techniques and detected the dominated vortex shedding frequency in the shear layer and also additional frequency peaks corresponding to other regions of flow [69].

1.2.   Heat transfer on pin fin heat sink

Micro pin-fin heat sinks have received much attention in recent years because of their potential to address emerging cooling challenges pertinent to high power electronics [70–73]. They enhance heat transfer through increased surface area and by promoting flow mixing that leads to higher heat transfer coefficients. Additional noticeable applications include hot spots cooling [74–77], concentrated solar cells, fuel cell stacks [78–80], biomedical devices [81,82].

1.2.1.   Literature review on pin fin heat sink

The main focus on the pin fin heat sinks has mainly addressed thermal performance and pressure drop of multi-row arrays of pin fins and employed various fin geometries and array configurations [83–91]. Peles et al. [51] derived a simplified expression for the total thermal resistance and supported their analysis with experimental measurements on a typical silicon micro heat sink with staggered array of circular pin fins. They found that very low thermal resistances are attainable using a pin fin heat sink. A dense pin fin array was suggested to reduce the thermal resistance at high Reynolds numbers while sparse array was found to be effective at low Reynolds numbers. Rasouli et al. [92] experimentally explored the effect of pitch and aspect ratio of diamond-shape pin fins on single-phase heat transfer and fluid flow with PF-5060 at Reynolds numbers (based on pin fin hydraulic diameter) ranging from 8 to 1189. Flow visualizations revealed that unsteady vortex shedding occurred in specific pitch and aspect ratios in which available Nusselt number correlations fail to accurately predict the heat transfer. As a result, a substantial decrease in the Nusselt number dependency on the Prandtl number was reported compared to non-vortex-shedding condition, and new Nusselt number correlations were proposed. Kharangate et al. [93] studied staggered circular pin fins with a diameter of 46.5 µm, height of 110 µm, and longitudinal and transvers pitch, SL and ST, of 100 µm. A heater and resistance temperature detectors (RTDs) were formed on the backside of a silicon substrate to provide heating power and to measure local temperature, respectively. The proposed

Nusselt number and friction factor correlations are in good agreement with previously published results [94]. Tullius et al. [95] conducted an optimization study by varying four parameters including pin fin shape, tip clearance, width/spacing, and material to reveal single-phase laminar flow heat transfer performance. Nusselt number and Darcy friction factor based the numerical modeling were also proposed. Their results suggest that triangular pin fins enhance heat transfer the most, but also tend to increase pressure drop.

In pin fin arrays, several factors such as pin fin density, pitch distances, arrangements etc. have appreciable impacts on fluid flow and heat transfer processes. To disassociate the variables, some of previous efforts [96–99] focused on a single pin fin in a microchannel. Wang et al. identified an important issue to consider in temperature measurements and mitigated it utilizing a combined experimental-*CFD* approach [97]. They evaluated heat transfer mechanism over a single circular pin fin and found that the interplay between flow convection and solid conduction (silicon substrate and pin fin) led to non-uniform heat flux which affected the local heat transfer coefficient.

In pin fin array with several rows, fluid flow is primarily affected by vortical structures occurred downstream of the first row. As the second row prematurely interrupt the flow, such arrangements does not allow to fully examine the undisturbed flow structure and heat transfer process downstream the first row. In addition, most previous studies used conductive material, such as silicon substrate or metal substrate, to study heat transfer processes in micro scale pin fins. In such experimental specimen a great amount of heat is being drawn by conduction process into the solid substrate (heat loss) causing challenges in assessing convective heat transfer mechanism in the vicinity of the pin fins.

2. RESEARCH OBJECTIVE

It is evident from the discussion presented in earlier sections that despite the ever-increasing research demand in the fields of MEMS and microfluidics, studies on hydrodynamic cavitation in micro domain are limited mostly to micro-orifices and micro-venturis. Cavitation as a result of micro scale bluff bodies has not been extensively studied. This dissertation aims to partially fill this research gap by performing experimental, numerical and analytical studies on cavitation downstream micro scale bluff bodies. The heat transfer study in this study is centered on single phase cooling of a single-row pin fins. A detailed list of major objectives of this research work is outlined below:

1. Set up experiments that integrate fluid loop, automated data acquisition system and flow visualization using high speed camera and microscope for the investigation of hydrodynamic cavitation in micro domains.

2. Determine flow condition criteria in which cavitation occurs behind various pin fin shapes in microchannel and characterize and compare cavity shape, length and type.

3. Develop a numerical framework to simulate both adiabatic and diabatic case studies, investigate flow around the pin fin and reveal vortical flow structure and wake region specification.

4. Design and fabricate microdevices capable of carrying out experiments to evaluate effects of single-row pin fin on heat transfer.

5. Carry out heat transfer measurements and perform numerical simulation on the heat transfer enhancement of the single-row pin fins.

3. MICROFABRICATION[1]

Two separate sets of micro devices used to perform cavitation studies and pin array heat transfer are explained in details in the following sections.

3.1.   Microfabrication of cavitation micro devices

The micro-devices were fabricated using *MEMS* techniques in a clean room environment. A silicon substrate and a Pyrex wafer were processed separately and then anodically bonded together.

The micro processing started with a *450* µm thick double-side polished silicon wafer. Silicon dioxide was thermally grown on both sides of the wafer by furnace oxidation. The oxide served as a hard mask for silicon deep reactive-ion etching *(DRIE)*, and the microchannel and pillar patterns were transferred to the silicon substrate. After being etched half way through *(~225 µm)*, the silicon wafer was flipped over; then the same etching procedure continued to etch through the holes for the fluid inlet and outlet. The silicon oxide was removed by buffered oxide etch (BOE). The patterned silicon wafer was then bonded to a Pyrex wafer to seal the microchannel from the top. Finally, each individual micro-device was separated from the bonded wafer using a die-saw machine. The microfabrication process was explained in details in [100].

---

[1] Portions of this chapter previously appeared as:

Nayebzadeh, A., Wang, Y., Tabkhi, H., Shin, J., and Peles, Y., 2018, "Cavitation behind a Circular Micro Pin Fin," *Int. J. Multiph. Flow*, 98, pp. 67–78. [Online] Available: https://www.sciencedirect.com/science/article/pii/S0301932216306620

Nayebzadeh, A., Tabkhi, H., Peles, Y., "Hydrodynamic cavitation downstream a micro pillar entrained inside a microchannel— a parametric study", *ASME Journal of Fluid Engineering*, vol. 141, 1, 2019. [Online] Available: http://fluidsengineering.asmedigitalcollection.asme.org/article.aspx?articleid=2682810

3.2.   Microfabrication of heat Transfer micro devices

The microfabrication was carried out in a cleanroom environment through multiple steps (Figure 8). A double-sided 500-µm Pyrex (Borofloat®) wafer was cleaned in Hamatech® tool with Piranha clean to remove all organic residues. A 0.5- µm layer of silicon nitride (Si_3N_4) was then deposited on one side of the wafer using an OXFORD® plasma-enhanced chemical vapor deposition (PECVD) technique. The layer served as a barrier and prevented the wafer from chemical reactions and oxidation during the subsequent microfabrication processes. A 7-nm Titanium layer was then deposited to promote adhesion of the 30-nm Platinum heater to the silicon nitride layer. This was performed in an AJA® sputtering tool with a custom-made recipe. To form the heater, HMDS adhesion promoter liquid (P20 prime) was poured onto the wafer followed by a S1818 photoresist, which was spun at a rate of 4000 rpm, 2500 acceleration for 30 seconds to form an even 2 µm thickness of the photoresist. After soft-baking on a hotplate for 100 seconds at a temperature of 115 °C, the wafer was placed in a contact aligner (Karl Suss MA6®) with the heater mask on top to pattern the heater. The photoresist was removed from the unmasked region on the wafer through a developing step in a Hamatech® tool. The Platinum and Titanium were etched to form the heater with AJA Ion Mill® tool. A custom made recipe with several cooling cycles was used to etch both metals without burning the photoresist. Once the metals were etched, the photoresist was removed by dipped the wafer into a solution of Microposit Remover 1165 (Microchem®) and subsequently placing it in a water tank with a sonic actuator at 50°C. The Aluminum heater vias were then deposited. A 20-nm Titanium layer followed by 1-µm Aluminum were deposited in the AJA® sputtering tool. Pattering the vias was performed similarly to the heater as explained above. It followed by wet Aluminum etching and by a Buffered Oxide Etch (BOE) 6:1 and 1165 photoresist remover. A similar process was followed for creating the RTDs and their vias on top of a 1-µm of silicon oxide (SiO2) layer that electrically insulated the heater. This SiO2 layer was formed by an OXFORD® PECVD deposition tool. Additional 1-µm SiO2 was deposited on top of RTDs' vias to protect the underlying layers. The final step was performed by removing SiO2 from the

heater and RTDs' vias using dry etching technique in an Oxford® 81 Etcher. To do so, two masks, one for the RTD vias and one for the heater vias were used to pattern the contact pads before the etching process.

To form the microchannel, SU-8 100 was spun, soft baked, exposed to UV light, post-exposure baked, developed, and was measured with a profilometer. One milliliter of SU-8 100 was placed over the previously fabricated Pyrex wafer and spun at 1500 rpm with 150 r/s ramp up and ramp down for a period of 45 seconds. For the Pyrex wafer, due to its low thermal conductivity, the soft bake and post-exposure bake were long to provide enough time for the heat to spread and also to prevent wafer bowing. The soft bake was performed at a temperature of 95 °C for 10 hours on a hotplate with 2 °C/min ramp up and down. In ABM® contact aligner with a near UV (350-400 nm) filter, the wafer was exposed for a total of 120 seconds. Afterward, post-exposure baking was done at 50 °C for 18 hours with 2 °C/min ramp up and down. Then, SU-8 was developed and stirred in pertinent solution. Afte rinsing and drying the wafer, the height of microchannels were measured in a profilometer (P-10®). Then, the individual micro-device was separated from the wafer in a DISCO® Dicing Saw. In a separate process, the sticker sheet and a bare Pyrex wafer were cut into the size of a micro-device using a Laser Cutter. The sticker had adhesion layers on both its sides with two liners enabling the attachement of one side while the other side was untouched. To protect the pin fins, the stickers were placed on the microchannel by peeling only one of the liners. After drilling the microchannel inlet and outlet, the bare Pyrex was attached to the sticker to form the micro-device.

1   Piranha clean of 500 μm Pyrex wafer

2   Deposit 0.5 μm Si_3N_4 on the Pyrex top

3   Sputter 7 nm Ti / 30 nm Pt

4   Dry Etch Pt and Ti

5   Deposit 10 nm Ti /1 μm Al

6   Wet Etch Al /Ti

7   Deposit 500 nm SiO_2

8   Dry etch SiO_2

9   Spin coat of 200 μm SU-8 on the Pyrex with heater and RTDs

10   Develop SU-8 to form microchannel and pin fins

11   Generate electrical contact pad holes on the double-sided sticker with Lase Cutter

12   Attach one side of sticker to cover the microchannel and pin fins

13   Drill microchannel inlet and outlet holes in machine shop

14   Drill electrical contact pad holes on another Pyrex with Laser Cutter

15

Legend

Pyrex	
Si_2N_4	
Titanium	
Platinum	
Aluminum	
SiO_2	
Heater, RTDs and Vias	
SU-8	
Sticker	

Figure 8: Microfluidic device fabrication process flow

4. THE MICRODEVICES AND PACKAGE[2]

4.1. Cavitation micro device and package

The package (Figure 9a), precision machined from Delrin®, contained the micro-device and provide fluidic connections to and from external fittings. A 4 mm thick aluminum cover plate, from the top, and a set of O-rings, from the bottom, were used to secure the device in the package and achieve hermetic fluidic seals. The micro-devices consisted of a silicon substrate with the microchannel and pillar anodically bonded to a Pyrex wafer. Micro fabrication techniques were utilized in a standard cleanroom environment. The microchannel dimensions were 18.5 mm long, 1.5 mm wide, and 225 µm high. Fluid entered the channel, travelled 13.5 mm before passing a pillar and then left the channel through the exit manifold. Figure 10 provides a schematic top view of the pillar geometries used in this study and their corresponding dimensions. The projected cross-sectional areas of all the pillars are identical to allow direct comparison among them. Since cavitation were formed downstream the pillars, pressure measurement at the vicinity of the cavity was performed by connecting the other end of the pillar's hole to a pressure transducer through the package.

---

[2] Portions of this chapter previously appeared as:

Nayebzadeh, A., Wang, Y., Tabkhi, H., Shin, J., and Peles, Y., 2018, "Cavitation behind a Circular Micro Pin Fin," *Int. J. Multiph. Flow*, 98, pp. 67–78. [Online] Available: https://www.sciencedirect.com/science/article/pii/S0301932216306620

Nayebzadeh, A., Tabkhi, H., Peles, Y., "Hydrodynamic cavitation downstream a micro pillar entrained inside a microchannel— a parametric study", *ASME Journal of Fluid Engineering*, vol. 141, 1, 2019. [Online] Available: http://fluidsengineering.asmedigitalcollection.asme.org/article.aspx?articleid=2682810
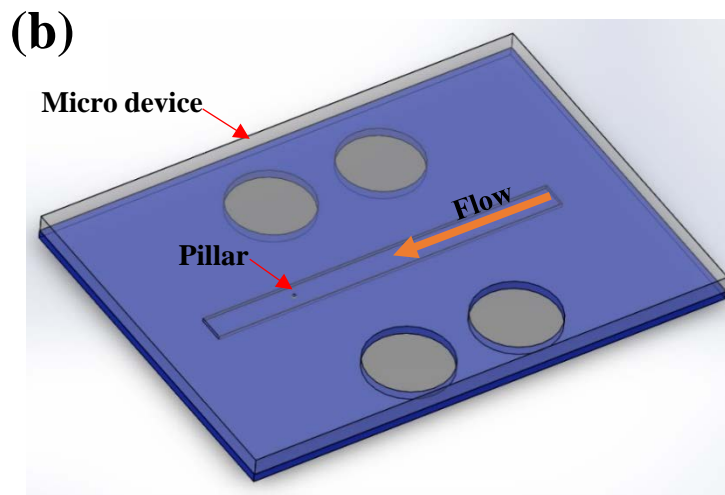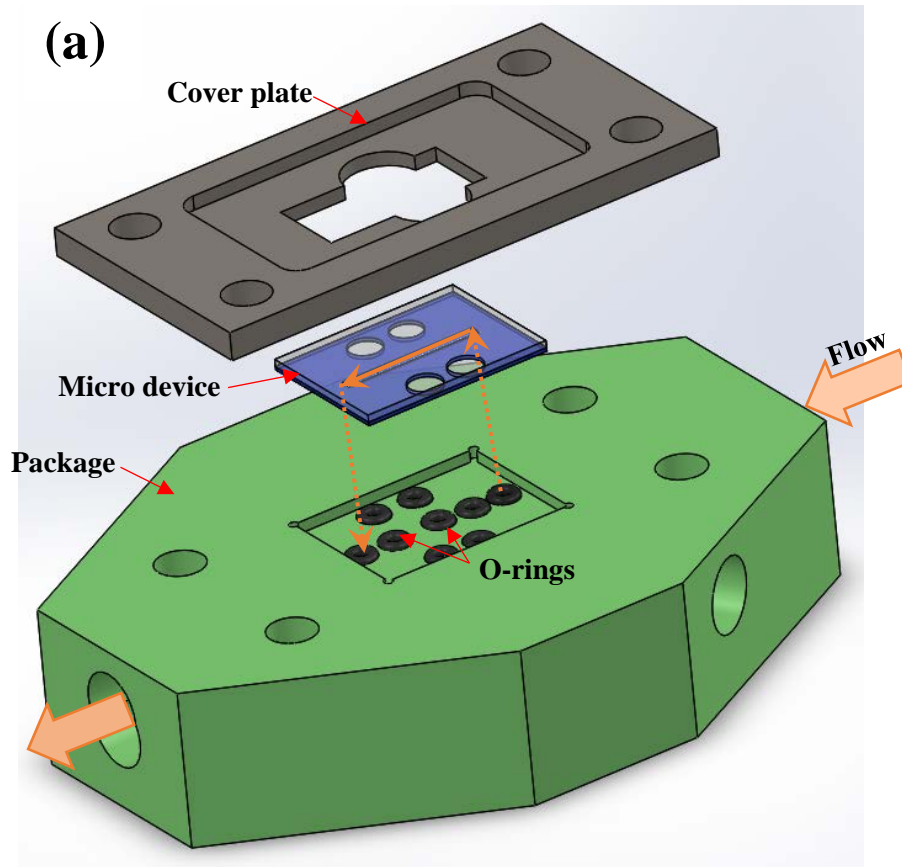
Figure 9: The package and the micro device. (a) A computer-aided design (CAD) schematic of the packaging assembly: the package, the micro device, a cover plate to keep the micro device in the package gap, and O-rings to prevent leakage. Flow entered the package and was guided toward the device through flow passages. (b) A schematic of the micro device with the pillar.

$D = 150\ \mu m$
$A = 0.0177\ mm^2$

$a = 202\ \mu m$
$A = 0.0177\ mm^2$

$a = 133\ \mu m$
$A = 0.0177\ mm^2$

$D = 150\ \mu m$
$A = 0.0353\ mm^2$
$G = 450\ \mu m$
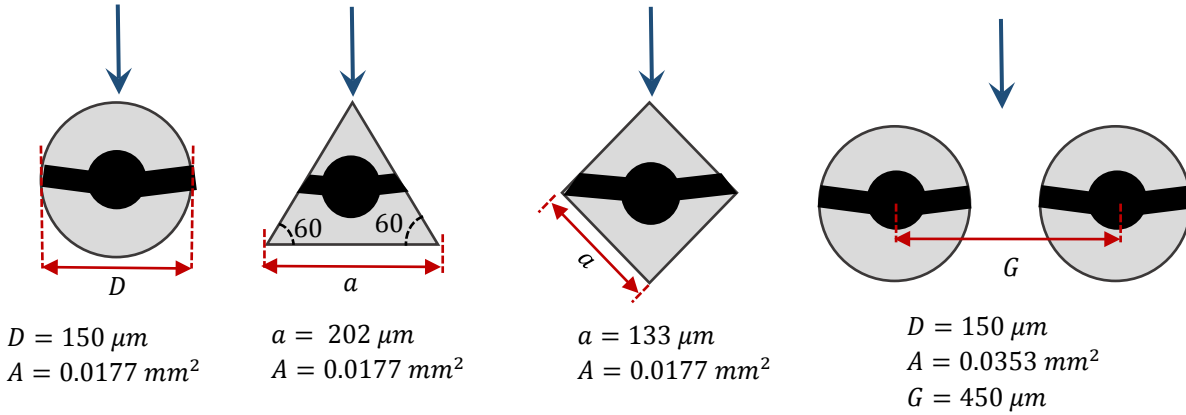
Figure 10: Schematic top-view of the pillars used in this study and their corresponding dimensions. The black regions correspond to the pillars' hollow regions where pressure measurement (P_p) was obtained.

4.2.   Pin fin Array heat transfer micro-devices

The micro-devices consisted of three substrates that formed the microchannel with the pin fins — a SU-8 substrate sandwiched between two Borofloat® Pyrex substrates. One Pyrex substrate carried a heater, RTDs, and electrical connections. The second Pyrex wafer was bonded to the microchannel through a special silicon sticker to form the top wall of the microchannel. The 130-µm thick sticker, Adhesive Research®, a transparent, inert to moisture and resistive against high temperatures adhesive, provided a hermetic seal between the microchannel and the top Pyrex substrate. The microchannel (23 mm long, 1.5 mm wide, and 200 µm high) was made of SU-8, a negative photoresist transparent material (Microchem®). The pin fin array, also made from SU-8, included five circular and hydrofoil pin fins and two half pin fins, and were located 13 mm from the fluid inlet just upstream of the heater (Figure 11). The 30-nm thick Platinum heater and eight RTDs were connected to contact pads through 1-µm thick Aluminum vias. The rectangular heater was 4.5 mm long and 1.5 mm wide; the serpentine RTDs occupied a total area of 65×65 µm² enabling local surface temperature measurement in the locations described in Figure 12 and Table 1.
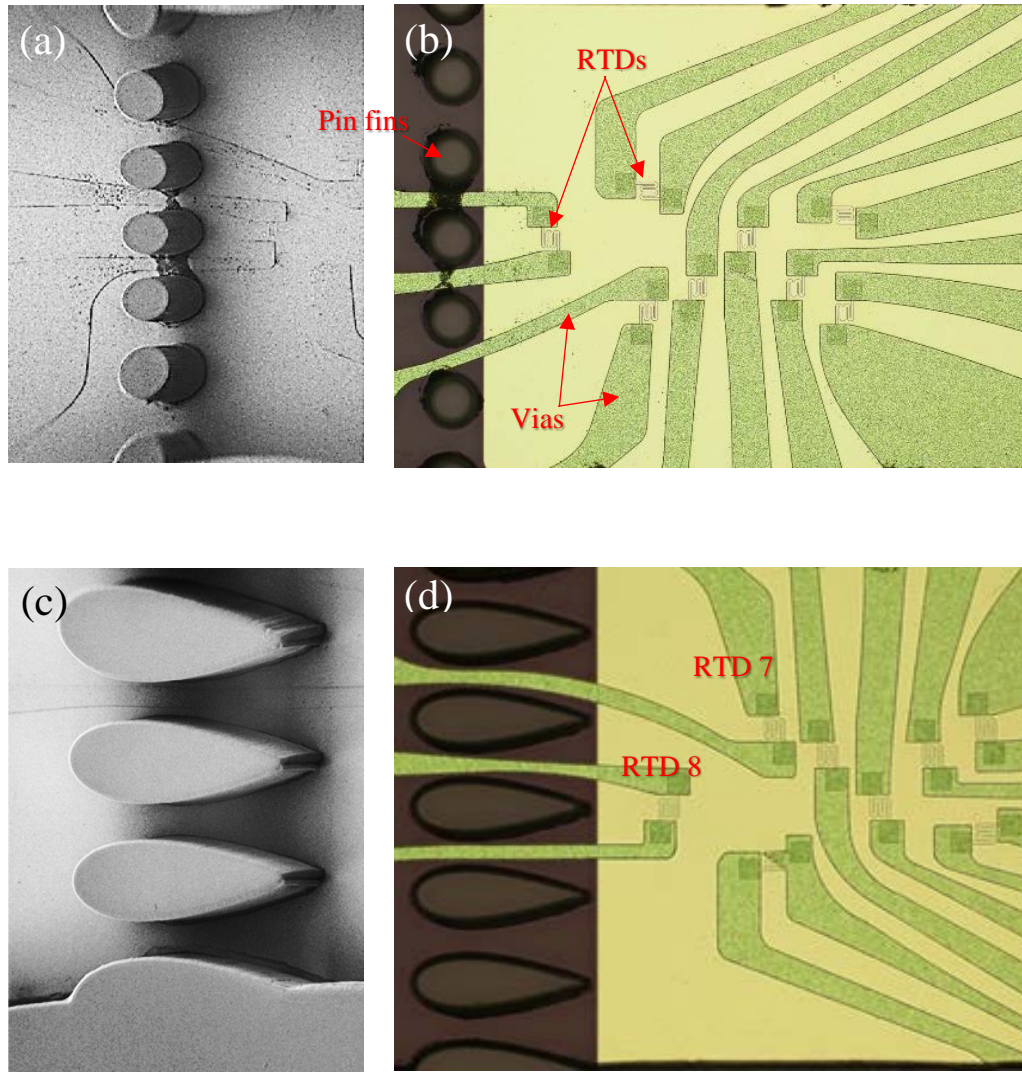
Figure 11: Images of pin fin array taken by (a) and (c) Scanning Election Microscope (SEM) and (b) and (d) by an optical microscope. Side pin fins appeared to be elliptical due to the wide window of imaging in SEM. Locations of eight RTDs and their respective electric vias are depicted in the right image.
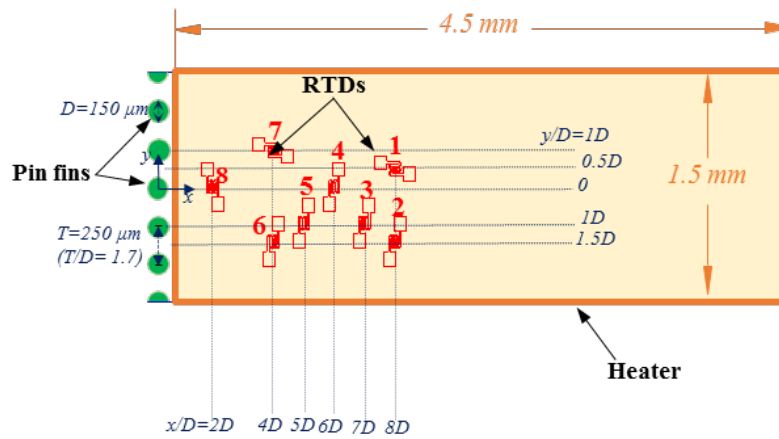
(a)
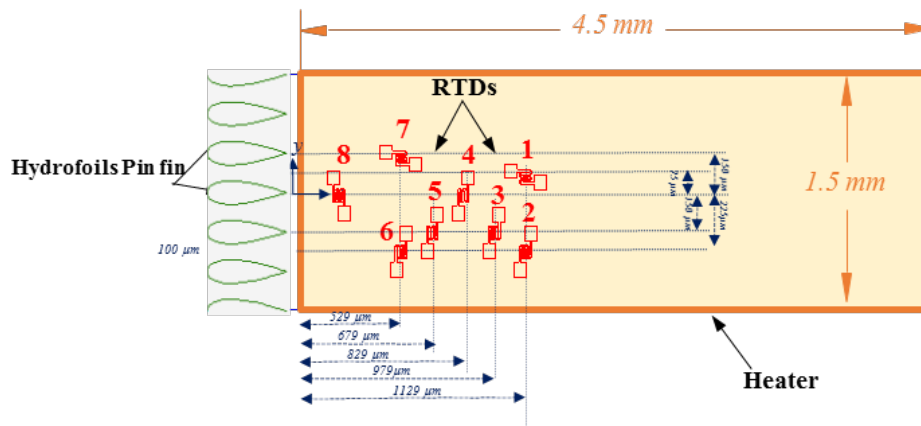
(b)

Figure 12: Pin fins, heater and RTDs arrangements for (a) circular and (b) hydrofoil arrays (not to scale). The serpentine dimension of the RTDs was $65 \times 65\ \mu m^2$.

Table 1: RTDs' dimensionless longitudinal distances for circular and hydrofoil configurations, for circular pin fins, the coordinate origin was located at the center of the middle pin fin. For hydrofoil pin fins, it was located on the trailing edge of the middle pin fin.

	Circular pin fins		Hydrofoil pin fins	
RTD Number	x/D	y/D	x/C	y/C
1	8	0.5	2.26	0.15
2	8	1.5	2.26	0.45
3	7	1	1.96	0.3
4	6	0	1.66	0
5	5	1	1.36	0.3
6	4	1.5	1	0.45
7	4	1	1	-
8	2	0	-	-

In order to connect the micro-device to the fluidic loop, a custom-made package made from Delrin® (DuPont) was designed and built (Figure 13). The fluidic paths inside the package connected the fluidic loop to the inlet and outlet of the microchannel. To hermetically seal the fluid inlet and outlet, two O-rings, made by Apple Rubber® were used in the inlet and outlet. The remaining O-rings served as a cushion to maintain the structural integrity of the device. The diameter and height of the O-rings were designed based on their lateral and vertical compression ratios to provide best sealing. One side of the package contains a rectangular groove for placing the micro-device. The groove depth calculated considering the total micro-

device thickness. A cover plate with the same material was bolted on top of the micro-device to secure it in

the grove.
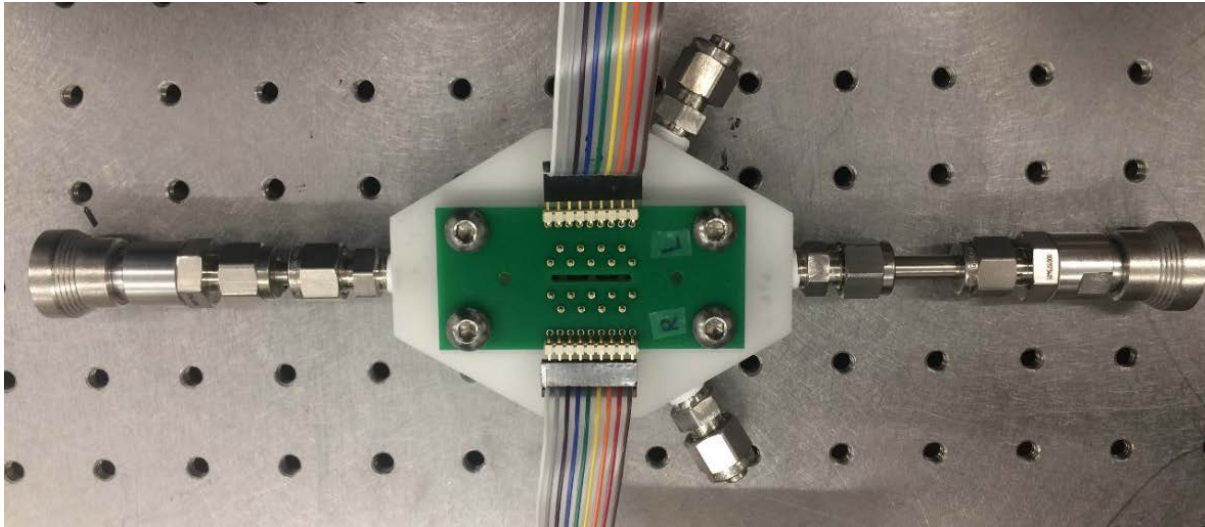
Figure 13: Top view of the hexagonal package made from Delrin, PCB board with two ribbon cables to electrically connect heater and RTDs to data acquisition systems

5. FLUIDIC LOOP AND EXPERIMENTAL PROCEDURE[3]

5.1. Experimental apparatus for cavitation experiments

Figure 14 shows the open fluidic loop that consisted of stainless steel inlet and outlet fluid pressure tanks manufactured by Alloy Products Corp®. A helium gas cylinder and a vacuum pump (Marathon®) were connected to the inlet and outlet tanks to provide the required pressure difference throughout the experiments. The flow loop also included a rotameter to measure volumetric flow rate, pressure transducers capable of measuring positive and vacuum pressures, and T-type thermocouples were all from OMEGA®. The micro device was embedded in the package and the entire system was placed above a Zeiss® Axio Observer inverted microscope that was connected to a high-speed camera (Phantom Miro® 320 from Vision Research) to enable flow visualization. The data acquisition system included a cDAQ from NI® connected to a LabVIEW® software for monitoring and collecting data. All piping and fittings were provided from Swagelok®.

Distilled water was used as the working fluid. To minimize the influence of dissolved gas content on the inception of cavitation, the water in the inlet tank was vacuumed for at least 24 hours before each

---

[3] Portions of this chapter previously appeared as:

Nayebzadeh, A., Wang, Y., Tabkhi, H., Shin, J., and Peles, Y., 2018, "Cavitation behind a Circular Micro Pin Fin," *Int. J. Multiph. Flow*, 98, pp. 67–78. [Online] Available: https://www.sciencedirect.com/science/article/pii/S0301932216306620

Nayebzadeh, A., Tabkhi, H., Peles, Y., "Hydrodynamic cavitation downstream a micro pillar entrained inside a microchannel— a parametric study", *ASME Journal of Fluid Engineering*, vol. 141, 1, 2019. [Online] Available: http://fluidsengineering.asmedigitalcollection.asme.org/article.aspx?articleid=2682810

experiment. A typical run was performed by turning on the vacuum pump at the outlet tank. Once the vacuum pressure was stabilized, the ball valve between the inlet tank and the package was manually opened.

High speed imagery was collected at 20 kHz sampling frequency and the resulting movies were converted to a series of images for further analysis.
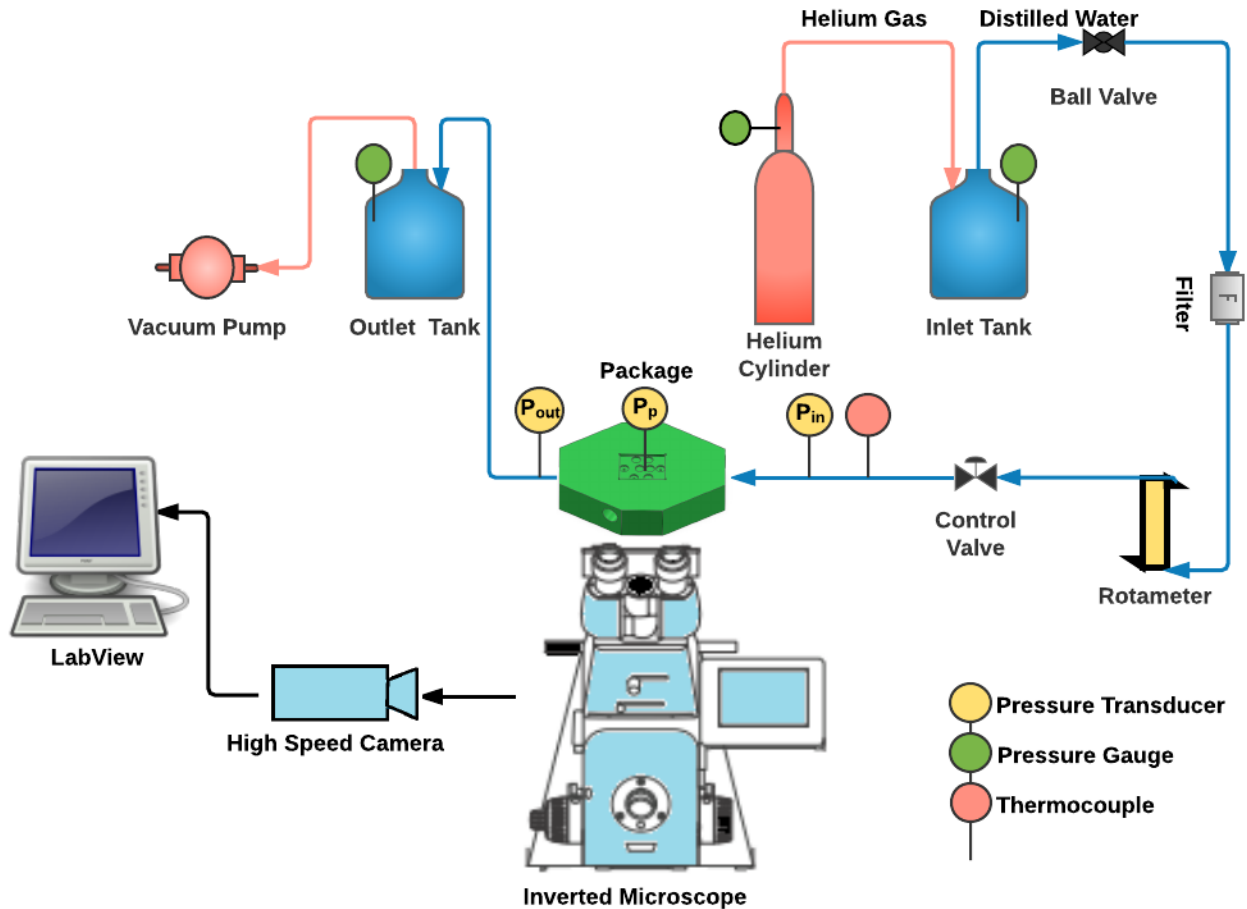
Figure 14: Schematic of experimental fluid loop: reduced pressure created by vacuuming the outlet pressure drive the flow in the loop, P_{mc} and P_{pf} are pin fin upstream and center-point pin fin pressures, respectively.

5.2. Experimental apparatus for heat transfer measurements

5.2.1. Electrical connections and apparatus

A custom-designed printed circuit board (PCB), manufactured by Sunstone Circuits®, were brazed to spring-loaded probe pins to provide electrical connection between the heater and RTDs contact pads to two ribbon cables. The cables connected the PCB to a SCXI data acquisition (DAQ) unit from National Instrument (NI®), a power supply, and two digital multimeters from Keysight® (Figure 15). Electric current to the heater was provided by a Keysight® power supply. To calculate the electric power supplied to the heater, the electric current and voltage across the heater were measured. Two digital multimeters for electric current and voltage measurements were connected in series and in parallel, respectively. Each RTD was wired to a SCXI 1581 National Instrument® current excitation module to provide a constant current of 100 µA. In addition, the RTDs were connected to an analog input module (SCXI-1102C, NI) to measure each RTD's voltage. Electrical resistances of the RTDs were then calculated by dividing voltage over the constant current in a LabVIEW custom made program.

5.2.2. Fluidic loop setup

Distilled water was used as a working fluid in an open fluidic loop incorporating two stainless steel pressure vessels. High pressure nitrogen gas tank generated a pressure difference to drive the flow. After opening the gate valve, placed right downstream the inlet tank, the flow passed through a filter, a rotameter (Omega®), the package, the micro-device, before finally exiting into the outlet vessel. All the fittings and tubing were from Swegelock®. Temperatures and pressures upstream and downstream the package were measured by T-type thermocouples and pressure transducers (all from Omega®) connected to a compact data acquisition system (cDAQ), NI® and the LabVIEW program. An inverted microscope (Zeiss, Axio

Observer®) and a high-speed camera (Phantom Miro 310 from Vision research®) captured high-speed movies of the flow.
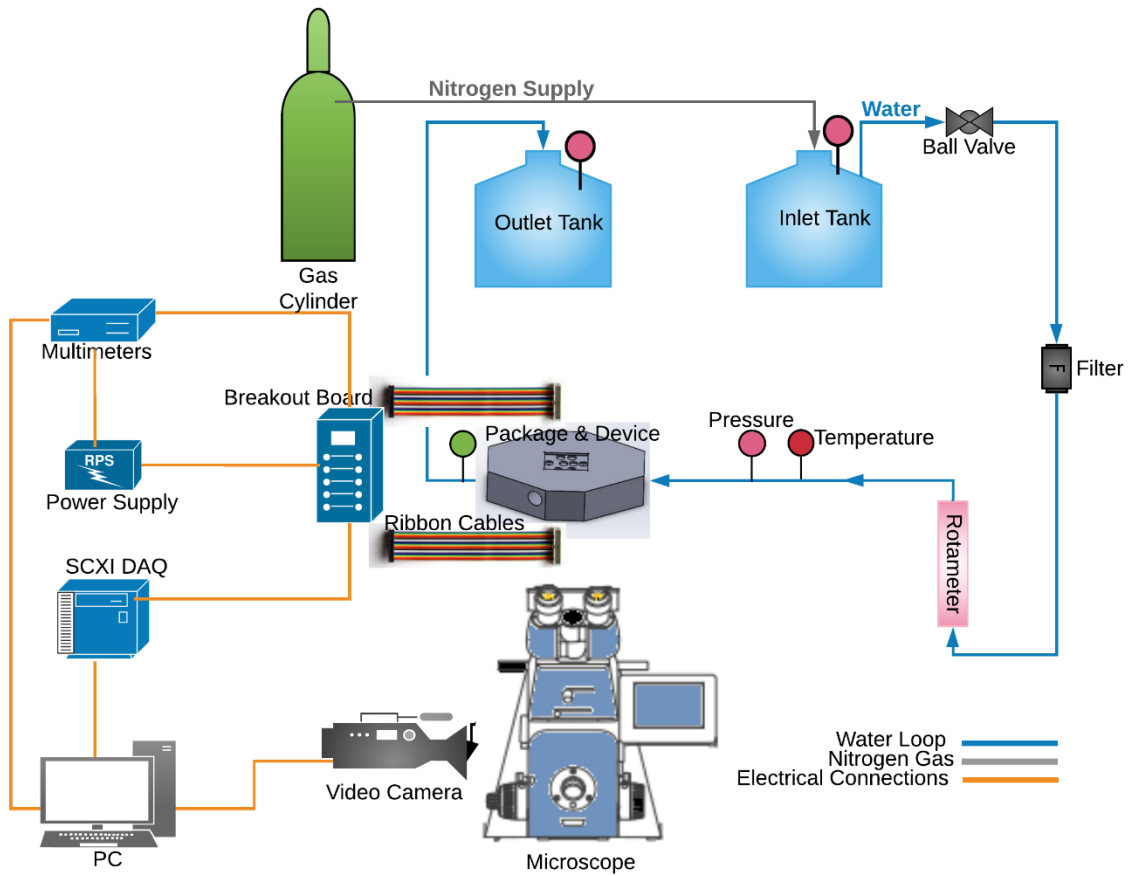
Figure 15: Schematic of the experimental fluidic open loop, which consisted of an inlet and an outlet tanks. Pressurized gas cylinder used to control the inlet tank pressure. The package was electrically connected to a breakout board via two ribbon cables. Water line, nitrogen gas, and electrical connections are shown in blue, gray and orange, respectively.

6. UNCERTAINTIES

Uncertainties of measured variables/parameters were obtained from the manufacturer datasheets and standard error propagation procedure [101] was followed for the calculated parameters. Table 2 summarizes the measurement uncertainties for cavitation experiments.

Table 2: Experimental uncertainties for the measured parameters

Property	Uncertainty
Pressure (kPa)	1
Flowrate (ml/min)	3
Pressure difference (kPa)	1.5
Cavitation inception number (σ_i)	7%
Reynolds number (Re)	4%

For heat transfer measurements, the uncertainty of the RTD measurements was ± 0.8 ℃. The uncertainty of the local heat transfer coefficient was less than 8%. The uncertainty associated with Reynolds number was less than 9%.

7. NUMERICAL SIMULATION

7.1. Numerical modeling for cavitation study

The obtained pressures from measurements were limited to four locations, which were P_{in}, P_{mc}, P_p and P_{out} (Figure 14). The flow pattern that existed downstream of the pillar was characterized by a wake region and unsteady vortex shedding. To obtain insight about the manner in which the pressure varied and to obtain information about the flow structure throughout the entire microchannel, liquid single-phase numerical simulations were performed. As stated earlier in the experimental section, single phase flow was dominated throughout the experiments until witnessing the appearance of shedding bubbles, the attached cavity, and elongated cavity. Since the purpose of the numerical simulation was to obtain pressure distribution, and to avoid the intricacy of two-phase flow simulation, single phase simulation was performed.

Figure 16 depicts a three dimensional fluid domain consisting of the entire microchannel. As previously noted in the experimental section, pressure transducers were not located at the inlet and outlet of the microchannel. However, for robust simulations, proper inlet and outlet boundary conditions are required. For the inlet of the microchannel, known mass flow rate of each experiment was used for each run. Outlet pressure value was of critical importance as it can affect the pressure distribution significantly. Given P_{in} and P_{out} and by estimating pressure drop from P_{in} to P_1 and P_{out} to P_2, it is possible to estimate P_1 and P_2. This calculation is discussed in subsequent section. No-slip boundary conditions were imposed on all walls including the pillar surface. The density and dynamic viscosity of distilled water were taken as $\rho = 998.7$ kg/m^3 and $\mu = 9.61 \times 10^{-4}$ $Pa \cdot s$, respectively, which corresponds to distilled water at 22.2 °C.

At high enough Reynolds numbers, the presence of the pillar produced vortex shedding and unsteady wake region downstream, hence unsteady Navier-Stokes equations were solved numerically using STAR-

CCM+®,10.04.011-R8. Calculated Reynolds numbers based on the microchannel hydraulic diameter shows that all cases were in the range of $1620 \leq Re \leq 2060$, therefore, laminar model used in this simulation.

Continuity and momentum equations were solved simultaneously utilizing implicit coupled flow model by a pseudo-time-marching approach. A second-order upwind discretization scheme were applied for convection and diffusion fluxes while enabling boundary secondary gradients. Second- order temporal scheme discretization of the unsteady term was employed. Simulations were initiated with low courant numbers and continued increasing it to achieve higher convergence rate.
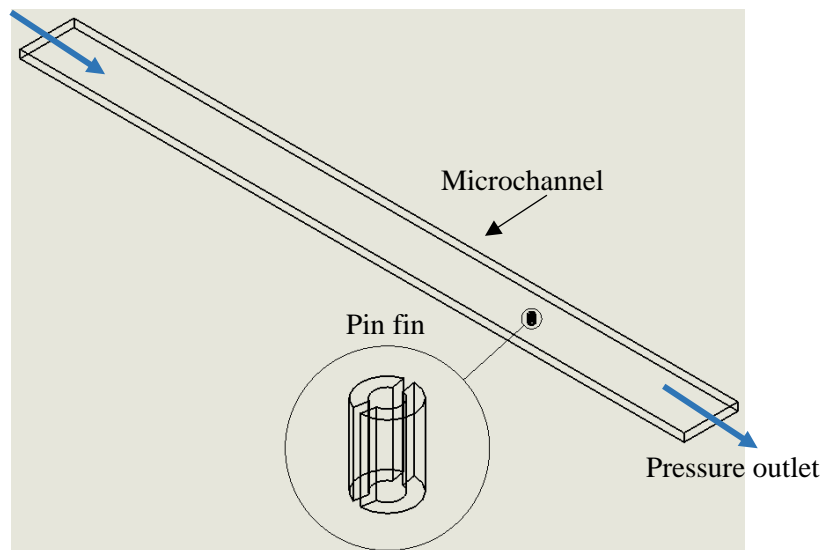
Figure 16: 3D numerical simulation computational domain and boundary conditions of the microchannel

A hybrid grid consisting of prism layers on the pillar surface and polyhedral grid over the entire microchannel was produced to discretize the computational domain (Figure 17). Grid refinements were performed in the proximity of the pillar area and in the wake region in order to resolve the separation locations on the pillar mid-plane perimeter and also to better simulate vortical flow downstream of the pillar. Grid convergence and time step size study were done to validate the accuracy of the results.

Time step for each simulation was determined by two methods. In the first method, an initial guess was made for shedding Strouhal number $(St = \frac{f.D_h}{\bar{V}})$ based on available literature and the corresponding frequency and period were calculated. Then, period was divided by 30 in order to capture adequate shedding cycles. The second method was based on keeping the Courant–Friedrichs–Lewy number $\left(CFL = \frac{\bar{V}.\Delta t}{\Delta x}\right)$ equal to unity. Time step was calculated by the following equation:

$$\Delta t = \frac{1 \times \Delta x_{min}}{V_{max}} \tag{7}$$

where Δx_{min} is the minimum grid dimension and V_{max} is the maximum velocity in the field.

Because *CFL=1* led to smaller time steps and higher computational costs, the results obtained by the two methods were compared together. Simulations were performed with these two time steps and a maximum average time step dependency of *9%* was witnessed.
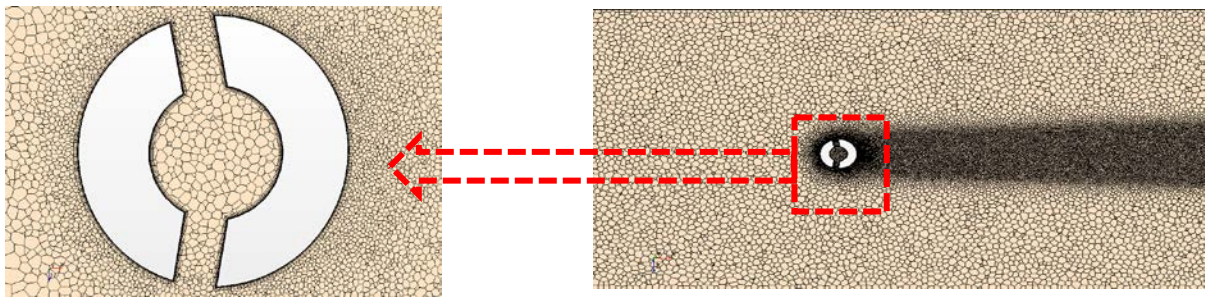
Figure 17: Top view of computational grid in the pillar area: grid refinements around and downstream of the pillar

7.1.1. **Pressure drop calculation**

Available correlations were applied to calculate pressure drop ($P_2 - P_{out}$). Figure 18 shows liquid path from P_{in} toward the inlet of the microchannel. The fluid flows through circular piping and the path consists of an expansion, a contraction, a $90°$ bend followed by a contraction and elevation, then another $90°$ and a change of cross-section from circular to rectangular at the microchannel. The same path from P_2 to P_{out} existed in the reverse direction.
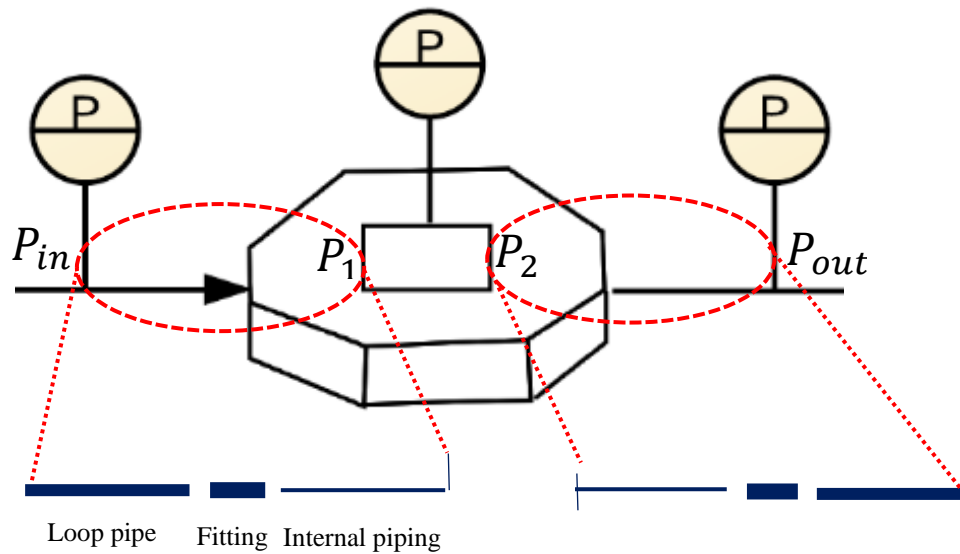
Figure 18: Schematic diagram of flow path throughout package

Total head loss was regarded as the sum of losses due to frictional effects in fully developed flow and losses due to abrupt changes in the area and direction of the flow, entrances, fittings and so on.

Total losses resulting from frictional loss are calculated using Equation (8):

$$h_1 = \sum_{i=1}^{4} f_i \frac{L_i}{D_i} \frac{\bar{V}_i^2}{2} \qquad (8)$$

Where h_1 is the frictional head loss, f_i is the friction factor, L_i is the length of the channel with constant area, D_i is diameter of channel, and $\bar{V}_i$ is the average velocity in the channel. As shown in Fig. 12, the diameter of the channel had four segments corresponding to four different diameters. In laminar flow and for circular pipes, f_i is estimated based on each section's Reynolds number via the following relation:

$$f_i = \frac{64}{Re_i} \tag{9}$$

Losses caused by the change in pipe area, i.e., contraction, expansion, or bends can be estimated by equation (10), noting that there are six types of these losses from the location of the inlet pressure transducer toward the inlet of the microchannel.

$$h_2 = \sum_{i=1}^{6} K_i \frac{\bar{V}_i^2}{2} \tag{10}$$

In the above equation, h_2 is an abrupt change loss, K_i is the loss coefficient. Corresponding correlations were used depending on whether there was a contraction, an expansion, or a bend.

Using Bernoulli's equation and neglecting the elevation change, Equation (11) was used to estimate P_1:

$$P_1 = P_{in} + \frac{\rho}{2}\left(\bar{V}_{in}^2 - \bar{V}_1^2 - h_1 - h_2\right) \tag{11}$$

Where $\bar{V}_{in}$ and $\bar{V}_1$ are the average velocities at the inlet pressure transducer and the inlet of the microchannel, respectively. Assuming the same pressure drop for the outlet region, P_2 can be estimated in the same manner and was used as the outlet pressure for the simulation.

7.2. Numerical simulation for heat transfer measurements

A 3D numerical model of the conjugate conduction/convection heat transfer process in the micro device (Figure 19) was developed using commercially available Star-CCM+ software. The model complemented the experimental results and provide further insight on the flow and heat transfer processes.

7.2.1. Numerical grid

A hybrid grid consisted of unstructured and structured elements were generated to capture near surface fluid flow and heat transfer (Figure 20). In particular, the appropriate number of structured elements called prism layers on the pin fins and the heater surfaces were chosen to accurately capture the wake region, flow accelerations and decelerations, vortex shedding, and the conjugate heat transfer process. For an improved gird resolution, three levels of grid refinements based on the surfaces of the pin fins, the surface of the heater, and a specific volume block were also created.
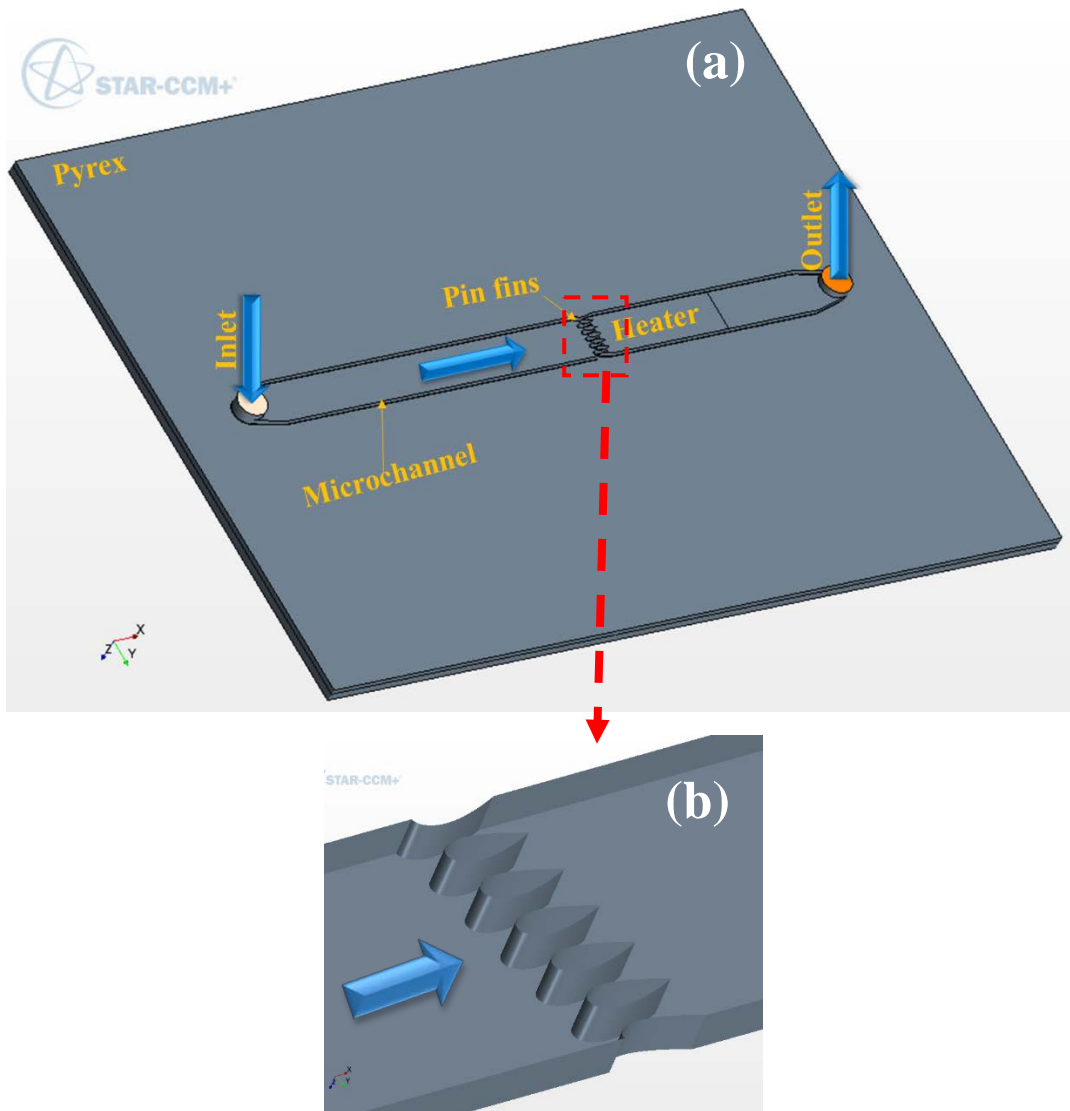
Figure 19: The micro device used for the thermal-fluid numerical model; (a) the entire 3D computational domain, (b) zoom-in view of pin fin row.
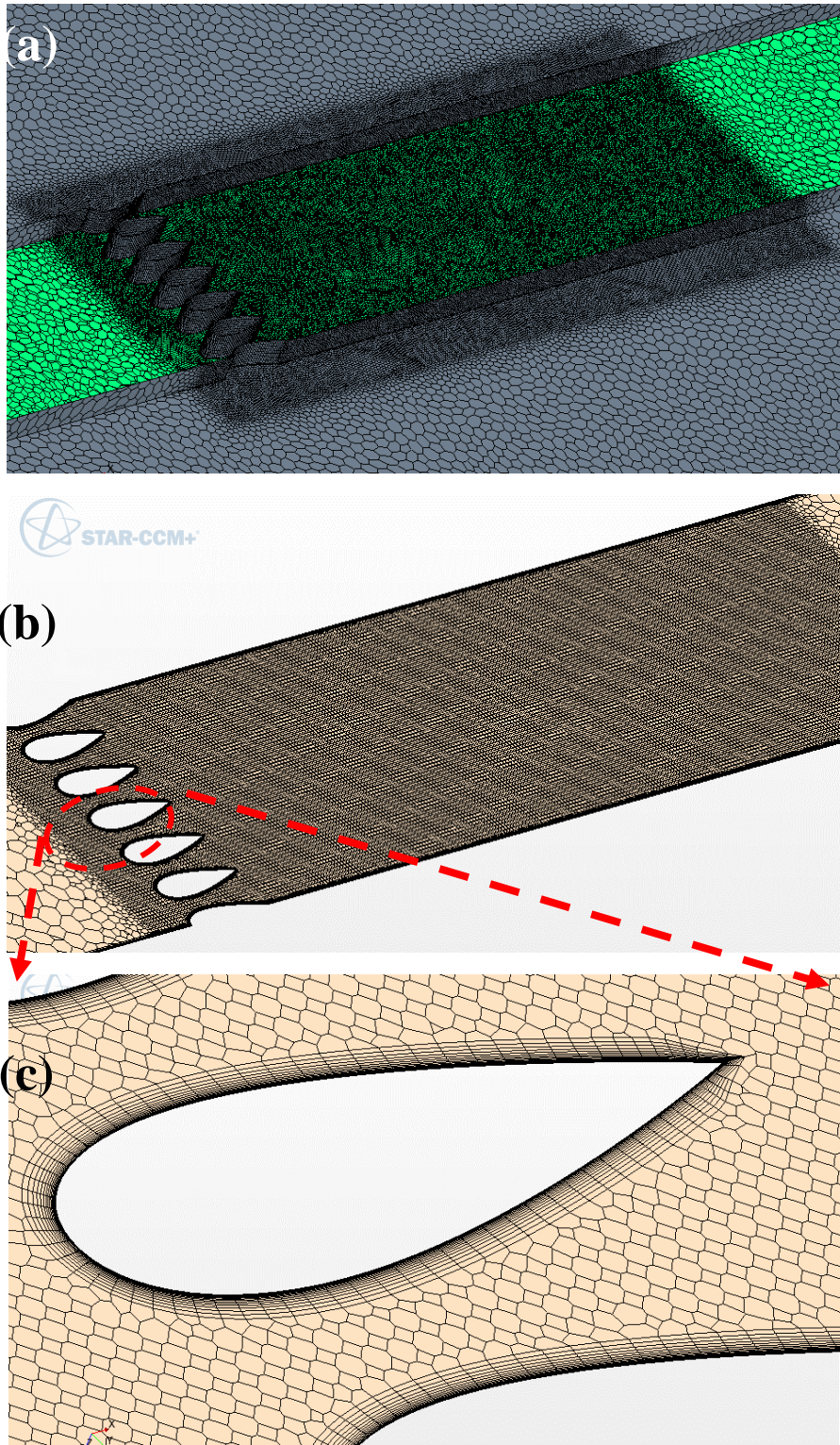
Figure 20: Computational grid; (a) grid refinements in the vicinity of pin fin and heater, (b) grid on the microchannel mid-plane, (c) zoom-in view of the grid and prism layers over the mid-hydrofoil.

7.2.2. **Boundary Conditions**

The computational domain includes the microchannel and pin fins made from SU-8 and the Pyrex substrate with the embedded heater. The cover Pyrex substrate and the sticker were not modeled since they added a considerable amount of computational cost. To quantify this effect, a separate computational domain with the entire micro device was modeled and showed an average of 15% increase on heater temperature when compared to the experimental measurements. The microchannel inlet and outlet were set as mass flow inlet and pressure outlet based on the experimental measurement from the rotameter and pressure transducer, respectively, in the fluidic loop. The conjugate heat conduction and convection was simulated by creating conformal interfaces between the Pyrex substrate and the fluid volume inside the microchannel. Heater as the heat source was simulated using a feature called "shell," which allows meshless modeling of ultra-thin objects. The upper and lower wall of the heater were in direct contacts with the fluid and Pyrex with a heat generation source inside the 30 nm thick heater. Other walls of the microchannel were assumed adiabatic because conduction through SU-8 and the sticker can be ignored as explained earlier. A heat transfer coefficient of $h = 10 \ W/m^2 \cdot k$ was set for the outer surfaces of the Pyrex to model natural convection heat transfer to the ambient.

8. RESULTS

In this chapter, measurements and numerical simulations for the hydrodynamic cavitation and also heat transfer studies are discussed.

8.1. Cavitation study results

In this section, flow visualization is presented to investigate the appearance of the cavitation inception and elongated cavity. To further study, signal processing with Fast Fourier Transform *(FFT)* on the cavitation images were implemented to find cavity dominant lateral pulsating frequency and then relate it to the vortex shedding frequency. The unsteady numerical simulation helped to find vortex shedding frequency.

8.1.1. Cavitation characteristics over circular pin fin

Figure 21 shows top-view images corresponding to the different instances of the inception and the development of cavitation behind the pin fin for $Re = 1620$, $\sigma_i = 2.20$. Four phases can be detected: (1) travelling vapor bubble shedding from the pin fin, (2) formation of unstable rotational vapor region adjacent to the pin fin and shedding bubble further downstream, (3) formation of attached cavity, and (4) stable elongated attached cavity with pulsating behavior at the trailing edge of cavity.

The gradual process of stretching of the attached cavity was accompanied by longitudinal and lateral pulsations with higher amplitudes in the longitudinal direction until reaching a point in which the average length of the cavity did not change.

Except the duration required for these steps to complete, which tended to be longer for higher Reynolds numbers, the general trend was almost identical among all test cases. In particular, by lowering the Reynolds number to *Re =1620*, the shedding bubble phase was shortened and the attached cavity formed very fast.

On the other hand, increasing Reynolds number delayed the process of transition from cyclic to fixed cavity. At $Re = 2060$, for example, bubble shedding appeared and disappeared sporadically for about 40 minutes before the formation of the attached cavity.

One deviation from macroscale is that transitional cavity (converting from cyclic to fixed cavity) was not seen here at this scale. Cavitation at each test commenced with cyclic type followed by an attached elongated cavity.
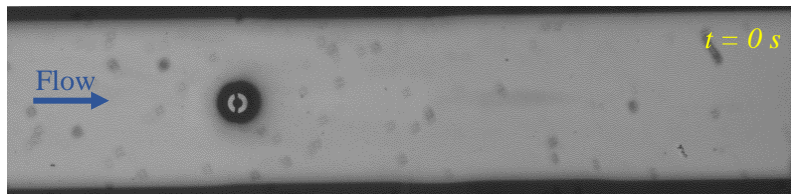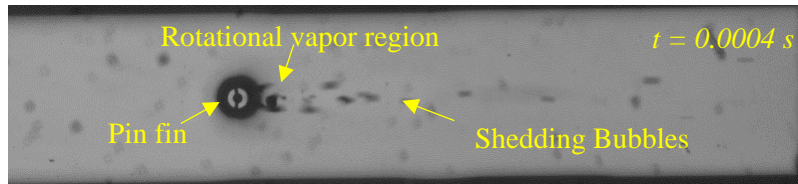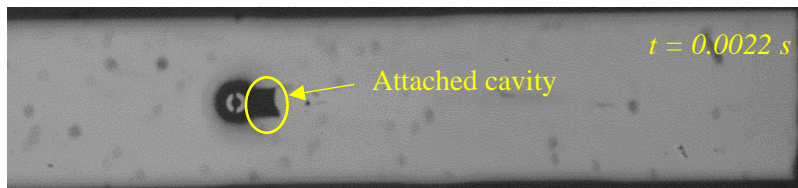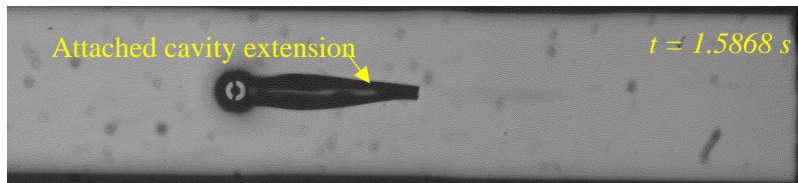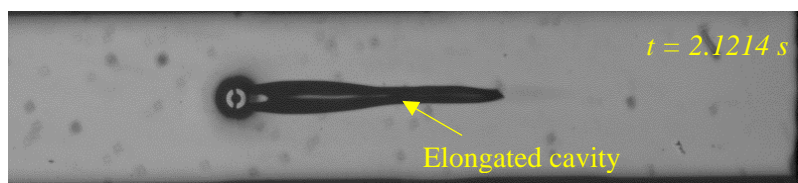
Figure 21: Snapshot of microchannel top view in the pin fin area showing cavitation development at $Re = 1620$, $\sigma_i = 2.20$. (a) no cavitation $(t = 0\ s)$, (b) unstable rotational vapor region and shedding bubbles $(t = 0.0004\ s)$, (c) appearance of attached cavity $(t = 0.0022\ s)$, (d) extension of attached cavity $(t = 1.5868\ s)$, and (e) elongated cavity $(t = 2.1214\ s)$

43

The characteristics of the elongated cavity was very repeatable, and were quantified using a series of visualization images. Figure 22 demonstrates the cavity average length and width and also the angles at which the cavity was attached to the pin fin for $Re = 1620, \sigma_i = 2.20$. The maximum width of the cavity ($W_{c,Max.}$) was observed to be about mid point downstream of the cavity length and was about *1.6D* wide. Longitudinal pulsation of the cavity resulted in an average maximum cavity length of about $L_{c,Max.} = 2.5$ mm *(16D)* for all Reynolds numbers which is longer than the maximum cavity length of *10D* at macroscale reported by [60]. The angle at which the cavity was attached to the pin fin was estimated to be about $\theta = 135^{\circ}$.
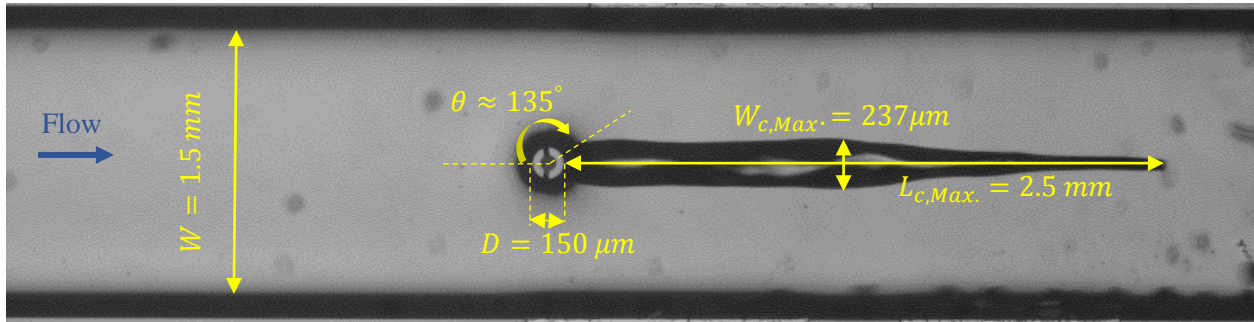
Figure 22: Stable attached cavity dimensions for *Re=1620, σ_i=2.20*

8.1.1.1. Spectral analysis of cavity images and pressure time series

To quantify cavitation shedding frequency, the images captured by the camera with a sampling frequency of *40* kHz were converted to a series of frames and analyzed using MATLAB® software. Similar to the method employed by [45], the level of gray intensity for each pixel was calculated after eliminating high frequency noise through performing spatial averaging. Figure 23 (b-d) show time series of the average light intensity *A(t)* or image brightness in three regions for $\sigma_i = 2.20$. The oscillatory behavior of the vapor cavity is particularly noticeable in these plots.
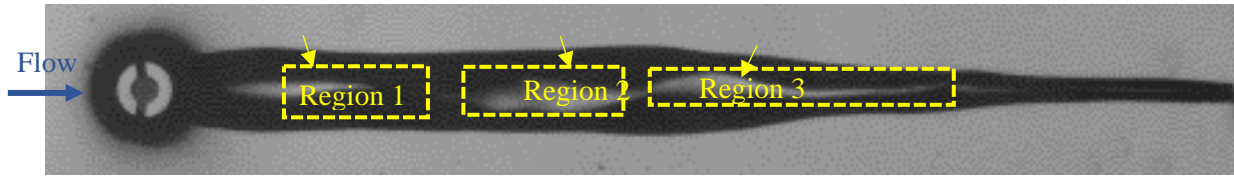
(a)
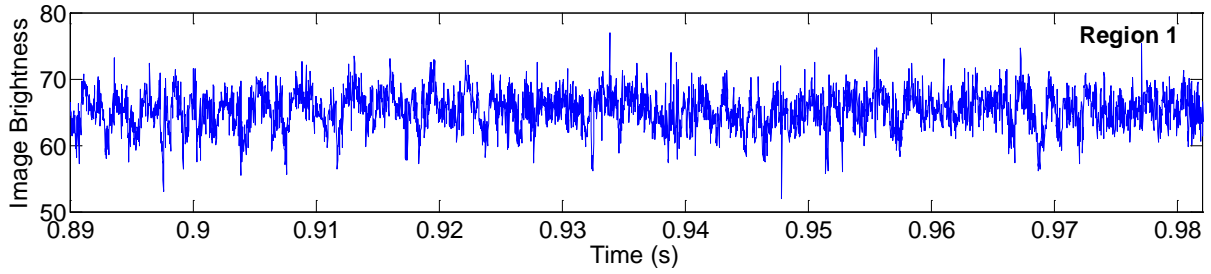
(b)
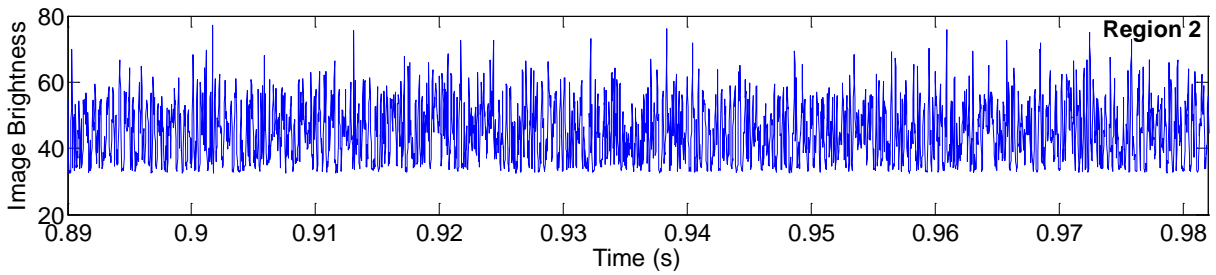
(c)
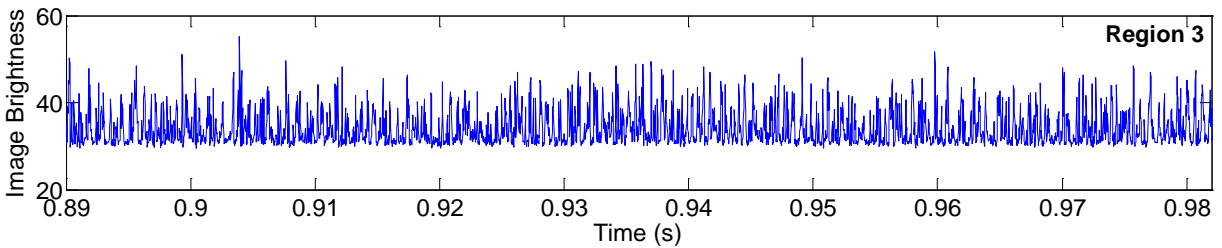
(d)

Figure 23: Image light intensities for cavitation region, $\sigma_i = 2.20$: (a) Selected cavitation regions for image processing (b-d) time history of average image brightness in different regions.

In Figure 24, the *FFT* amplitude spectrums of the average light intensity are plotted over the specified regions. A peak frequency range of *1600* to *3000* Hz has been observed for region 1. The maximum *FFT* amplitude occurred at region 2 with a narrower dominant frequency range of *2500-3000* Hz. For region 3,

45

the slope seems to be flatter with the lowest signal amplitudes and the peak frequency ranging from *2500* to *3600* Hz.

(a)

(b)

(c)
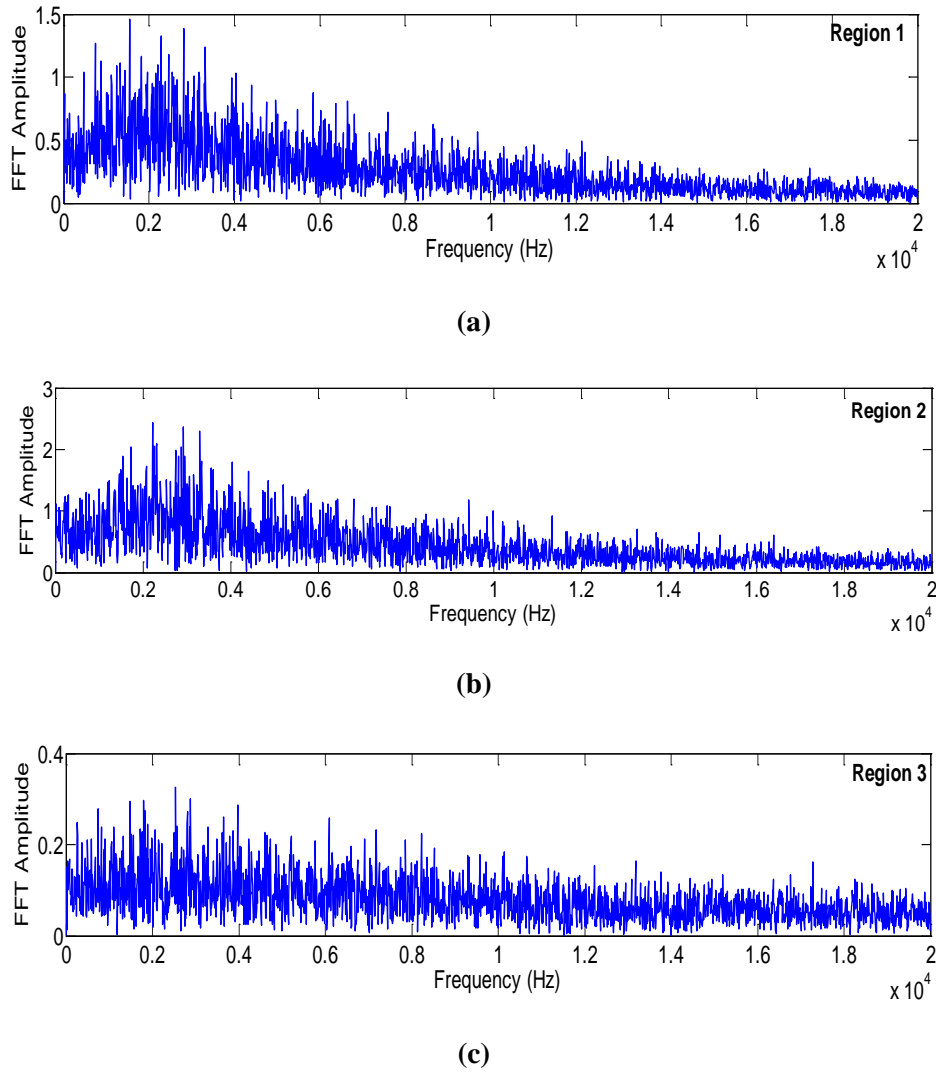
Figure 24: *FFT* results for regions 1, 2 and 3 shown in (a), (b) and (c), $\sigma_i = 2.20$.

The images captured by the camera were synchronized with pressure measurements using a pulse generator, which triggered both the camera and data acquisition system at the instance with the sampling frequency of *40* kHz. Figure 25 illustrates the synchronized pin fin pressure (P_{pf}) signal and *FFT* spectrum with the data presented in Figure 23 and Figure 24. The *FFT* amplitudes show agreement with the amplitude spectra of the time history of the average image brightness for various cavitation flow patterns. This indicates that the pressure signal contained all the characteristic frequencies associated with cavitating flow patterns.
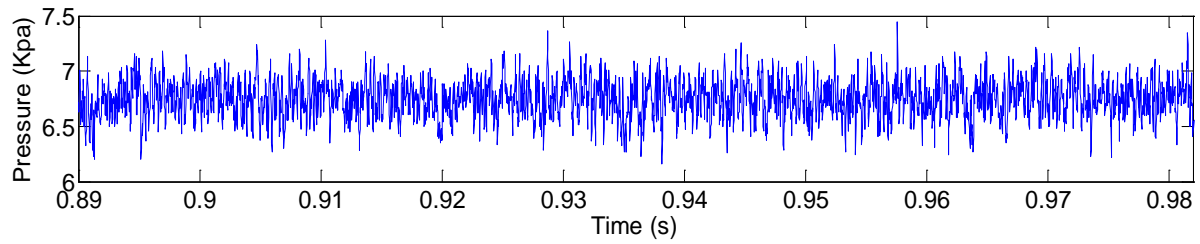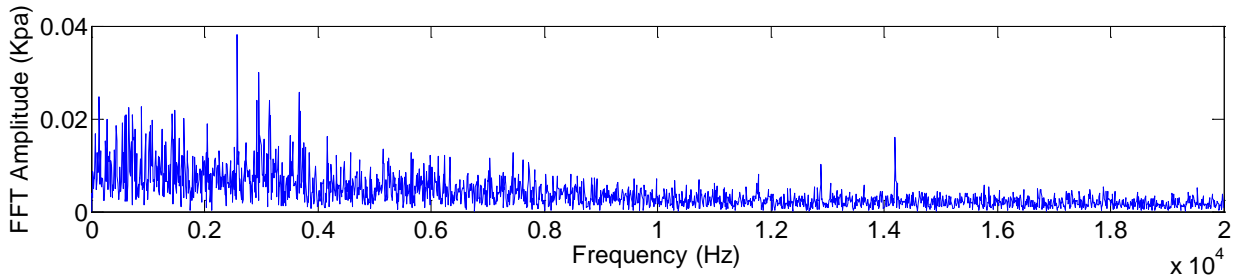
Figure 25: (a) Pin fin pressure (P_{pf}) history (b) *FFT* results of pin fin pressure (P_{pf})

8.1.1.2. Pressure and velocity effects on cavitation inception

As seen from Figure 26, there is a slight dependency between cavitation number and pressure difference indicating negligible pressure scale effects similar to the macro scale, albeit in different geometries (micro-orifice)[3].
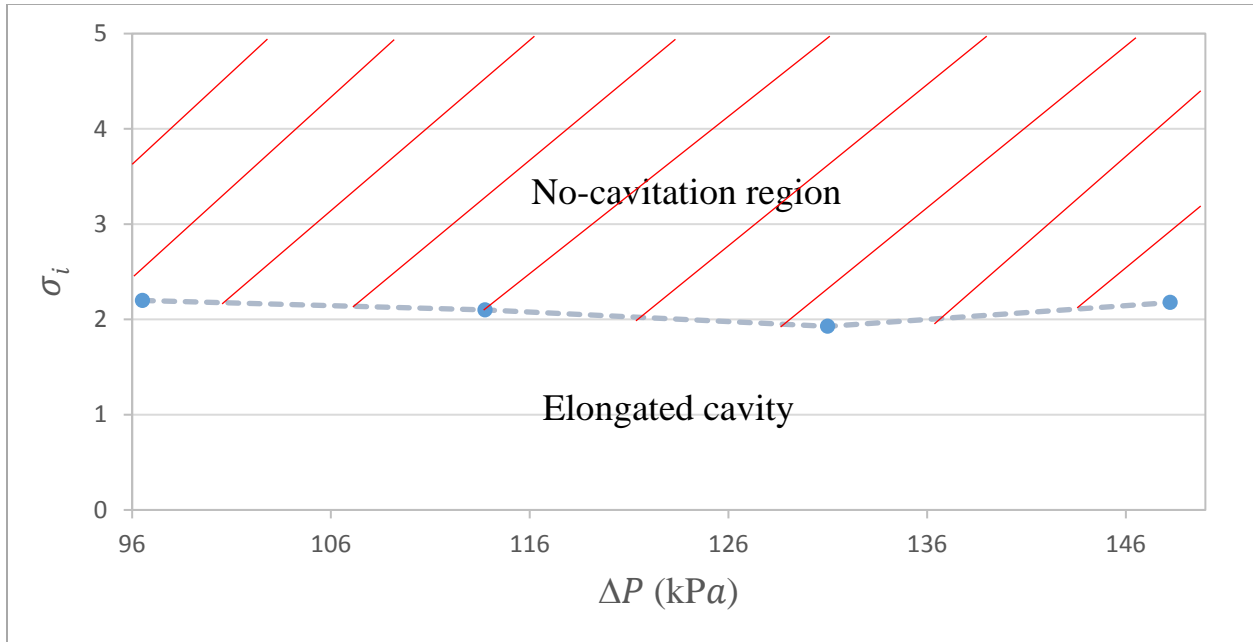
Figure 26: Cavitation map displaying pressure difference range versus incipient cavitation number at which elongated cavity occurred.

Figure 27 shows the mean velocity in the pin fin area as a function of the cavitation inception number. Similar to cavitation in macro scale domain, incipient cavitation number did not depend on velocity.
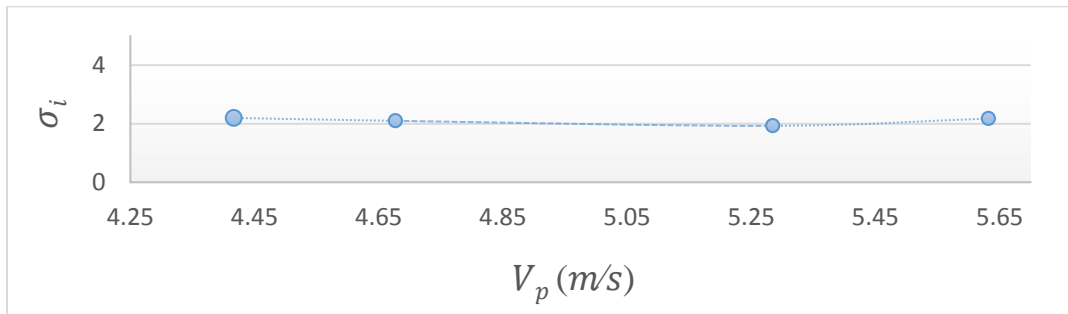
Figure 27: Effect of velocity on cavitation inception number

8.1.1.3. Numerical results

Figure 28 depicts mean pressure coefficient in the mid-plane of the pin fin and compares the locations of minimum $C_{p,Min.}$ with the separation angle and cavitation angle. For all Reynolds numbers, the angle at which $C_{p,Min.}$ occurred were lower than the separation angle (obtained from wall shear stress, Fig. 19) and

cavitation angle, i.e. $\theta_{C_{p,Min.}} < \theta_{Sep.} < \theta_{Cav.}$. To identify the separation location, the location where the average wall shear stress is zero was obtained on the pin fin surface.
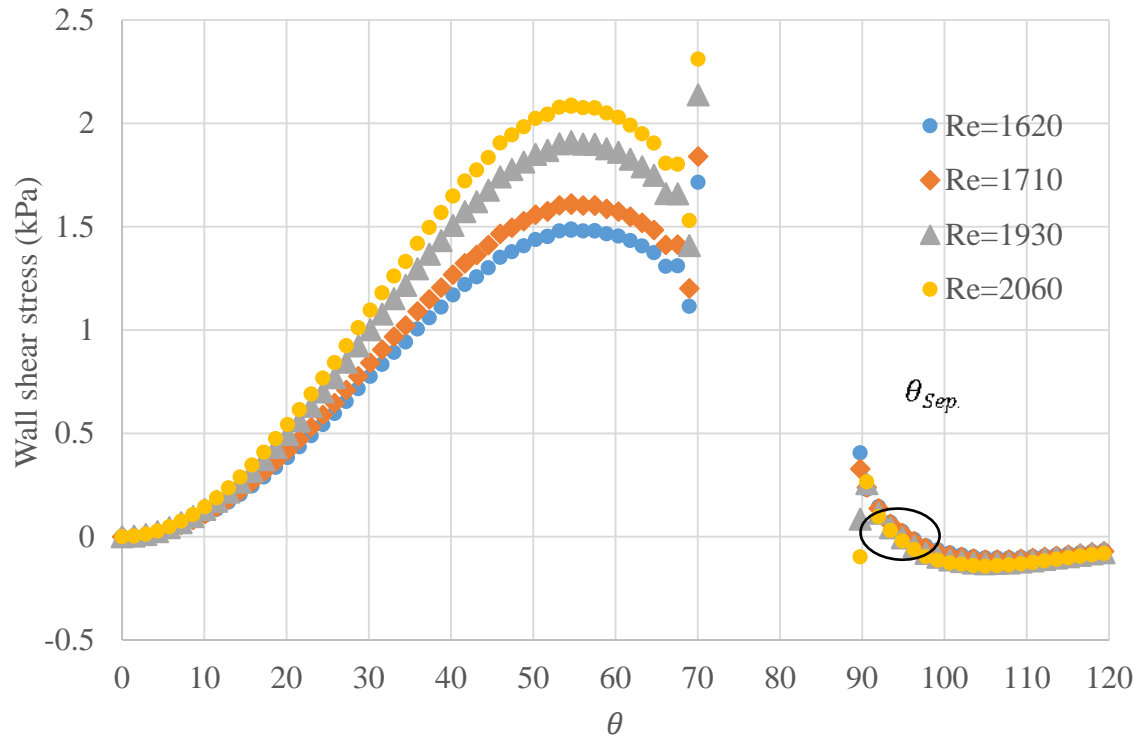
Figure 29 depicts the separation locations on the pin fin mid-plane, which are summarized in Table 3. As expected, flow separated from the pin fin surface at lower angles with increasing Reynolds number. Figure 30 shows instantaneous velocity vector contour in the vicinity of the pin fin and further denotes the flow pattern around the pin fin.
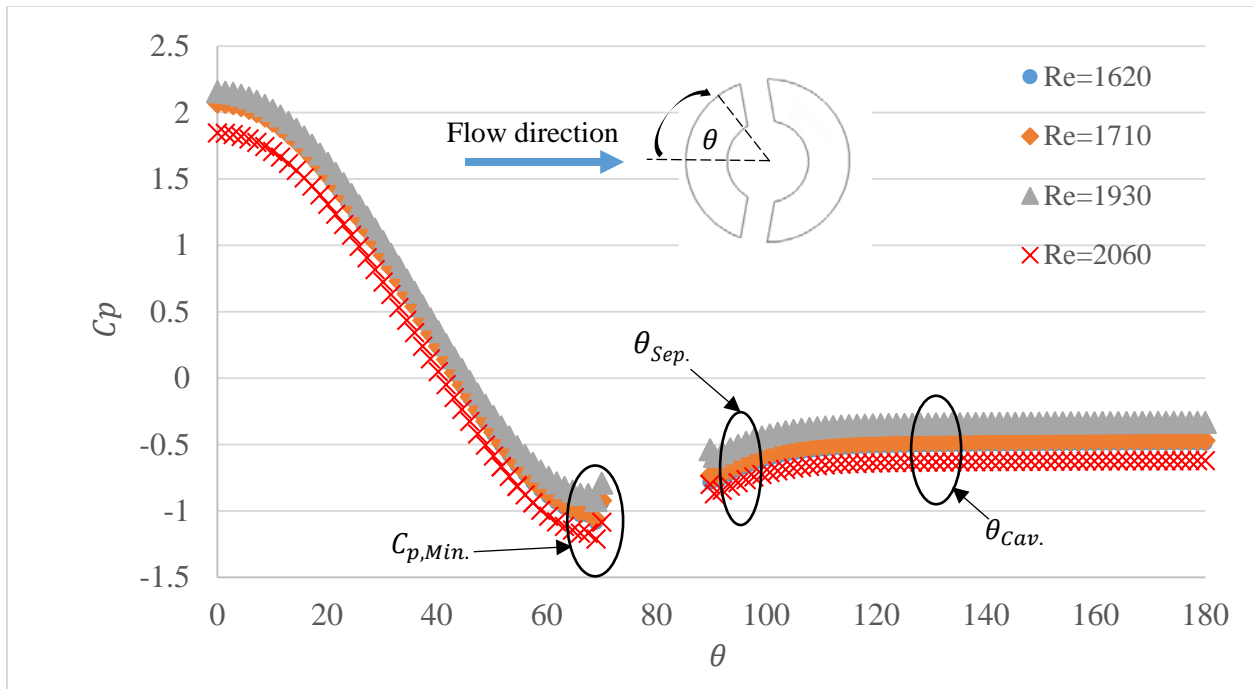
Figure 28: Pressure coefficient around the mid-plane of the pin fin averaged over the last *40000* time steps
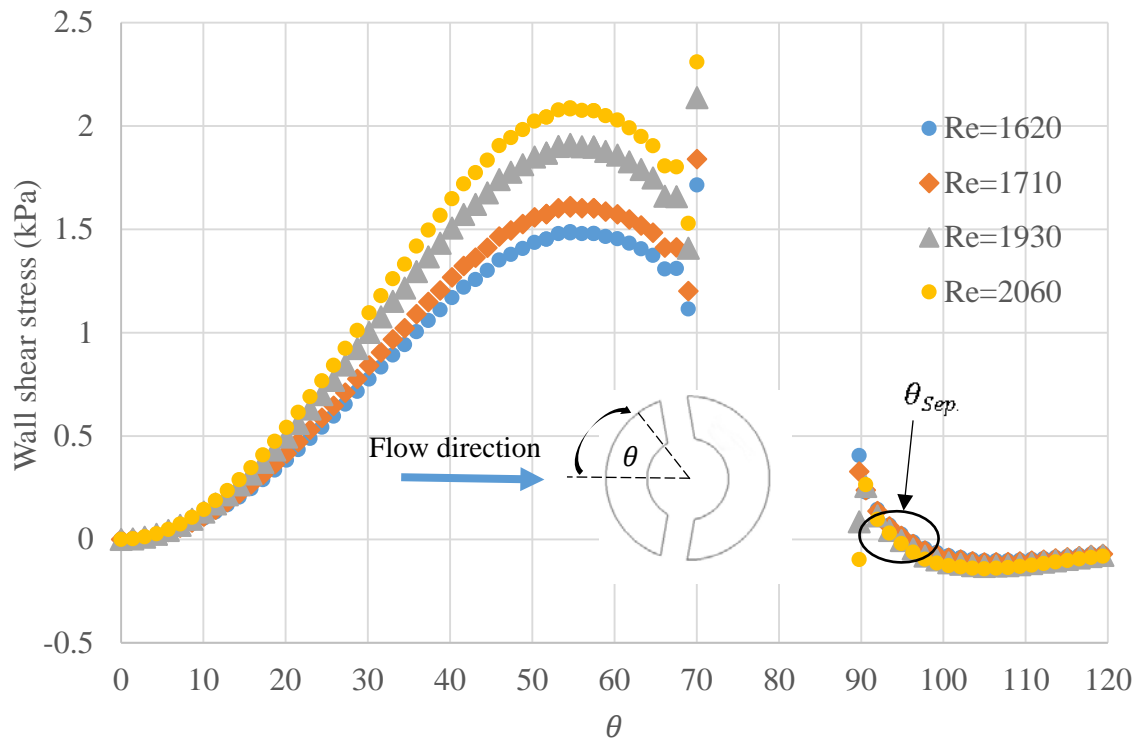
Figure 29: Wall shear stress around the mid-plane of the pin fin averaged over the last *40000* time steps

Table 3: Flow separation angle for different Reynolds numbers averaged over the last *40000* time steps

Re	1620	1710	1930	2060
$\theta_{Sep.}$	$95.88°$	$95.50°$	$94.88°$	$94.76°$

(a)

(b)
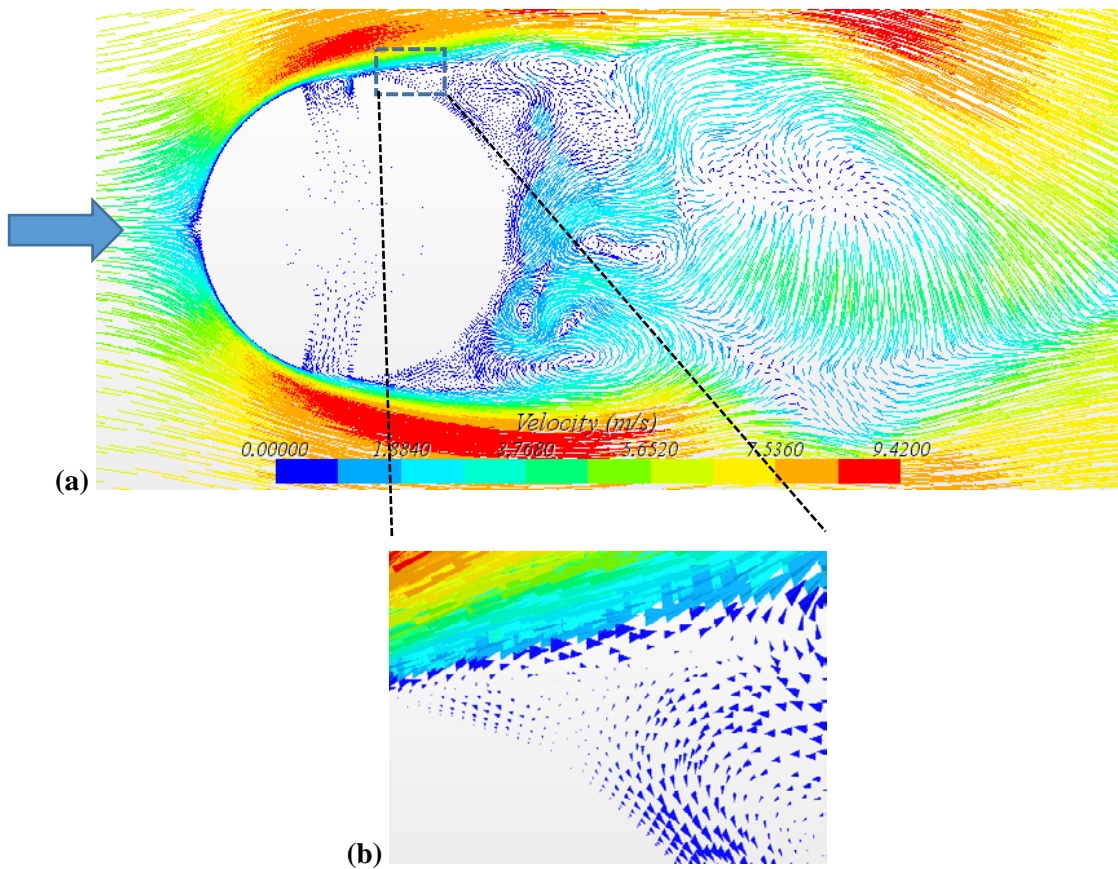
Figure 30: (a) Instantaneous colored contour of velocity magnitude around the pin fin and in the wake area at *Re=2060*, *t=0.07* s, (b) zoom-in view of flow separation zone on pin fin

High speed imagery were carried out to capture cavitation inception events, identify the cavitation inception mechanisms and measure the dimension of cavities downstream the micro pillars. The dominant vapor cavity frequency were determined and were related to vortex shedding frequency.

8.1.2. **Parametric study over various pin fin configurations**

In this section, the outcome of a parametric study is presented. Overall, four different pin fin geometries: circular, triangular, diamond and twin circular were tested.

8.1.2.1. Cavitation inception

A substantial incubation time was witnessed for all pillar geometries before the onset of cavitation. This was attributed to the dominance of surface tension forces that resisted liquid rupture. In addition, the process of degassing before the experiments reduced available stream nuclei. Furthermore, the smooth silicon surfaces (i.e., absence of surface nuclei) in micro domain decreased the availability of surface nuclei. These combined effects coupled with the short fluid's residence time resulted in large incubation time for cavitation inception and low cavitation inception numbers as discussed below. Cavitation inception events were captured through a series of high speed imaging for various pillar shapes (Figure 31). The black regions around the pillars are optical shadows of the intersection between the bottom wall and the pillar. The fabrication process forms a short but gradual expansion of the pillar in the lower most section of the pillar where it meets the bottom wall. The other black regions correspond to regions where vapor/liquid interfaces were formed. Three modes of inception prior to the formation of the attached elongated cavity were revealed including bubble shedding, stationary bubble accompanied by bubble shedding, and an abrupt attached cavity without bubble shedding. For single and twin circular pillars intermittent bubbles shed from the pillars into the wake region and collapsed once reaching a high pressure region downstream.

(a) **(b)** **(c)** **(d)**

Re=2060 *Re=1997* *Re=1616* *Re=1853*
$\sigma_i=2.21$ $\sigma_i=2.74$ $\sigma_i=2.02$ $\sigma_i=1.55$
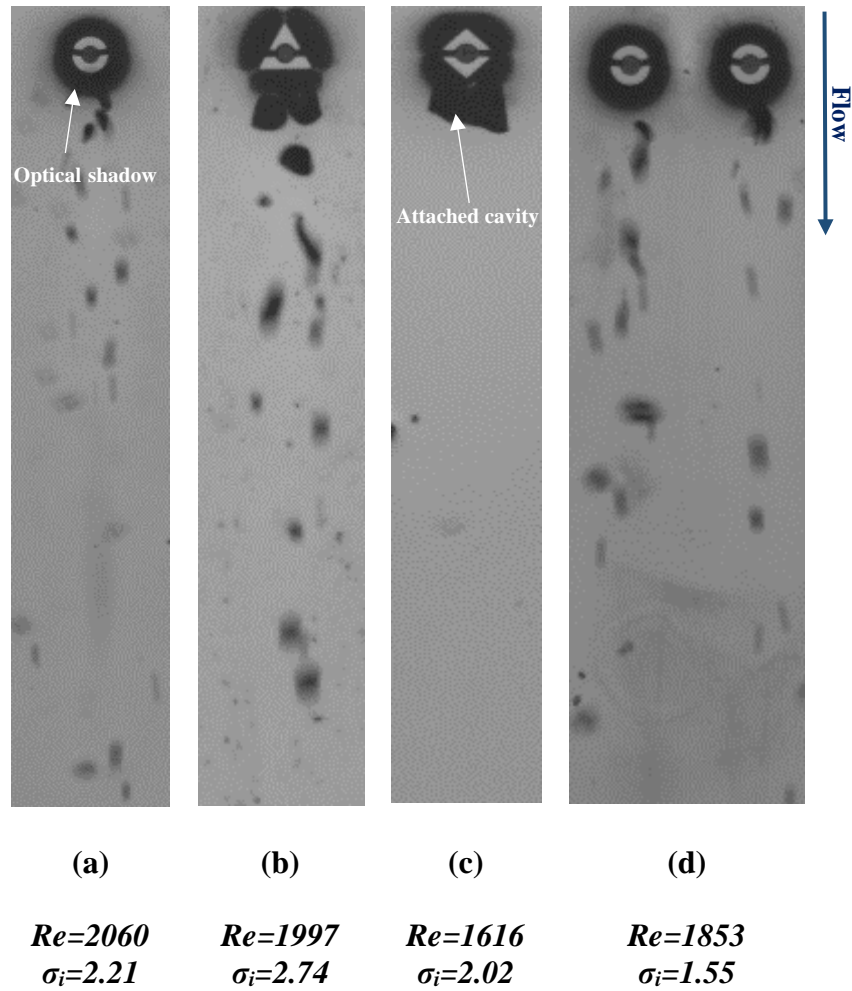
Figure 31: Cavitation inception modes for: (a) single circular pillar — bubble shedding, (b) triangle pillar — bubble shedding accompanied with stationary bubble in the wake region, (c) diamond pillar — sudden formation of attached cavity, and (d) twin circle pillars — bubble shedding

Figure 32 depicts time intervals of cavitation inception process for the triangular pillar. A distinct bubble adjacent to the pillar was observed in the wake region for a substitutional long time. In addition, sporadic bubble shedding from both sides of the pillar was observed. The cavitation inception pattern seen for the triangular pillar may be attributed to a specific flow field downstream of the pillar as reported in [102] and [103]. They identified three types of cavitating vortices: near-wake vortices, the primary two dimensional Kármán vortices, and secondary three dimensional streamwise vortices. In addition, three distinct wake regions were found to preside downstream of a wedge (Figure 33). The near-wake region is responsible for

abiding the bubble that was witnessed in the experiment. The diamond shape pillar showed no bubble shedding prior to the formation of the attached elongated cavity.
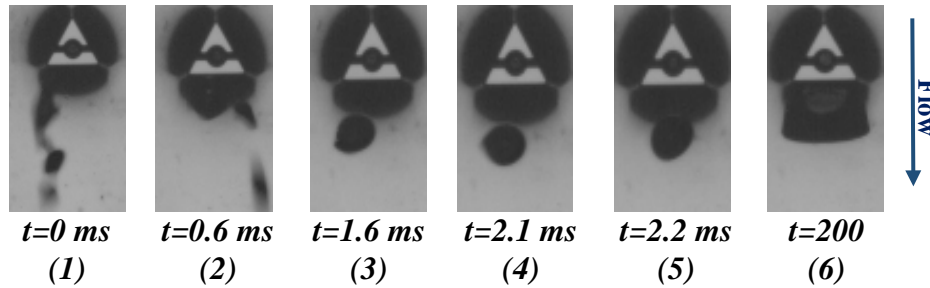
Figure 32: High speed camera images demonstrating cavitation inception modes and time instances downstream a triangular pillar (1, 2): intermittent attached cavity and bubble shedding from both sides, (3, 4, 5): separated cavity vapor moving in the wake region, (6): formation of attached cavity, Re=1997, σ_i=2.74.

Figure 34 depicts cavitation inception numbers as a function of Reynolds number for the micro pillars. The variations in the inception number are within the measurement uncertainty throughout various Reynolds numbers (except for the first data point of the diamond pillar), which confirms the independency of cavitation inception number and the Reynolds number. This observation correlates well with previous studies on cavitation in orifices at the macro scale [104] and micro orifice entrenched in microchannel [3], but contradicts results by [105] who showed a monotonically increasing cavitation inception number with Reynolds number around 2×10^6 for sharp-edged circular disks. The highest cavitation inception numbers among all configurations were seen for a triangular pillar. Similar results were obtained by Rammamurthy and Bhaskaran [106] for two dimensional triangular and circular elements under cavitating condition; they reported high cavitation inception numbers for the two triangular cases (refer to Table 2). The formation of a distinct wake region illustrated in Figure 33 suggests that the high cavitation inception numbers is related to the presence of shear layer vortices in the near-wake region. The vortex cores provided low pressure regions that triggered the inception of cavitation even in high system pressures leading to a higher cavitation inception numbers in the triangular pillar.
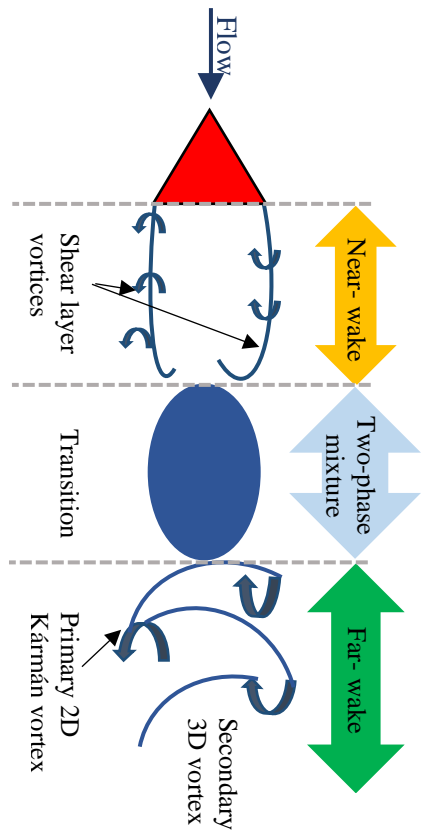
Figure 33: Top view sketch of the wake region downstream a triangular bluff body. Near-wake region with shear layer vortices, a transition region, and a far-wake region with 2D and 3D primary and secondary Kármán vortices, adopted from [102].
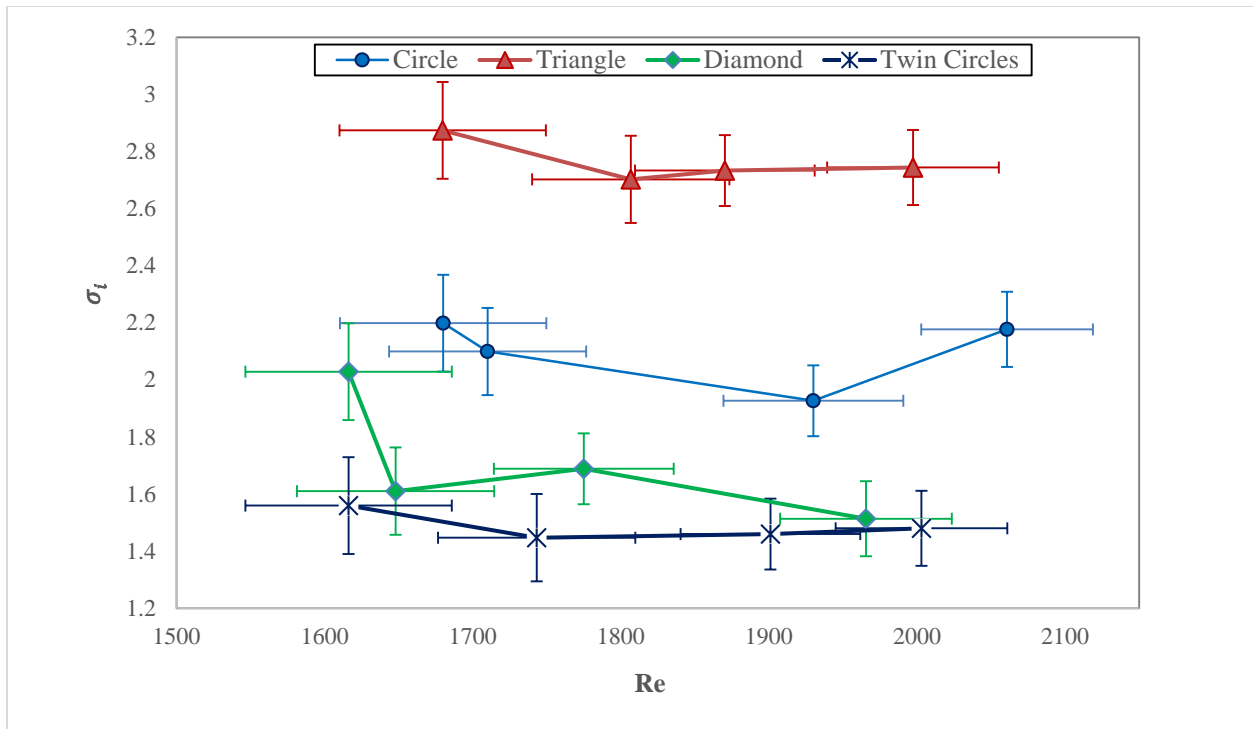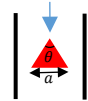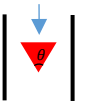
Figure 34: Comparison of cavitation inception numbers at various Reynolds numbers for four pillar configurations
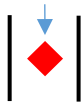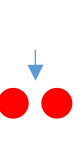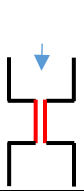
The inception cavitation numbers for a range of constriction elements along with their geometrical information and test conditions are summarized in Table 4. A comparison between the cavitation inception numbers for micro and conventional scales denotes relatively lower inception numbers at the micro scale. At the macroscale, several studies postulated that the availability of stream nuclei rather than surface nuclei dominates the onset of cavitation. This may not be the case at the microscale in which surface nuclei are more likely to initiate cavitation [3]. Nevertheless, the influence of stream nuclei was partially eliminated here via degassing process and filtering of large size particles as explained earlier. In addition, the microchannel and the pillar/s were made of silicon with a relatively smooth surfaces. Qu et al. [107] measured the roughness of a polished Pyrex test wafer, used as a top channel wall, and the surface roughness of microchannel side and bottom walls (made of silicon), and found them to be of the order of 10 nm and less than 2 μm, respectively. Another study by Vengallatore [108] stated that the surface roughness of

microchannel silicon wall depends on the deep reactive ion etching (DRIE) process, which results in scalloped sidewalls with a roughness of ~0.3 μm. The lack of stream and surface nuclei significantly delayed the onset of cavitation. Thus, the static pressure in the vicinity of the pillars needs to be much reduced in order to trigger cavitation, which in turn, results in low cavitation inception numbers at the micro scale.

Comparison among various micro scale domains reveals that micro orifices and micro venturis yielded low cavitation inception numbers. This may be associated with the nature of flow in orifice and venturi wherein abrupt velocity increase and pressure drop lead to low cavitation inception numbers.

Table 4: Mean cavitation inception numbers (σi) for various micro and macro scale constriction elements

Constriction cross section		Mean cavitation inception number (σ_i)		
		Present study (B.R.=0.1, A.R.=1.5)	Previous studies	
			Microscale	Macroscale
Circle		**2.1** (D=150 μm)	-	**4.25** [60] (D=20 mm, B.R.=0.5)
				3.7 (Kumar et. al) (D=10 mm)
				[106] I) **4,** (D=25.4 mm, B.R.=0.165, A.R.=0.24, Re= 1-5× 10^5) II) **3.3,** (D=50.4 mm, B.R.=0.327, A.R.=0.12, Re= 3-8× 10^5)
				10, [109] (D=40 mm, B.R. =0.5. A.R.=0.5, Re= 1.2× 10^5)
				[110] **3.07** (D=10 mm, B.R.=0.125)
Triangle I		**2.76** (a=202 μm)	-	[106] $\theta = 60°$ I) **6**, (a=15.9 mm, B.R.= 0.103, A.R.=0.38) II) **6.8**, (a=30.2 mm, B.R.= 0.196, A.R.=0.2) III) **8**, (a=50.2 mm, B.R.= 0.326, A.R.=0.12)
				[111] I) **6.18**, ($\theta = 90°$) (Re=1.7×10^5) II) **5.40**, ($\theta = 60°$) (Re=1.7×10^5) III) **3.90**, ($\theta = 30°$) (Re=1.8×10^5) IV) **2.95**, ($\theta = 15°$) (Re=1.9×10^5)
				[102] **3.72**, $\theta = 25°$ (a=35 mm, B.R.=0.2, Re=3×10^5)
Triangle II		-	-	[106] $\theta = 60°$ I) **5.2**, (a=15.9 mm, B.R.= 0.103, A.R.=0.38) II) **5.9**, (a=30.2 mm, B.R.= 0.196, A.R.=0.38) III) **7**, (a=50.2 mm, B.R.= 0.326, A.R.=0.38)

Diamond		**1.70** (a=133 μm)	-	-
Twin circles		**1.49** (D=150 μm, G=450 μm)	-	-
Orifice (diaphragm)		-	I) **0.284** [3] (d_h^*=20.65μm) II) **0.32** [31] (d_h=74-104 μm)	I) **1.10,** [104] (d_h=2.96×10^{-2} m) II) **1.95,** [112] (d_h= 1.70 × 10^{-2} m)
Venturi		-	I) **2.51,** [40] (d_h=34.77μm) II) **0.47,** [31] (d_h=51-82 μm)	-

**Orifice hydraulic diameter

8.1.2.2. Cavity characteristics in various pin fin geometries

Figure 35 shows top-view images corresponding to fully developed cavities behind the pillars. The gray scales that are projected from the cavity provide a qualitative measure about the cavity relative position in the channel. The white regions surrounded by black region correspond to regions in direct contact with the top wall. A qualitative comparison based on the image gray level demonstrates that the triangular pillar has the largest white region and the twin circles have the smallest, suggesting that most of the cavity inner volume of the triangular pillar was in direct contact with the channel top wall. In addition, comparing the black regions surrounding the white regions reveals that its cavity is longer and wider. A survey over 2000 images for each pillar was conducted and is presented in the subsequent section.
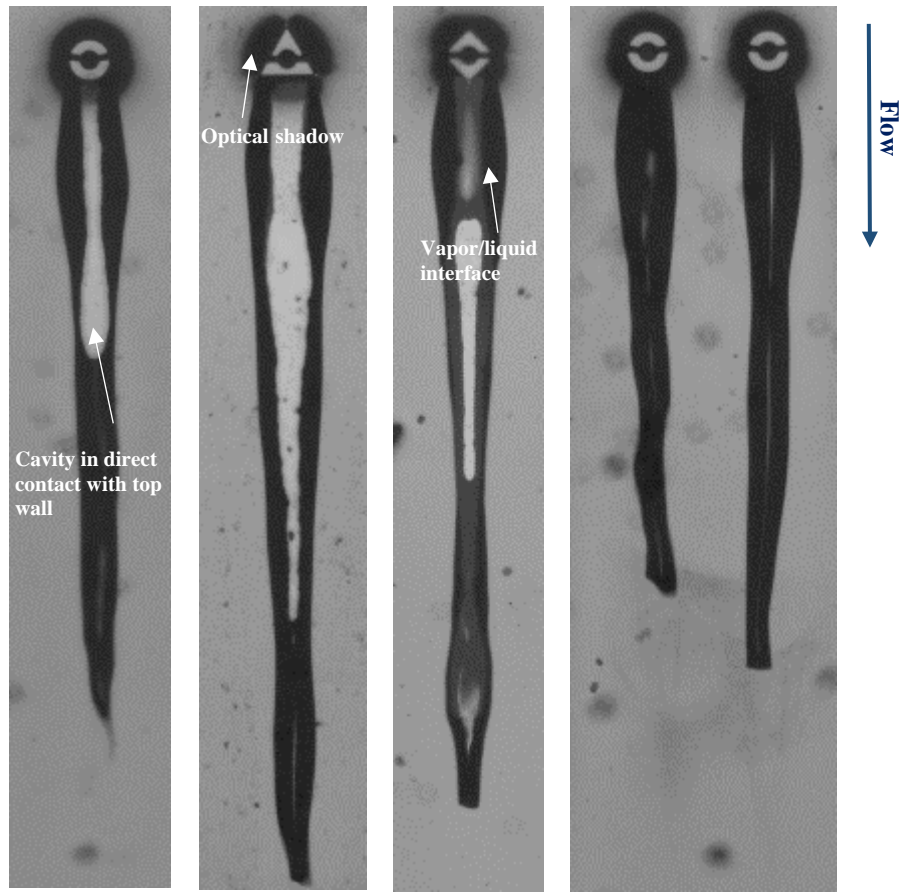
(a) **(b)** **(c)** **(d)**

Re=2060 *Re=1997* *Re=1616* *Re=1853*
σ_i=2.21 *σ_i=2.74* *σ_i=2.02* *σ_i=1.55*

Figure 35: Snapshots of elongated cavity formation for (a) a single circle pillar, (b) a triangle pillar, (c) a diamond pillar, and (d) two circular pillars. The gray scale denotes cavity relative position in the channel.

To study the influence of the cavitation number on the vapor cavity length, the pressure difference between the inlet and exit manifolds was varied. The inlet tank pressure was kept at zero gauge while the outlet tank was vacuumed. The first data points were recorded once a stable attached cavity was formed. Subsequently, the inlet pressure (and consequently pressure difference and Reynolds number) was repeatedly increased by introducing helium gas into the inlet tank. As presented in Figure 36, cavitation numbers were maintained at almost identical values for circular, diamond and to some extent triangular pillars while cavity lengths varied. This was mainly ascribed to the simultaneously increase of pressure difference and velocity so that cavitation numbers did not vary significantly.
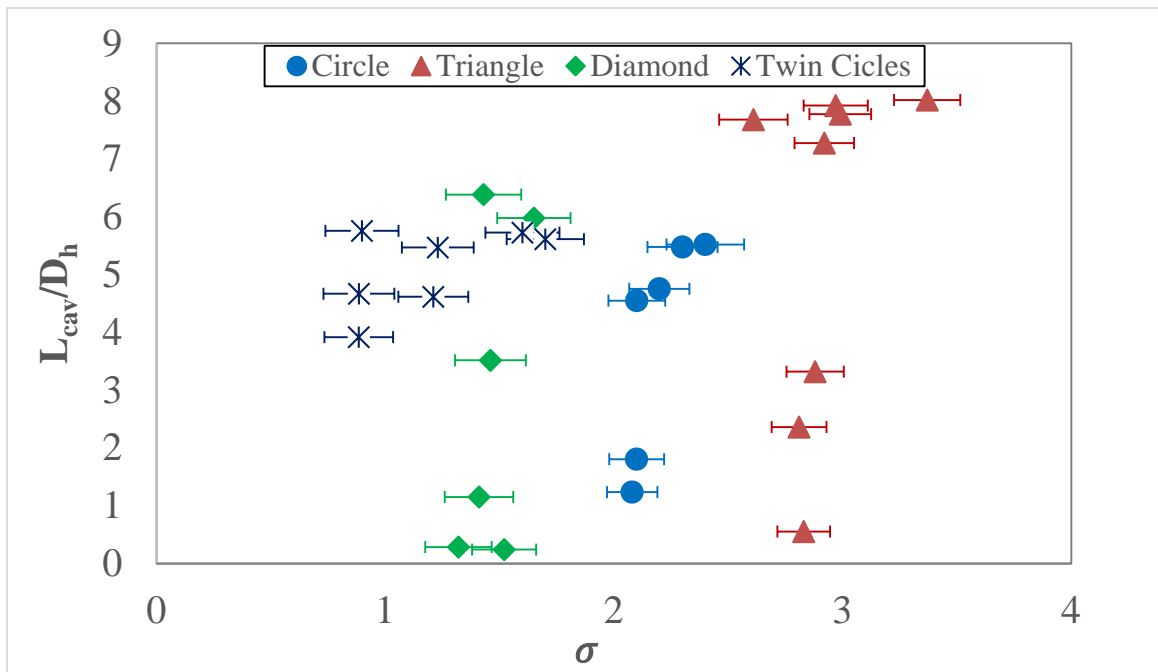
Figure 36: Dimensionless vapor cavity length as a function of cavitation number for four configurations. Cavity lengths are not strong functions of cavitation number. Attached cavity length averaged over 2000 frames. For the twin circles, the average length of the two cavities were calculated.

In order to identify the factor controlling cavity length, pressure effects were explored. Figure 37 compares averaged cavity lengths for various configurations as a function of system pressure. System pressure refers to the pressure measurement in the vicinity of the vapor cavity (P_p). Despite negligible change of the cavitation number for all pillar geometries, cavity lengths changed with system pressure. The dependency of cavity length on system pressure seemed to be stronger for circular and square pillars as the curves demonstrated a steeper slope. The triangular pillar had the longest cavities at low system pressure before it contracted around $P_{Sys.} = 57\ kPa$. This can be linked to the width of the near wake regions formed behind sharp edged bluff bodies as suggested by [113] wherein the cavity is attaches to the sharp edges of the bluff body. Also, sharp vertices lead to larger low pressure regions that promote the formation of highly stable cavitation regions that are less susceptible to the variation of system pressure. The triangular pillar had the largest characteristic length of 202 μm, corresponding to the widest wake region. The attached cavity behind the triangular pillar stretched the most and was persistent under a range of flow conditions ($35 \leq P_{Sys.} \leq$ 63 kPa). Also, the cavity existed over the largest system pressures range in the triangular pillar suggesting it is less sensitive to a change in the flow field. A sudden transition of the vapor cavity length was observed at a distinct cavitation number, but it varied depending on the pillar shape. The two circular pillars showed a more gradual variation in the cavity size compared to the other geometries suggesting that once a cavity is formed it is likely to persist without appreciable change in the cavity length. For the other three pillar geometries, the cavity collapsed abruptly once certain hydrodynamic condition developed. Besides the triangular pillar, the diamond pillar resulted in the longest cavity. Also, the circular and the diamond pillars brought about cavitation occurrence over almost the same range of system pressure.

The angle at which the cavity is attached to the pillars ($\theta_{Cav.}$) was measured using image analysis software (ImageJ) and was averaged over a range of Reynolds numbers. The angle is measured from the centerline of the pillars as shown in Table 5 where the cavity attachment angles were compared for four pillar geometries. Note that the optical shadow around the pillars made it impossible to measure the exact angles

and therefore, the angles were measured with respect to the edges of the optical shadows. For the twin circles, the average angle was calculated. Larger cavity angles were seen for single and twin circular pillars whereas relatively small attachment angles were recorded for the triangular and the diamond pillars. Cavity detachment process on a smooth body, i.e., single and twin circular pillars, is often called smooth detachment and is affected by the location of the boundary layer separation upstream of the cavity [114]. The gradual change in the solid body curvature causes the flow to separate at higher angles. Since the height of the microchannel and pillars was 225 µm, the boundary layer of the pillar and the boundary layer of the channel wall interacted, modifying the cavity formation position. Although semi-empirical correlations and attachment criteria were proposed by [63,114] to link the locations of the cavity attachment and flow separation on unconfined smooth bodies in conventional scales, no similar study provided such correlations for short pillars at the micro scale. For configurations with sharp corners, such as triangular and diamond, the cavitation attachment locations are fixed by the geometry of the macroscale body as suggested by [114]. The lower cavity attachment angles may be attributed to the discontinuity of the solid boundary curvature gradient around the sharp corners that generate local low pressure regions that led to the attachment of cavity in the vicinity of sharp corner.
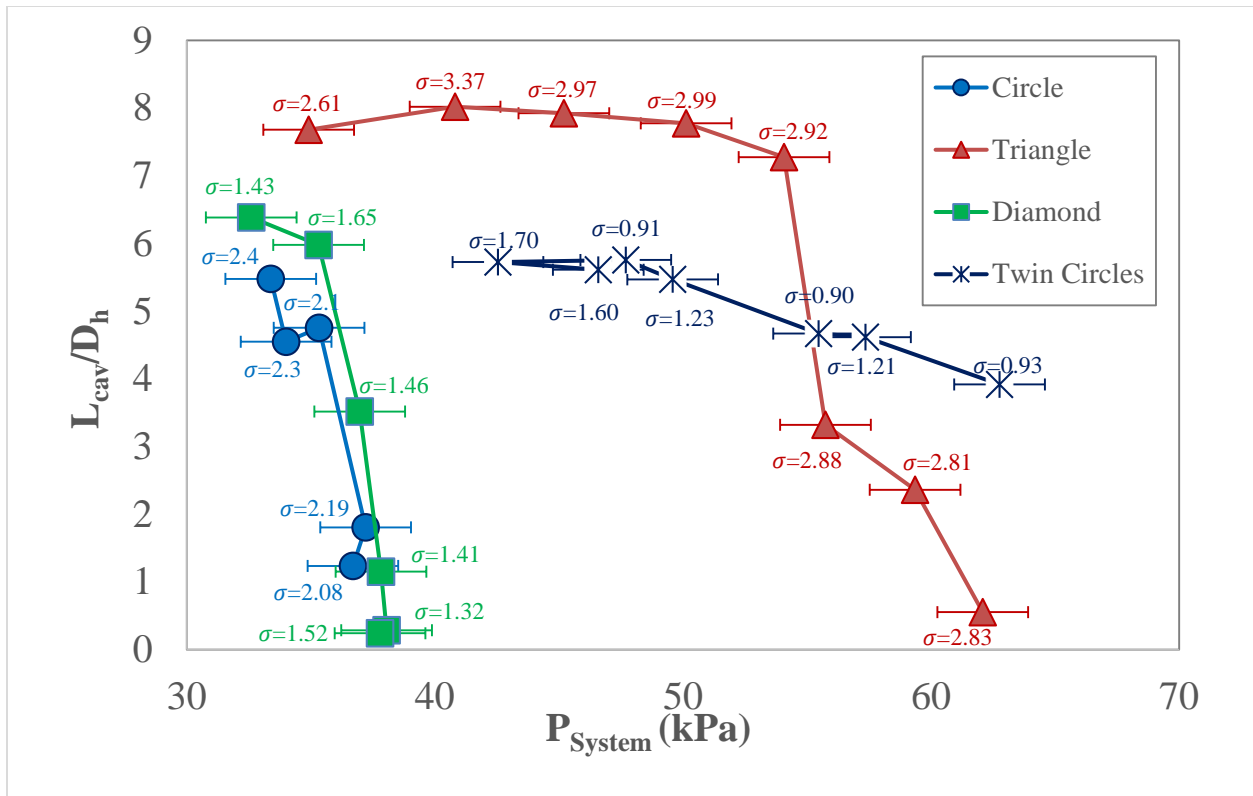
Figure 37: System pressure effect on the length of attached cavity for the various pillars studied. Numbers show the pertinent cavitation numbers for each case.

Table 5: Cavity attachment angle measured from the pillar centerline at incoming flow and averaged over Reynolds numbers

Pillar Shape	Circle	Triangle	Diamond	Twin Circles
	135°	123°	126°	140°
Average cavity attachment angle ($\theta_{Cav.}$)				

8.1.2.3. Flow pattern over twin circle pillars

For twin parallel circular cylinders, the longitudinal and transverse spacing between the cylinders and the Reynolds number specify the near-wake flow structure and have a strong effect on the flow parameters like drag forces and vortex shedding. Since attached cavities are formed mostly in the wake region, their characteristics are also affected by the cylinders' spacing. Depending on the gap between the cylinders (γ =Δ/D), three scenarios are likely to occur [115]: For $1 < \gamma < 1.1 - 1.2$, the two cylinders act like a single bluff body and a single Kármán vortex street is shed from the cylinders. At intermediate pitch ratio, $1.1 - 1.2 < \gamma < 2 - 2.2$, asymmetrical or biased flow pattern forms, which bends toward one of the two cylinders [116]. At higher pitch ratio ($\gamma > 2 - 2.2$), parallel Kármán vortex streets form symmetrically over each cylinder at the same frequency. Although the abovementioned classification were reported for infinite and unconfined cylinders, it provides a general framework pertinent to the flow pattern in the current study. The two cylinders studied here falls into the latter regime (γ =3). Anti-phase synchronization between the Kármán vortices are the predominant mode as depicted in Figure 38 although intermittent in-phase shedding [116] and in some cases irregular sporadic shedding [117,118] were reported.

Figure 39 depicts the image of the attached cavity where one cavity is always longer than the other. This trend was seen for all cases for all Reynolds numbers and cavitation numbers studied. Since the vapor cavities were situated in the near wake region of the cylinders, their movements was dominated by anti-phase synchronization. However, the result in the current study shows that the transverse movement of the vapor cavity shifted among irregular, anti-phase, and in-phase modes. One possible speculation is that short confined pillars affect the vortex shedding mechanism that led to an abrupt mode shift in the cavity transvers movements.
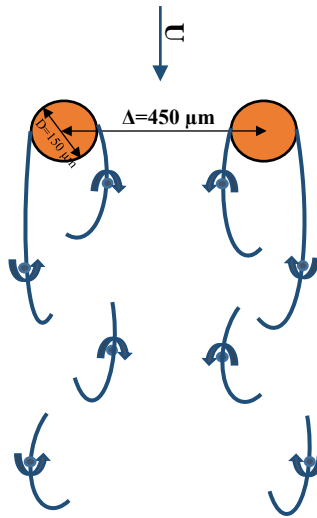
Figure 38: Schematic view of flow pattern behind twin cylinders placed side-by-side with the dominant vortex shedding mode of "anti-phase".
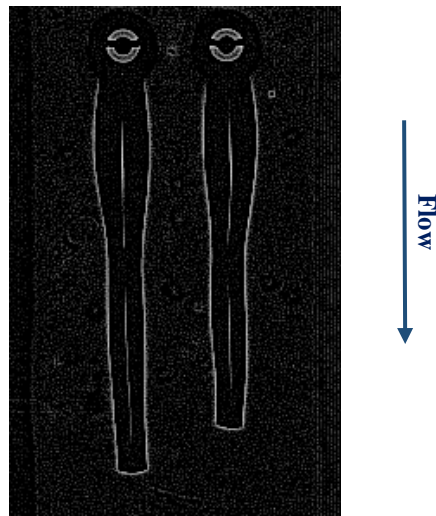
Figure 39: Filtered image showing attached cavities. Side white lines show the edge of cavity pocket while the middle lines correspond to the locations where the cavity is attached to the top channel wall, Re= 1853

8.1.2.4. Spectral analysis of cavity images

Several previous studies on cavitating flows used high speed digital videos to quantify cavitation through spectral analysis [45,69,119]. Measuring and analyzing gray scale intensity variations in a spatiotemporal domain is a quantification technique used to extract information about cavity dynamics. In the present study, images of elongated attached cavities were sampled with a frequency of 20000 frame per seconds (fps). For each pillar shape, videos compromising 2000 frames that captured sequentially were implemented for greyness intensity analysis.

Gray intensity of each pixel is assigned based on a spectrum ranging from 0 to 255. Intensity of 0 corresponds to a black pixel while a value of 255 corresponds to a white pixel. To capture cavitation oscillatory behavior, time series of average gray intensities was transformed into frequency domain using Fast Fourier transform (FFT). Pixels including the edge area of the moving cavity were coded based on their greyness or image brightness. Time series of pixels were associated with high frequency noise that were filtered here. Fluctuations of average gray scale intensity is related to the oscillating behavior of the cavity. The vapor cavity was developed in the vortex street generated from fluid-pillar interaction. Based on previous studies summarized in the introduction section, it can be assumed that the characteristic frequency of the cavity movement and vortex shedding frequency are well correlated and measuring cavitation frequency using image processing techniques can be used to infer vortex shedding frequency.

Figure 40 depicts the FFT spectra of the brightness intensity time series obtained from the videos of the circular, triangular, and diamond pillars. The peak amplitudes for the circular pillar corresponded to a frequency of about 3500 Hz. The equivalent Strouhal number for this frequency is $St = \frac{f.D}{V} = 0.13$ while available literature [48] suggested a non-cavitating Strouhal numbers near 0.2 for unconfined macro scale cylinder. The reduced Strouhal number might be associated with the influence of cavitation and also the dampening effect of confinement (i.e., endwall effects) on the vortex shedding. The shape of the bluff body

is one of the primary factors in determining vortex shedding characteristics including its dominant frequency [120]. As shown before in Fig. 7, the specific wake region and distinct vortical structures downstream a triangular pillar results in a different cavitation behavior. Past studies on sharp edge wedge cavitating vortices [102,111] suggested Strouhal numbers range of $St \geq 0.2$ whereas we captured low dominant frequencies and corresponding Strouhal numbers of $St \leq 0.1$ that may be due to confinement effect and also a unique interaction between vortices and cavitated regions downstream sharp-edged micro bluff bodies that suppresses vortex shedding more than for a smooth shape body. As mentioned earlier, vortex shedding and cavity oscillation are not two independent phenomena and the reduction seen in the dominant frequencies can be ascribed to lower vortex shedding frequency of these configurations.
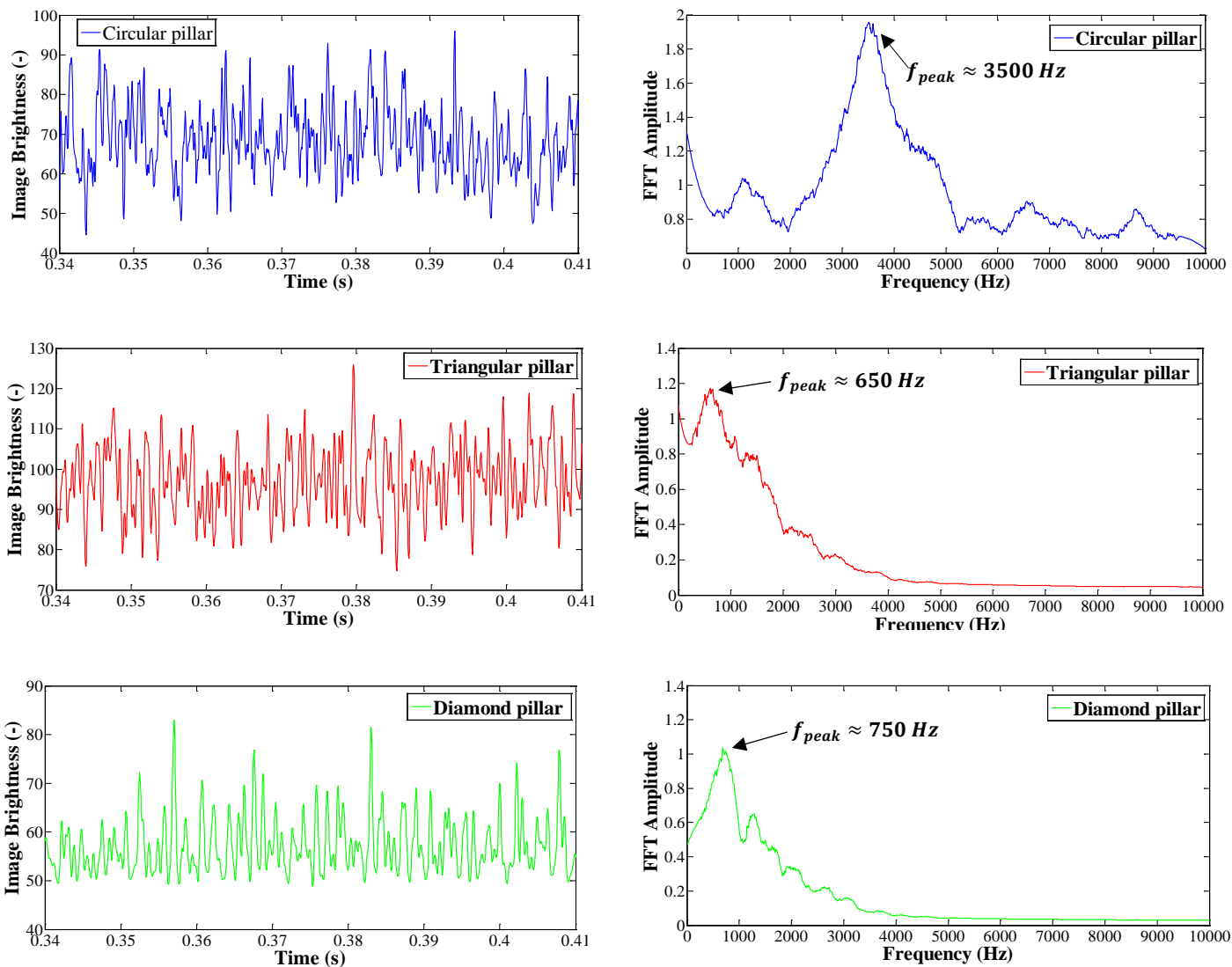
Figure 40: Time history of image brightness content for circular, triangular and diamond pillars (left column), and the corresponding FFT amplitude spectrum of image brightness (right column).

8.2. Heat transfer over micro pin fin arrays

In this chapter, a series of experimental measurements and numerical simulations are presented to evaluate the influence of a single pin fin array with two pin fin geometries on the enhancement of heat transfer. The approach presented in the current study is an intermediate step between a single pin fin and pin fin arrays. Specifically, in this effort the flow is only interrupted in the direction perpendicular to the flow direction. Two micro devices with a single row of hydrofoil and circular micro pin fins inside a microchannel were experimentally and numerically studied. The flow structure was examined and its effect on the heat transfer process was revealed. To mitigate the effect of solid conduction, microchannel and pin fins were fabricated using a permanent photoresist material (SU-8 100) with low thermal conductivity (k=0.3 W/m·K). To further reduce heat losses through the solid substrates, the microchannel was formed by sandwiching two Pyrex substrates between the SU-8 layers. All the materials used in the micro-device fabrication were transparent enabling full flow visualization. Experimental results were complemented by a conjugate fluid/heat transfer modeling in order to link the flow structure to the heat transfer process.

8.2.1. Flow patterns

The convective heat transfer process is closely related to flow structure. As such, the numerical simulation aimed to reveal this dependency through a detailed analysis of the flow structures including the wake regions, flow stagnation, flow acceleration, and flow deceleration that occur in the vicinity of pin fins. The flow patterns for the circular pin fin arrays and the hydrofoil arrays are discussed separately.

8.2.1.1. Flow field in circular pin fin

Flow around a single bluff body is dominated by vortex shedding, which depends on the Reynolds number. In wall-bounded flows, such as those encountered in microchannel, wall interference affects the structure and the inception of vortex shedding [100,121,122]. In the current study where a row of circular pin fin

72

exists, the interaction of vortex shedding was controlled by the pin fin crosswise distances as predicted by

Sumner et al. [115,117]. Sumner also observed four different flow patterns for three-side-by-side circular

cylinders. Namely, a single bluff-body asymmetric biased flow for $1< T/D < 1.1 - 1.2$, symmetric biased

flow pattern (likely with synchronized vortex shedding) at intermediate T/D values,

$1.1 - 1.2 < T/D < 2.2$, and synchronized vortex shedding for $T/D > 2.2$. In the current study, T/D

corresponded to the intermediate range where symmetric biased flow exists, and the flow through the gap

is tilted towards one of the cylinders (Figure 41). This results in a narrower wake region (NW) downstream

the cylinder towards which the flow is deflected and a wider wake (WW) downstream of an adjacent

cylinder is formed. In addition, two dominant vortex shedding frequencies were measured for the biased

flows.
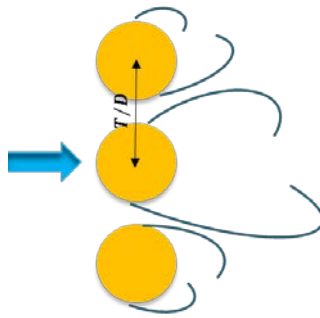
Figure 41: Schematic representation of symmetric biased flow pattern over three side-by-side cylinders when $1.1 - 1.2 < T/D < 2.2$

Figure 42 shows the mean velocity magnitudes contours in three longitudinal planes with the vertical

dimensionless distances of y/H=0.1, 0.25 and 0.5 from the heater surface for three Reynolds numbers.

Except for the case of Re=294, which was simulated by assuming steady state, other contours were

averaged over substantial amount of time steps. For the case of Re=262, a distinct wake region is witnessed.

Particularly, the length of the wake regions alternate tandemly. This behavior was seen in all the

longitudinal planes suggesting the presence of the pattern throughout the entire height of channel as shown

in Figure 43 where velocity magnitudes in a vertical plane downstream the pin fins were presented.

Increasing y/H and approaching the channel mid-channel plane resulted in diminished wake regions for all the Reynolds numbers considered in this study. At Reynolds numbers of 794 and 1024, the two wake regions adjacent to the microchannel side walls were enlarged and made the nearby flow tilted toward the microchannel wall. This behavior is was more pronounced at Re=1026. While many similarities were observed between the current micro scale study and conventional scale studies, the flow pattern observed in the current study exhibited some deviations from the previous macroscale studies, as depicted schematically in Figure 41 where end-wall effects were not considered. The confinement of the pin fins from the top and bottom walls together with the downsizing effect from macro to microscale might justify these discrepancies.

$Re_{Dh} = 294$

(a) (b) (c)

$Re_{Dh} = 794$

(d) (e) (f)

$Re_{Dh} = 1024$

(g) (h) (i)

$y/H = 0.1$ $y/H = 0.25$ $y/H = 0.5$
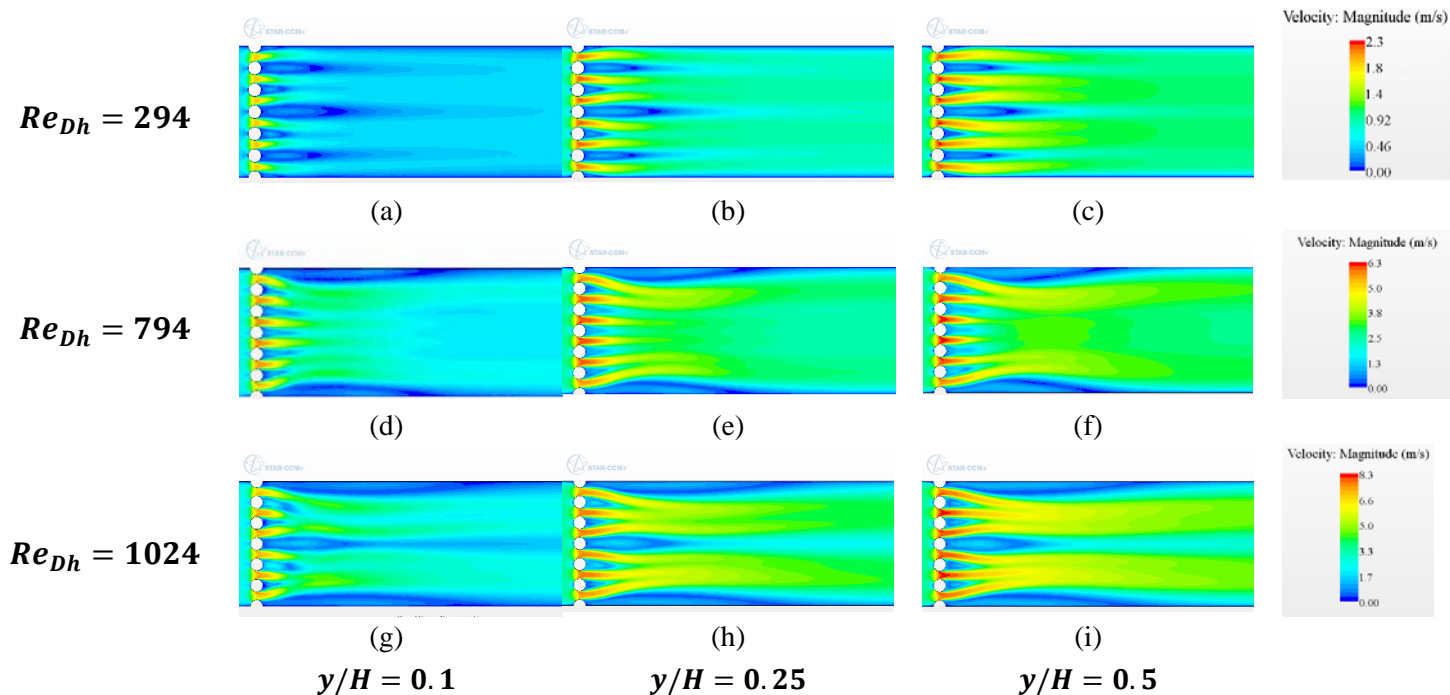
Figure 42: Mean velocity magnitude contours in the vicinity of the pin fins at various vertical distances from the heater surface (y/H); (a), (b) and (c) are for steady state, the rest of the contours were simulated using a transient approach with appropriate time steps, and the velocity was averaged over 20000 time steps.
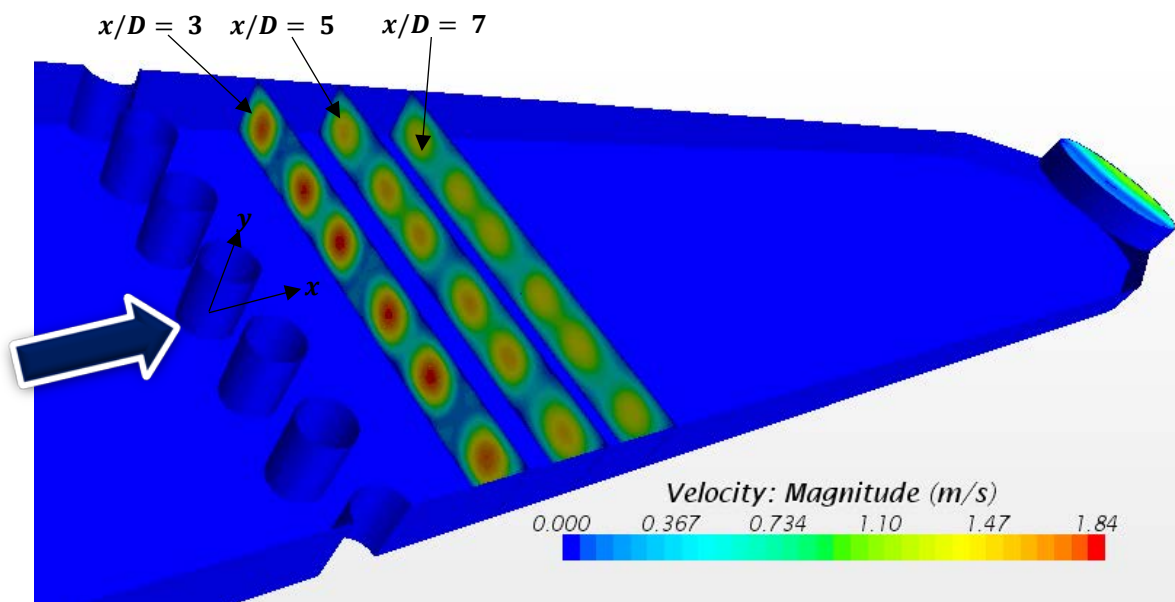
Figure 43: Vertical velocity magnitude contour in three planes of $x/D = 3, 5, 7$ downstream the pin fins.

Biased flow is clearly shown in Figure 44 where an identical numerical approach led to two distinct flow patterns. The flow pattern for both are symmetric with respect to the microchannel center line. The unsteady vortex shedding led to a bi-stable (flip-flop) flow pattern with a shift in the wake length. This phenomenon is an intrinsic characteristic of such configuration and is reported in detail in previous studies [123–126].
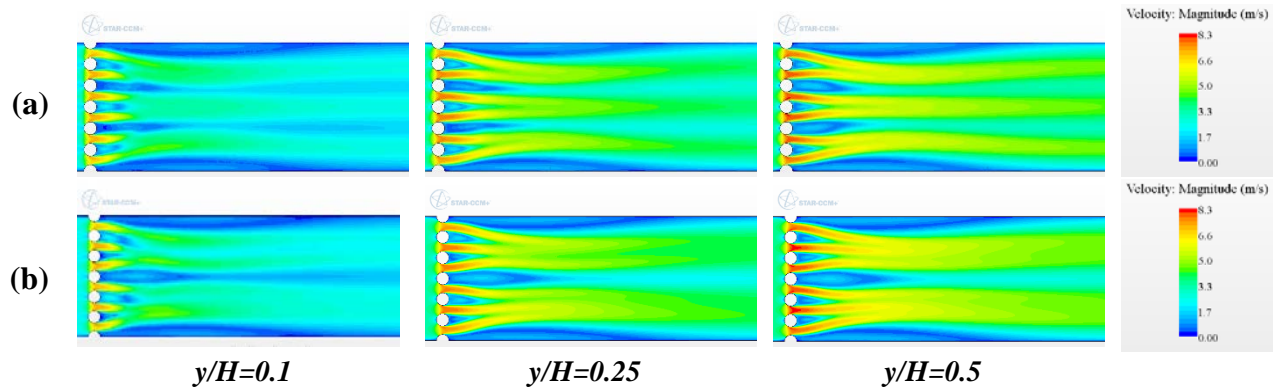
Figure 44: Flip-flop behavior of wake regions: mean velocity magnitude contour for Re=1026 at a time step of 0.1 ms (a) and a time step of 0.11 ms (b).

8.2.1.2. Flow field on hydrofoil

Contrary to bluff bodies, hydrofoil is a slender body with a low flow resistance. Studies on hydrofoil vortex shedding is limited to unconfined single hydrofoil at Reynolds numbers of $Re > 10^6$ based on chord length [127,128]. Figure 45 shows the flow field for three Reynolds numbers, $Re = 262, 794, and\ 1026$. The hydrofoil zero-angle of attack resulted in an attached flow over pin fin surfaces with a relatively shorter wake regions compared to circular pin fins. In addition, the biased flow was not observed at Re=262 and only appeared at the two higher Reynolds numbers and at lower intensities in comparison to the circular pin fins. This is attributed to the extent of the separated region formed over the pin fins; for the circular pin fins, the separated flow is covered over a substantial portion of their surfaces and hence forms an unstable wake region with vortex shedding even at a low Reynolds number.

$$Re_{Dh} = 294$$

$$Re_{Dh} = 792$$

$$Re_{Dh} = 1024$$

| (a) | (b) | (c) |

| (d) | (e) | (f) |

| (g) | (h) | (i) |

$$y/H = 0.1 \qquad\qquad y/H = 0.25 \qquad\qquad y/H = 0.5$$
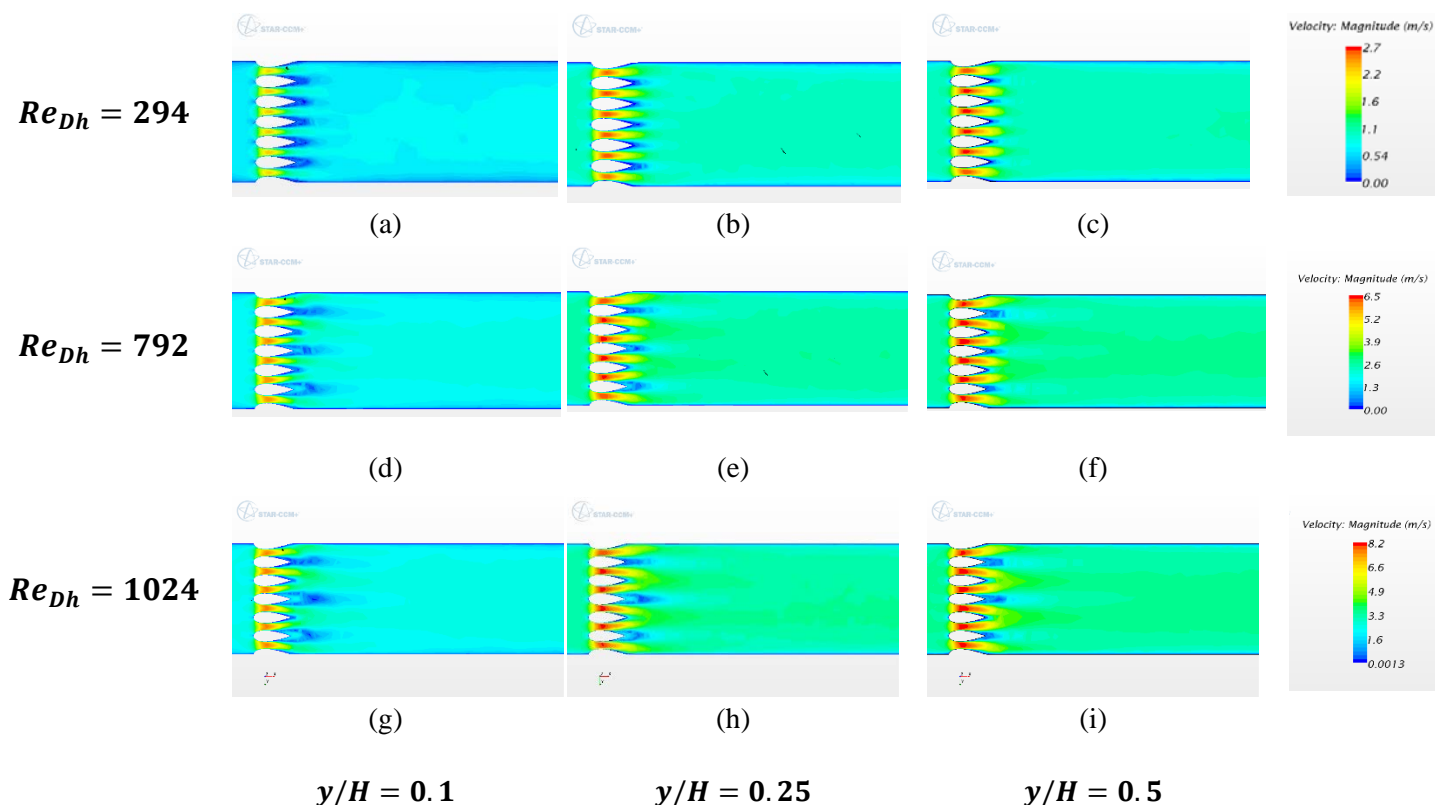
Figure 45: Mean velocity magnitude contour in the vicinity of the pin fins at various vertical distances from the heater surface (y/H); (a), (b) and (c) are for steady state, and the rest of the contours were averaged over 20000 time steps.

8.2.2.   **Temperature measurements**

Experimental heat transfer was based on hydrofoil micro device as it shows better RTD measurement repeatability compared to the circular case and the result for six RTDs were presented here. Figure 46 shows the temperature difference (ΔT) versus heat fluxes for six Reynolds number of 294, 361, 493, 626, 792 and 1024.The electrical power source was increased in a 0.25 watts increments up to 2 watts. A decrease in ΔT was observed for all RTDs with increasing Reynolds number — a result of enhanced mixing as the flow regime developed with the Reynolds number and in the process enhanced flow mixing and advection heat transfer. For all Reynolds numbers, a maximum temperature difference, implying a minimum heat transfer coefficient, was observed for RTD 1 located at the farthest distance from the pin fins $(x/D = 8)$ with a

lateral distance of $y/D = 0.5$. For all the Reynolds numbers except $Re_{Dh} = 361,493$, the minimum temperature difference was observed for RTD 6, the closest to the pin fins. For the Reynold numbers of $Re_{Dh} = 361,493$, the lowest ΔT, corresponding to the highest heat transfer coefficient, was observed for RTD2. This behavior may suggests that vortex shedding started to develop around a Reynolds number of 400, similar to the result of Jung et al. [99] who demonstrated that global flow instability downstream a micro scale pin fin inside a confined microchannel occurs around Re=400 .
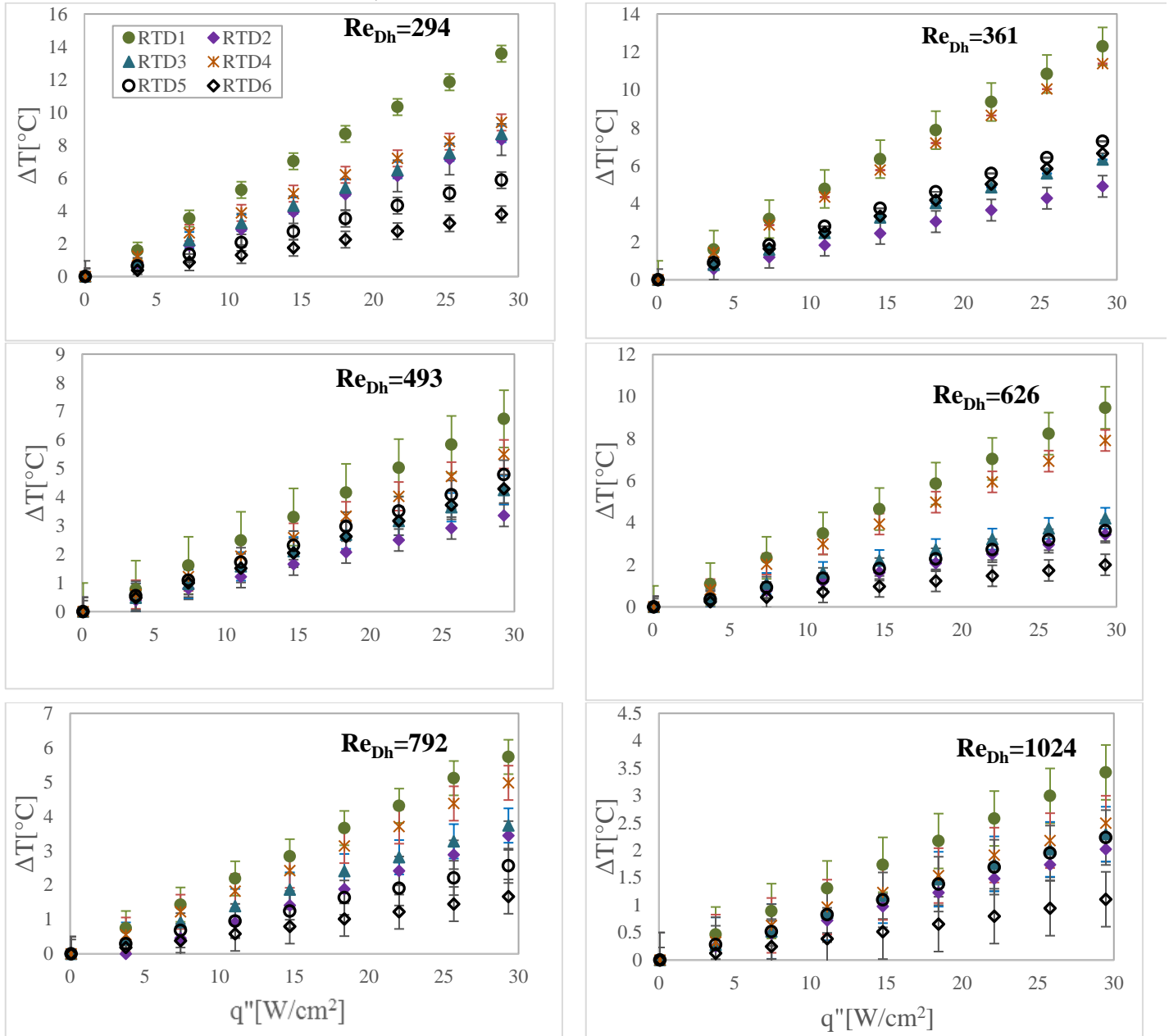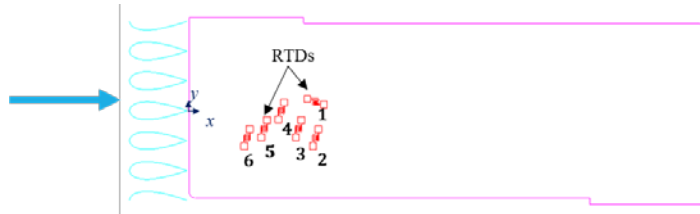
Figure 46: Temperature difference (ΔT) as a function of heat fluxes in 6 *RTD* locations for six Reynolds numbers. ΔT was defined as the difference of RTD temperature and inlet bulk temperature.

Figure 47 shows heat transfer coefficient at various RTDs. For all Reynolds numbers, maximum heat transfer coefficient was seen to occur in $x/C = 1,$ the closest RTD to the pin fins array. The trend is more evident at higher Reynolds numbers($Re_{Dh} \geq 696$). As vortex shedding initiated the flow structure near the hydrofoils' trailing edges altered leading to enhanced heat transfer process near the pin fins.
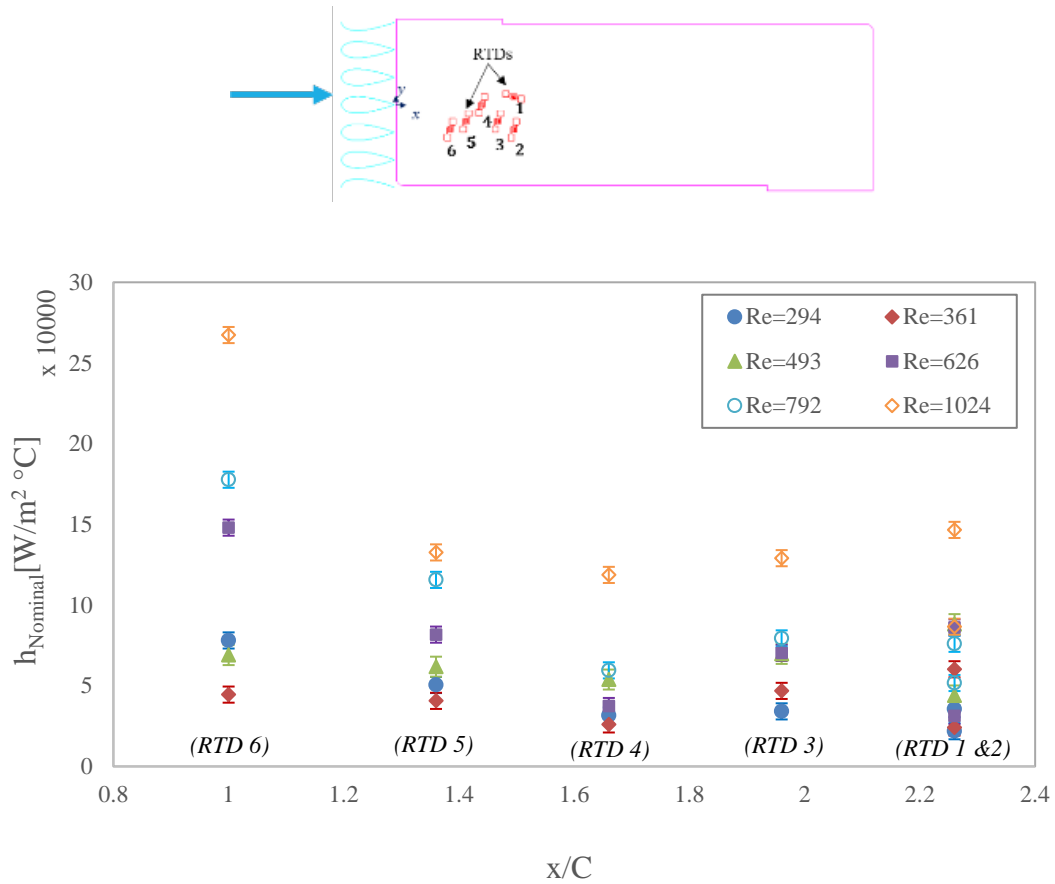
Figure 47: Heat transfer coefficient as a function of location as a function of the Reynolds number.

8.2.2.1. Numerical validation

The numerical model was validated by comparing the results of the temperature difference with experimental measurements for $Re_{Dh} = 792$ (Figure 48). The numerical simulation predicted the temperature difference trend of the RTDs with an average over-prediction of $\Delta T = 15\%$ including the measurement uncertainty. It is believed that this is partly due to the adiabatic boundary condition assumption made for SU-8 and the top Pyrex wall and by elimination the sticker and top Pyrex substrates in the numerical simulation.
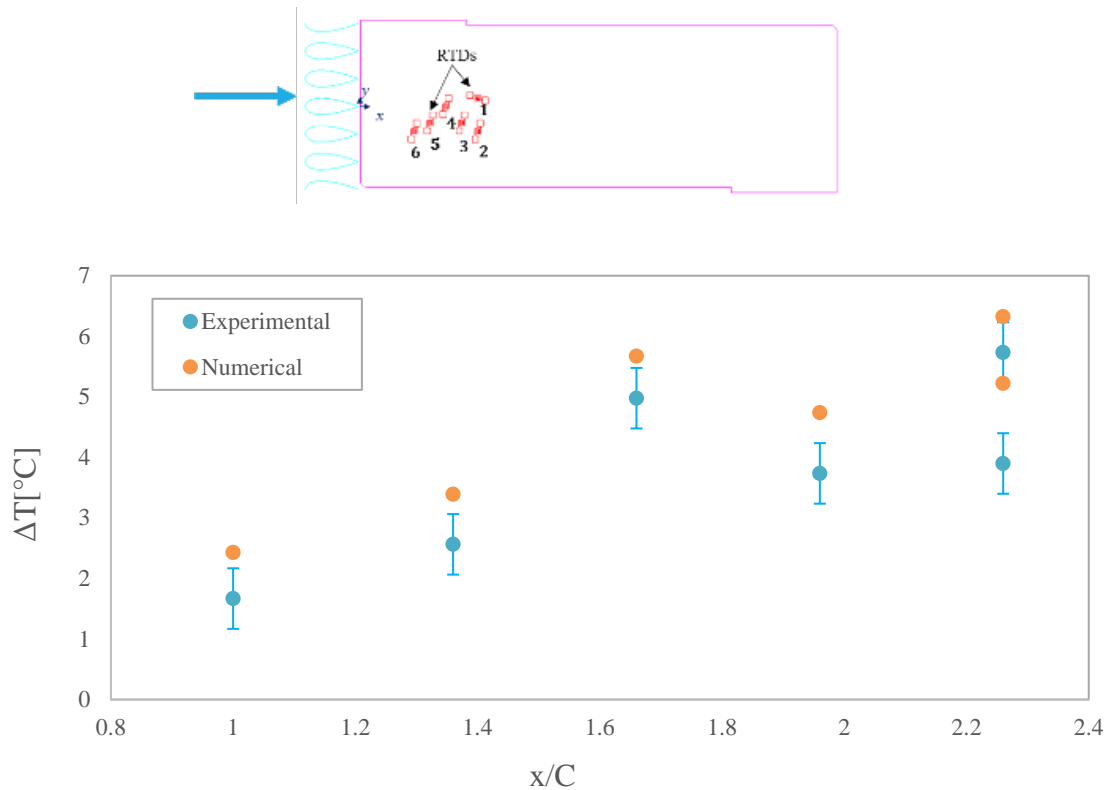
Figure 48: Numerical and experimental comparison of temperature difference as a function of the downstream positions for $Re_{Dh} = 792$.

8.2.2.2. Comparison of circular and hydrofoil configurations

Experimentally obtained heat transfer coefficient for circular and hydrofoil pin fins were compared (Figure 49). The comparison was conducted at 4 RTDs locations since not all the RTDs for the circular case generated repeatable data. In both configurations, the highest heat transfer coefficient was measured at RTD6. For $x/D \leq 6,$ the heat transfer coefficient for the circular pin fins outperform the hydrofoils. For $Re_{Dh} = 294$, the heat transfer coefficient trend was similar for the two configurations, indicating no vortex shedding at this low Reynolds number.
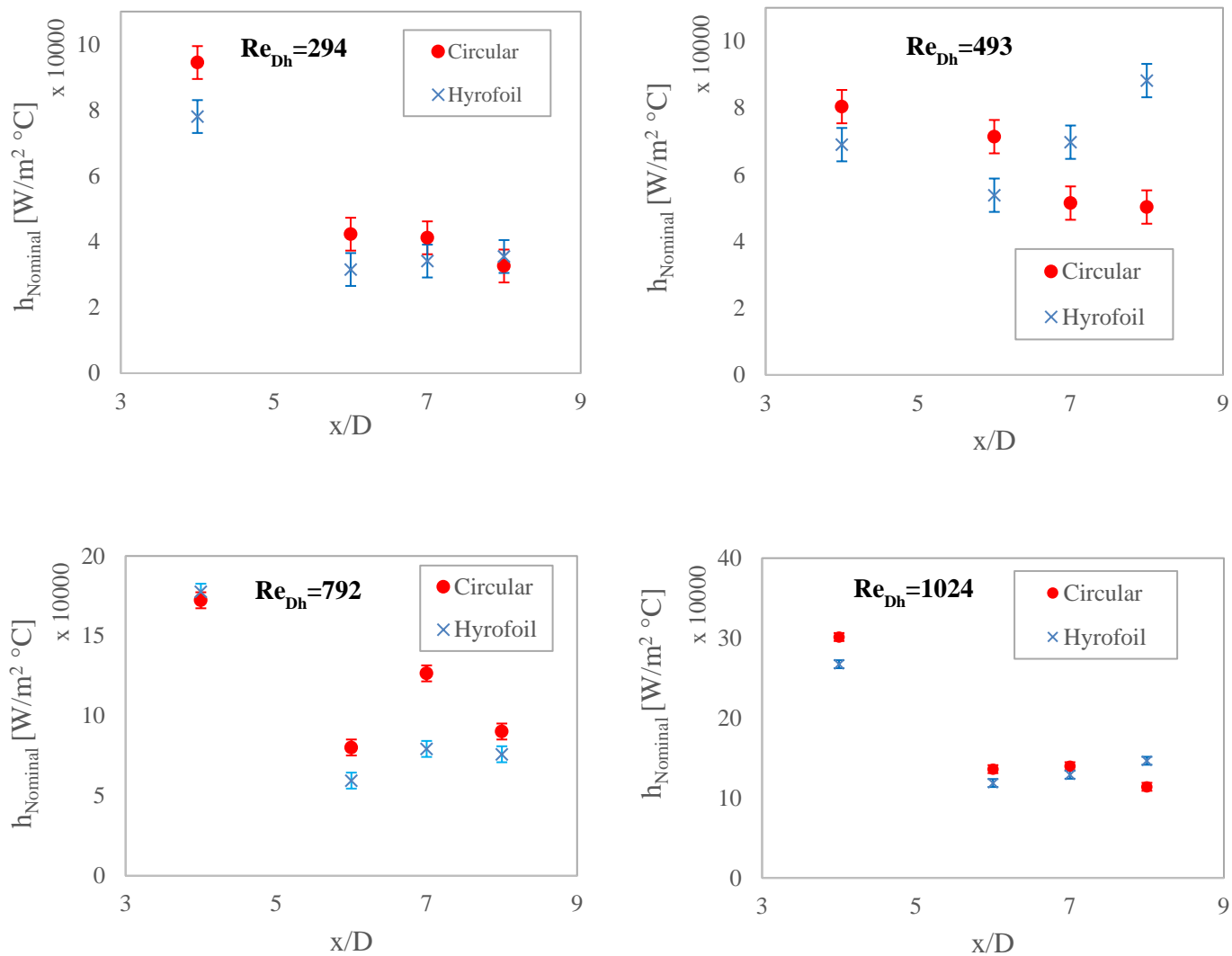
Figure 49: Comparison of heat transfer coefficient between circular and hydrofoil configurations

9. SUMMARY AND CONCLUSION

9.1. Cavitation study

Measurements and flow visualizations were conducted to characterize hydrodynamic cavitation downstream various micro pillars entrenched in a microchannel. The experiments were carried out using distilled water in an open fluid loop under various flow conditions. The inception mechanism of the cavities were explored for different configurations and similarities and deviations were discussed and compared among micro scale constriction elements and their macro scale counterparts. A special inception mode accompanied by high inception cavitation numbers was detected for the triangular configuration that is postulated to be linked to its wake region vortical structures. The cavity dimensions including average cavity length and its attachment angle were measured and compared for each configuration. Triangular pillar had the longest cavity. Configurations with sharp corners led to lower cavity attachment angles close to the flow separation vertex while circular micro pillars resulted in higher angles. For twin circles, the flow patterns were presented and the cavities synchronization mode were analyzed by investigating high speed images. Image processing were performed on the image pixel intensity via FFT and the dominant cavitation frequency were detected for circular, triangular and diamond pillars. Confinement effect is believed to be associated with lower Strouhal number for vortex shedding and cavitation pulsations. The lowest Strouhal numbers were obtained for sharp-edged pillars, which may be an indication of increased suppression effects of vortical structure and cavity interactions at the micro scale.

9.2. Heat transfer

This study explored single-phase fluid flow and heat transfer through a single row circular and hydrofoil pin fin configurations for distilled water in a microchannel. Using a combination of local temperature measurements downstream the pin fins and conjugate fluid / thermal numerical modeling, the prevailing

flow structure was revealed including vortex shedding in the vicinity of pin fins. These were linked to the

local heat transfer coefficients. Key findings are summarized below:

(1) The flow pattern for both circular and hydrofoil pin fins were dominated by the occurrence of vortex shedding at $Re_{Dh} > 294$. The crosswise distance among the pin fins yielded an especial type of flow filed called biased flow. The flow issuing from the gap between the pin fins tilted, resulting in a wakes of two types — one with a narrow and short wake region and another with a wider and longer one.

(2) Result of local heat transfer measurement for the hydrofoil pin fin revealed an appreciable heat transfer enhancement influence in the vicinity of pin fin array. With increasing Reynolds numbers, the heat transfer enhanced as a result of the inception of vortex shedding.

(3) Comparison between the numerical model and experimental measurements showed good agreements and the numerical scheme was able to capture most prominent features of the flow filed and heat transfer process.

(4) Local heat transfer coefficient measurements showed that the circular pin fin configuration outperformed the hydrofoil pin fin in most locations. This is believed to be a result of a stronger gap flow and vortex shedding in the circular pin fins.

10. FUTURE WORK

The current study focused on exploring the hydrodynamic characteristics of cavitation including cavitation inception toward elongated cavity on micro pin fins. Because cavitation is in the form of two-phase flow, it can have favorable effect on heat transfer. To further study this hypothesis, the current research can be extended to heat transfer measurements to evaluate the influence of hydrodynamic cavitation on heat transfer enhancement. Another plausible work can be conducting numerical modeling on cavitation, this would be result in a more realistically simulation and provide more useful results for comparison to the flow visualization.

For the second part on single-phase fluid flow and heat transfer over a single-row micro pin fins, boiling experiments can be carried out. Preheater can be used to bring the water to near-saturation temperatures. When high temperature water enters the microchannel, the heater can boil water inside the microchannel. Available local temperatures coupled with video synchronization would enable the realization of boiling regimes.

REFERENCES

[1]   A. Gnanaskandan, Development of a methodology for LES of Turbulent Cavitating Flows, 2015.

[2]   C.E. Brennen, Cavitation and bubble dynamics, Oxford University Press, 1995. doi:10.1017/CBO9781107338760.

[3]   C. Mishra, Y. Peles, Cavitation in flow through a micro-orifice inside a silicon microchannel, Phys. Fluids. 17 (2005) 013601. doi:10.1063/1.1827602.

[4]   S. Pennathur, Micro-scale turbopump blade cavitation, Massachusetts Institute of Technology, 2001.

[5]   M.R. Soltani, F. Askari, A.R. Davari, A. Nayebzadeh, Effects of canard position on wing surface pressure, Sci. Iran. 17 (2010).

[6]   H. Ganesh, J. Schot, S.L. Ceccio, Stationary cavitation bubbles forming on a delta wing vortex, Phys. Fluids. 26 (2014). doi:10.1063/1.4903204.

[7]   B. Schneider, A. Koşar, C.-J. Kuo, C. Mishra, G.S. Cole, R.P. Scaringe, Y. Peles, Cavitation Enhanced Heat Transfer in Microchannels, J. Heat Transfer. 128 (2006) 1293. doi:10.1115/1.2349505.

[8]   B. Schneider, A. Koşar, Y. Peles, Hydrodynamic cavitation and boiling in refrigerant (R-123) flow inside microchannels, Int. J. Heat Mass Transf. 50 (2007) 2838–2854. doi:10.1016/j.ijheatmasstransfer.2007.01.002.

[9]   A. Koşar, M. Şeşen, O. Oral, Z. Itah, D. Gozuacik, Bubbly cavitating flow generation and investigation of its erosional nature for biomedical applications, IEEE Trans. Biomed. Eng. 58 (2011) 1337–1346. doi:10.1109/TBME.2011.2107322.

[10]   O.Y. Perk, M. Şeşen, D. Gozuacik, A. Koşar, Kidney stone erosion by micro scale hydrodynamic cavitation and consequent kidney stone treatment, Ann. Biomed. Eng. 40 (2012) 1895–1902. doi:10.1007/s10439-012-0559-7.

[11]   Z. Itah, O. Oral, O.Y. Perk, M. Sesen, E. Demir, S. Erbil, A.I. Dogan-Ekici, S. Ekici, A. Kosar, D. Gozuacik, Hydrodynamic cavitation kills prostate cells and ablates benign prostatic hyperplasia tissue., Exp. Biol. Med. (Maywood). 238 (2013) 1242–50. doi:10.1177/1535370213503273.

[12]   P. Prentice, A. Cuschieri, K. Dholakia, M. Prausnitz, P. Campbell, Membrane disruption by optically controlled microbubble cavitation, Nat. Phys. 1 (2005) 107–110. doi:10.1038/nphys148.

[13]   P.R. Gogate, A.B. Pandit, A review and assessment of hydrodynamic cavitation as a technology for the future, in: Ultrason. Sonochem., 2005: pp. 21–27. doi:10.1016/j.ultsonch.2004.03.007.

[14]   A.G. Chakinala, D.H. Bremner, P.R. Gogate, K.C. Namkung, A.E. Burgess, Multivariate analysis of phenol mineralisation by combined hydrodynamic cavitation and heterogeneous advanced Fenton processing, Appl. Catal. B Environ. 78 (2008) 11–18. doi:10.1016/j.apcatb.2007.08.012.

[15]   A.G. Chakinala, P.R. Gogate, A.E. Burgess, D.H. Bremner, Treatment of industrial wastewater effluents using hydrodynamic cavitation and the advanced Fenton process, Ultrason. Sonochem. 15 (2008) 49–54. doi:10.1016/j.ultsonch.2007.01.003.

[16]   S.S. Sawant, A.C. Anil, V. Krishnamurthy, C. Gaonkar, J. Kolwalkar, L. Khandeparker, D. Desai, A.V. Mahulkar, V.V. Ranade, A.B. Pandit, Effect of hydrodynamic cavitation on zooplankton: A tool for disinfection, Biochem. Eng. J. 42 (2008) 320–328. doi:10.1016/j.bej.2008.08.001.

[17]   P.R. Gogate, A.M. Kabadi, A review of applications of cavitation in biochemical engineering/biotechnology, Biochem. Eng. J. 44 (2009) 60–72. doi:10.1016/j.bej.2008.10.006.

[18]   M. Zupanc, T. Kosjek, M. Petkovšek, M. Dular, B. Kompare, B. Širok, Ž. Blažeka, E. Heath, Removal of pharmaceuticals from wastewater by biological processes, hydrodynamic cavitation and UV treatment, Ultrason. Sonochem. 20 (2013) 1104–1112. doi:10.1016/j.ultsonch.2012.12.003.

[19]   P.R. Gogate, Hydrodynamic Cavitation for Food and Water Processing, Food Bioprocess Technol. 4 (2010) 996–1011. doi:10.1007/s11947-010-0418-1.

[20]   J. Ji, J. Wang, Y. Li, Y. Yu, Z. Xu, Preparation of biodiesel with the help of ultrasonic and hydrodynamic cavitation, Ultrasonics. 44 (2006). doi:10.1016/j.ultras.2006.05.020.

[21]   B.R. Parkin, Scale Effects in Cavitating Flow, California Institute of Technology, 1952.

[22]   Y. Kuhn, D. Chizelle, S.L. Ceccio, C.E. Brennen, Observation and Scaling of Travelling Buble Cavitation, J. Fluid Mech. 293 (1995) 99–126. doi:10.1017/S0022112095001650.

[23]   A.P. Keller, Cavitation Scale Effects Empirically Found Relations and the Correlation of Cavitation Number and Hydrodynamic Coefficients, Cav2001. (2001) 1–18.

[24]   E.L. Amromin, Scale Effect of Cavitation Inception on a 2D Eppler Hydrofoil, J. Fluids Eng. 124 (2002) 186–193. doi:10.1115/1.1427689.

[25]   C.-T. Hsiao, G.L. Chahine, H.-L. Liu, Scaling Effect on Prediction of Cavitation Inception in a Line Vortex Flow, J. Fluids Eng. 125 (2003) 53. doi:10.1115/1.1521956.

[26]   M. Dular, I. Khlifa, S. Fuzier, M. Adama Maiga, O. Coutier-Delgosha, Scale effect on unsteady cloud cavitation, Exp. Fluids. 53 (2012) 1233–1250. doi:10.1007/s00348-012-1356-7.

[27]   C. Ho, Y. Tai, Micro-Electro-Mechanical- Systems (Mems) and Fluid, (1998) 579–612.

[28]   H.A. Stone, A.D. Stroock, A. Ajdari, Engineering flows in small devices: Microfluidics toward a Lab-on-a-Chip, Annu. Rev. Fluid Mech. 36 (2004) 381–411. doi:doi:10.1146/annurev.fluid.36.050802.122124.

[29]   S. Krishnamurthy, Y. Peles, Flow boiling of water in a circular staggered micro-pin fin heat sink, Int. J. Heat Mass Transf. 51 (2008) 1349–1364. doi:10.1016/j.ijheatmasstransfer.2007.11.026.

[30]   K. V. Sharp, R.J. Adrian, J.G. Santiago, J.I. Molho, Liquid Flows in Microchannels, MEMS Handb. (2002) 6.1–6.38. doi:doi:10.1201/9781420036572.ch10.

[31]   M. Medrano, P.J. Zermatten, C. Pellone, J.P. Franc, F. Ayela, Hydrodynamic cavitation in microsystems. I. Experiments with deionized water and nanofluids, Phys. Fluids. 23 (2011) 127103. doi:10.1063/1.3671682.

[32] Y. Peles, Cavitation in Microdomains, in: Encycl. Microfluid. Nanofluidics, 2008: pp. 197–201.

[33] A. Bamshad, H.J. Cho, Digital microfabrication on paper and cloth For heavy metal detection and remediation, in: Transducers 2019 - EUROSENSORS XXXIII, 20th Int. Conf. Solid-State Sensors, Actuators Microsystems, Berlin, Germany, 2019.

[34] A. Bamshad, A. Nikfarjam, M.H. Sabour, H. Raji, Theoretical and Numerical Investigation of Liquid- Gas Interface Location of Capillary Driven Flow During the Time Throughout Circular Microchannels, 2017 5th RSI Int. Conf. Robot. Mechatronics. (2017) 432–438.

[35] A. Bamshad, A. Nikfarjam, M.H. Sabour, Capillary-based micro-optofluidic, Meas. Sci. Technol. 29 (2018).

[36] A. Karbalaei, R. Kumar, H.J. Cho, Thermocapillarity in Microfluidics — A Review, Micromachines. 7 (2016). doi:10.3390/mi7010013.

[37] A. Karbalaei, H.J. Cho, Microfluidic Devices Developed for and Inspired by Thermotaxis and Chemotaxis, Micromachines. 9 (2018). doi:10.3390/mi9040149.

[38] A. Karbalaei, K. Hejranfar, A Central Difference Finite Volume Lattice Boltzmann Method for Simulation of 2D Inviscid Compressible Flows on Triangular Meshes, in: ASME Int. Mech. Eng. Congr. Expo., Pittsburgh, Pennsylvania, USA, 2018.

[39] C. Mishra, Y. Peles, Flow visualization of cavitating flows through a rectangular slot micro-orifice ingrained in a microchannel, Phys. Fluids. 17 (2005) 1–14. doi:10.1063/1.2132289.

[40] C. Mishra, Y. Peles, An experimental investigation of hydrodynamic cavitation in micro-Venturis, Phys. Fluids. 18 (2006) 103603. doi:10.1063/1.2360996.

[41] M. Medrano, C. Pellone, P.J. Zermatten, F. Ayela, Hydrodynamic cavitation in microsystems. II. Simulations and optical observations, Phys. Fluids. 24 (2012) 047101. doi:10.1063/1.3699067.

[42] T. Gothsch, C. Schilcher, C. Richter, S. Beinert, A. Dietzel, S. Buttgenbach, A. Kwade, High-pressure microfluidic systems (HPMS): flow and cavitation measurements in supported silicon microsystems, Microfluid. Nanofluidics. 18 (2015) 121–130. doi:10.1007/s10404-014-1419-6.

[43] M. Schlender, A. Spengler, H.P. Schuchmann, High-pressure emulsion formation in cylindrical coaxial orifices: Influence of cavitation induced pattern on oil drop size, Int. J. Multiph. Flow. 74 (2015) 84–95. doi:10.1016/j.ijmultiphaseflow.2015.04.004.

[44] A. Cioncolini, F. Scenini, J. Duff, M. Szolcek, M. Curioni, Choked cavitation in micro-orifices : An experimental study, Exp. Therm. Fluid Sci. 74 (2016) 49–57. doi:10.1016/j.expthermflusci.2015.12.004.

[45] M.G. De Giorgi, A. Ficarella, M. Tarantino, Evaluating cavitation regimes in an internal orifice at different temperatures using frequency analysis and visualization, Int. J. Heat Fluid Flow. 39 (2013) 160–172. doi:10.1016/j.ijheatfluidflow.2012.11.002.

[46] M.G. De Giorgi, A. Ficarella, A. Lay-ekuakille, S. Member, Monitoring Cavitation Regime From Pressure and Optical Sensors : Comparing Methods Using Wavelet Decomposition for Signal Processing, IEEE Sens. J. 15 (2015) 4684–4691. doi:10.1109/JSEN.2015.2427369.

[47] M.G. De Giorgi, A. Ficarella, A. Lay-ekuakille, S. Member, Cavitation Regime Detection by LS-SVM and ANN With Wavelet Decomposition Based on Pressure Sensor Signals, IEEE Sens. J. 15

(2015) 5701–5708. doi:10.1109/JSEN.2015.2447518.

[48]   C.H.K. Williamson, Vortex Dynamics in the Cylinder Wake, Annu. Rev. Fluid Mech. 28 (1996) 477–539. doi:10.1146/annurev.fl.28.010196.002401.

[49]   M.M. Zdravkovich, Flow around circular cylinders, Vol. 1, Oxford University Press, 1997.

[50]   J. Jung, C.-J. Kuo, Y. Peles, M. Amitay, The flow field around a micropillar confined in a microchannel, Int. J. Heat Fluid Flow. 36 (2012) 118–132. doi:10.1016/j.ijheatfluidflow.2012.04.009.

[51]   Y. Peles, A. Koşar, C. Mishra, C.J. Kuo, B. Schneider, Forced convective heat transfer across a pin fin micro heat sink, Int. J. Heat Mass Transf. 48 (2005) 3615–3627. doi:10.1016/j.ijheatmasstransfer.2005.03.017.

[52]   A. Koşar, C. Mishra, Y. Peles, Laminar Flow Across a Bank of Low Aspect Ratio Micro Pin Fins, J. Fluids Eng. 127 (2005) 419–430. doi:10.1115/1.1900139.

[53]   A. Kosar, Y. Peles, Thermal-Hydraulic Performance of MEMS-based Pin Fin Heat Sink, J. Heat Transfer. 128 (2006) 121–131. doi:10.1115/1.2137760.

[54]   A. Koşar, Y. Peles, Boiling heat transfer in a hydrofoil-based micro pin fin heat sink, Int. J. Heat Mass Transf. 50 (2007) 1018–1034. doi:10.1016/j.ijheatmasstransfer.2006.07.032.

[55]   A. Kosar, Y. Peles, Micro Scale pin fin Heat Sinks — Parametric Performance Evaluation Study, Components Packag. Technol. 30 (2007) 1–11. doi:10.1109/TCAPT.2007.906334.

[56]   A. Kosar, Y. Peles, Micro scale pin fin heat sinks -Parametric performance evaluation study, IEEE Trans. Components Packag. Technol. 30 (2007) 855–865. doi:10.1109/TCAPT.2007.906334.

[57]   S. Krishnamurthy, Y. Peles, Flow Boiling Heat Transfer on Micro Pin Fins Entrenched in a Microchannel, J. Heat Transfer. 132 (2010) 41007. doi:10.1115/1.4000878.

[58]   Y. Wang, F. Houshmand, D. Elcock, Y. Peles, Convective heat transfer and mixing enhancement in a microchannel with a pillar, Int. J. Heat Mass Transf. 62 (2013) 553–561. doi:10.1016/j.ijheatmasstransfer.2013.03.034.

[59]   A. Gnanaskandan, K. Mahesh, Numerical investigation of near-wake characteristics of cavitating flow over a circular cylinder, J. Fluid Mech. 790 (2016) 453–491. doi:10.1017/jfm.2016.19.

[60]   S.A. Fry, Investigating cavity/wake dynamics for a circular cylinder by measuring noise spectra, J. Fluid Mech. 142 (1984) 187–200. doi:10.1017/S0022112084001051.

[61]   J. Varga, G. Sebestyen, Experimental investigation of cavitation noise, La Houille Blanche 8. (1966) 905–910.

[62]   J. Varga, G. Sebestyen, A. Fay, Detection of cavitation by acoustic and vibration-measurement methods, La Houille Blanche. (1969) 137–150. doi:10.1051/lhb/1969012.

[63]   V.H. Arakeri, Viscous effects on the position of cavitation separation from smooth bodies, J. Fluid Mech. 68 (1975) 779–799. doi:10.1017/S0022112075001231.

[64]   B.C. Syamala Rao, D. V. Chandrasekhara, Some Characteristics of Cavity Flow Past Cylindrical Inducers in a Venturi _ Journal of Fluids Engineering _ ASME DC, J. Fluids Eng. 98 (1976) 461–

466. doi:doi:10.1115/1.3448368.

[65] A. Ramamurthy, P. Bhaskaran, Constrained Flow Past Cavitating Bluff Bodies _ Journal of Fluids Engineering _ ASME DC, J. Fluid Eng. 99 (1977) 717–726. doi:doi:10.1115/1.3448892.

[66] Y. Matsudaira, Y. Gomi, R. Oba, Characteristics of Bubble-Collapse Pressures in Karman-Vortex Cavity, JSME Int. J. 35 (1992) 179–185. doi:10.1299/kikaib.57.843.

[67] A. Tassin Leger, L.P. Bernal, S.L. Ceccio, Examination of the flow near the leading edge of attached cavitation. Part 1. Detachment of two-dimensional and axisymmetric cavities, J. Fluid Mech. 376 (1998) 61–90. doi:10.1017/S0022112098002778.

[68] P. a. Brandner, G.J. Walker, P.N. Niekamp, B. Anderson, An experimental investigation of cloud cavitation about a sphere, J. Fluid Mech. 656 (2010) 147–176. doi:10.1017/S0022112010001072.

[69] P. Kumar, D. Chatterjee, S. Bakshi, Experimental investigation of cavitating structures in the near wake of a cylinder, Int. J. Multiph. Flow. 89 (2017) 207–217. doi:10.1016/j.ijmultiphaseflow.2016.09.025.

[70] S.G. Kandlikar, S. Colin, Y. Peles, S. Garimella, R.F. Pease, J.J. Brandner, D.B. Tuckerman, Heat Transfer in Microchannels—2012 Status and Research Needs, J. Heat Transfer. 135 (2013) 091001. doi:10.1115/1.4024354.

[71] A. Koşar, Y. Peles, Thermal-Hydraulic Performance of MEMS-based Pin Fin Heat Sink, J. Heat Transfer. 128 (2006) 121. doi:10.1115/1.2137760.

[72] A. Kosar, Y. Peles, TCPT-2006-096. R2: micro scale pin fin heat sinks—Parametric performance evaluation study, Components Packag. Technol. …. 30 (2007) 855–865. http://ieeexplore.ieee.org/xpls/abs_all.jsp?arnumber=4358424.

[73] H. Tabkhi, A. Nayebzadeh, Y. Peles, Effect of Micropillar with Free-End on Heat Transfer, in: 16th IEEE Intersoc. Conf. Therm. Phenom. Electron. Syst., 2017.

[74] A. Bar-Cohen, P. Wang, Thermal Management of On-Chip Hot Spot, J. Heat Transfer. 134 (2012) 051017. doi:10.1115/1.4005708.

[75] D. Ansari, K.Y. Kim, Hotspot thermal management using a microchannel-pinfin hybrid heat sink, Int. J. Therm. Sci. 134 (2018) 27–39. doi:10.1016/j.ijthermalsci.2018.07.043.

[76] A.F. Al-Neama, N. Kapur, J. Summers, H.M. Thompson, Thermal management of GaN HEMT devices using serpentine minichannel heat sinks, Appl. Therm. Eng. 140 (2018) 622–636. doi:10.1016/j.applthermaleng.2018.05.072.

[77] S. Adera, D.S. Antao, R. Raj, E.N. Wang, Hotspot Thermal Management via Thin-Film Evaporation—Part II: Modeling, IEEE Trans. Components, Packag. Manuf. Technol. 8 (2018) 99–112. doi:10.1109/TCPMT.2017.2757461.

[78] M. Ahadi, M. Tam, M.S. Saha, J. Stumper, M. Bahrami, Thermal conductivity of catalyst layer of polymer electrolyte membrane fuel cells: Part 1 – Experimental study, J. Power Sources. 354 (2017) 207–214. doi:10.1016/j.jpowsour.2017.02.016.

[79] Q. Wang, B. Jiang, B. Li, Y. Yan, A critical review of thermal management models and solutions of lithium-ion batteries for the development of pure electric vehicles, Renew. Sustain. Energy Rev. 64 (2016) 106–128. doi:10.1016/j.rser.2016.05.033.

[80]   B. Ramos-Alvarado, P. Li, H. Liu, A. Hernandez-Guerrero, CFD study of liquid-cooled heat sinks with microchannel flow field configurations for electronics, fuel cells, and concentrated solar cells, Appl. Therm. Eng. 31 (2011) 2494–2507. doi:10.1016/j.applthermaleng.2011.04.015.

[81]   M. Ghorbani, O. Oral, S. Ekici, D. Gozuacik, A. Kosar, Review on Lithotripsy and Cavitation in Urinary Stone Therapy, IEEE Rev. Biomed. Eng. 3333 (2016) 1–1. doi:10.1109/RBME.2016.2573381.

[82]   Z. Itah, O. Oral, O.Y. Perk, M. Sesen, E. Demir, S. Erbil, A.I. Dogan-Ekici, S. Ekici, A. Kosar, D. Gozuacik, Hydrodynamic cavitation kills prostate cells and ablates benign prostatic hyperplasia tissue., Exp. Biol. Med. (Maywood). 238 (2013) 1242–50. doi:10.1177/1535370213503273.

[83]   T.E. Sarvey, Y. Hu, C.E. Green, P.A. Kottke, D.C. Woodrum, Y.K. Joshi, A.G. Fedorov, S.K. Sitaraman, M.S. Bakir, S. Member, Micropin-Fin Arrays for Nonuniform Power Maps, IEEE Trans. Components, Packag. Manuf. Technol. 7 (2017) 1465–1475.

[84]   A. Mohammadi, A. Kosar, Hydrodynamic and Thermal Performance of Microchannels With Different Staggered Arrangements of Cylindrical Micro Pin Fins, 139 (2019) 1–14. doi:10.1115/1.4035655.

[85]   M. Koz, M. Rafet, A. Kosar, Parametric study on the effect of end walls on heat transfer and fluid flow across a micro pin fi n, Int. J. Therm. Sci. 50 (2011). doi:10.1016/j.ijthermalsci.2010.12.008.

[86]   A. Mohammadi, A. Koşar, Review on Heat and Fluid Flow in Micro Pin Fin Heat Sinks under Single-phase and Two-phase Flow Conditions, Nanoscale Microscale Thermophys. Eng. 22 (2018) 153–197. doi:10.1080/15567265.2018.1475525.

[87]   C.R. Kharangate, K.W. Jung, S. Jung, D. Kong, J. Schaadt, M. Iyengar, C. Malone, H. Lee, M. Asheghi, K.E. Goodson, Experimental Investigation of Embedded Micropin-Fins for Single-Phase Heat Transfer and Pressure Drop, 140 (2018). doi:10.1115/1.4039475.

[88]   J. Mita, W. Qu, International Journal of Heat and Mass Transfer Pressure drop of water flow across a micro-pin – fin array part 1 : Isothermal liquid single-phase flow, Int. J. Heat Mass Transf. 89 (2015) 1073–1082. doi:10.1016/j.ijheatmasstransfer.2015.06.006.

[89]   W. Qu, I. Mudawar, Experimental and numerical study of pressure drop and heat transfer in a single-phase micro-channel heat sink, 45 (2002) 2549–2565.

[90]   H.Y. Zhang, D. Pinjala, T.N. Wong, K.C. Toh, Y.K. Joshi, Single-phase liquid cooled microchannel heat sink for electronic packages, Appl. Therm. Eng. 25 (2005) 1472–1487. doi:10.1016/j.applthermaleng.2004.09.014.

[91]   J. Harrington, A. Nayebzadeh, W. Wang, J. Winn, J. Kapat, M. Maurer, S. Thorpe, Effect of Target Wall Curvature on Heat Transfer and Pressure Loss From Jet Array Impingement, in: Proc. ASME Turbo Expo, Montreal, 2015: pp. 1–13. doi:10.1115/1.4035160.

[92]   E. Rasouli, C. Naderi, V. Narayanan, Pitch and aspect ratio effects on single-phase heat transfer through microscale pin fin heat sinks, Int. J. Heat Mass Transf. 118 (2018) 416–428. doi:10.1016/j.ijheatmasstransfer.2017.10.105.

[93]   C.R. Kharangate, K.W. Jung, S. Jung, D. Kong, J. Schaadt, M. Iyengar, C. Malone, H. Lee, M. Asheghi, K.E. Goodson, Experimental Investigation of Embedded Micropin-Fins for Single-Phase Heat Transfer and Pressure Drop, J. Electron. Packag. Trans. ASME. 140 (2018) 1–12.

doi:10.1115/1.4039475.

[94] A. Koşar, Y. Peles, Convective flow of refrigerant (R-123) across a bank of micro pin fins, Int. J. Heat Mass Transf. 49 (2006) 3142–3155. doi:10.1016/j.ijheatmasstransfer.2006.02.013.

[95] J.F. Tullius, T.K. Tullius, Y. Bayazitoglu, Optimization of short micro pin fins in minichannels, Int. J. Heat Mass Transf. 55 (2012) 3921–3932. doi:10.1016/j.ijheatmasstransfer.2012.03.022.

[96] Y. Wang, F. Houshmand, D. Elcock, Y. Peles, Convective heat transfer and mixing enhancement in a microchannel with a pillar, Int. J. Heat Mass Transf. 62 (2013) 553–561. doi:10.1016/j.ijheatmasstransfer.2013.03.034.

[97] Y. Wang, A. Nayebzadeh, X. Yu, J.-H. Shin, Y. Peles, Local heat transfer in a microchannel with a pin fin—experimental issues and methods to mitigate, Int. J. Heat Mass Transf. 106 (2016) 1191–1204. doi:10.1016/j.ijheatmasstransfer.2016.10.100.

[98] Y. Wang, Y. Peles, An Experimental Study of Passive and Active Heat Transfer Enhancement in Microchannels, 136 (2014) 1–11. doi:10.1115/1.4025558.

[99] J. Jung, C. Kuo, Y. Peles, M. Amitay, International Journal of Heat and Fluid Flow The flow field around a micropillar confined in a microchannel, Int. J. Heat Fluid Flow. 36 (2012) 118–132. doi:10.1016/j.ijheatfluidflow.2012.04.009.

[100] A. Nayebzadeh, Y. Wang, H. Tabkhi, J. Shin, Y. Peles, Cavitation behind a circular micro pin fin, Int. J. Multiph. Flow. 98 (2018) 67–78. doi:10.1016/j.ijmultiphaseflow.2017.08.012.

[101] R.J. Moffat, Describing the uncertainties in experimental results, Exp. Therm. Fluid Sci. 1 (1988) 3–17. doi:10.1016/0894-1777(88)90043-X.

[102] B. Belahadji, J.P. Franc, J.M. Michel, Cavitation in the rotational structures of a turbulent wake, J. Fluid Mech. 287 (1995) 383. doi:10.1017/S0022112095000991.

[103] A.S. Ramamurthy, R. Balanchandar, The Near Wake Characteristics of Cavitating Bluff Sources, J. Fluids Eng. 112 (1990) 492–495. doi:doi:10.1115/1.2909433.

[104] Y. Yan, R.B. Thorpe, Flow regime transitions due to cavitation in the flow through an orifice, Int. J. Multiph. Flow. 16 (1990) 1023–1045. doi:10.1016/0301-9322(90)90105-R.

[105] R.W. Kermeen, B.R. Parkin, Incipient cavitation and wake flow behind sharp-edged disks, Pasadena, 1957.

[106] Ramamurthy, Bhaskaran, Constrained Flow past Cavitating Bluff Bodies, J. Fluids Eng. 99 (1977) 717–726. doi:doi:10.1115/1.3448892.

[107] W. Qu, G.M. Mala, D. Li, Heat transfer for water flow in trapezoidal silicon microchannels, Int. J. Heat Mass Transf. 43 (2000) 3925–3936. doi:10.1016/S0017-9310(00)00045-4.

[108] S. Vengallatore, Y. Peles, L.R. Arana, S.M. Spearing, Self-assembly of micro- and nanoparticles on internal micromachined silicon surfaces, Sensors Actuators, A Phys. 113 (2004) 124–131. doi:10.1016/j.sna.2004.03.066.

[109] Y. Saito, K. Sato, Cavitation bubble collapse and impact in the wake of a circular cylinder, in: Fifth Int. Symp. Cavitation (CAV 2003), Osaka, Japan, 2003.

[110] K. Sato, K. Kakutani, Measurements of cavitation inception, JSME Int. Journal. Ser. B. 37 (1994) 306–312. doi:10.1299/kikaib.58.1349.

[111] J.O. Young, J.W. Holl, Effects of Cavitation on Periodic Wakes Behind Symmetric Wedges, J. Basic Eng. 37 (1966) 163–176.

[112] J.W. Ball, J.P. Tullis, T. Stripling, Ball, J.W., Tullis, J.P. and Stripling, T., 1975. Predicting cavitation in sudden enlargements., J. Hydraul. Div. 101 (1975).

[113] J.-P. Franc, J.-M. Michel, Fundamentals of Cavitation, Springer, 2005.

[114] J.P. Franc, J.M. Michel, Attached cavitation and the boundary layer: experimental investigation and numerical treatment, J. Fluid Mech. 154 (1985) 63–90. doi:10.1017/S0022112085001422.

[115] D. Sumner, Two circular cylinders in cross-flow: A review, J. Fluids Struct. 26 (2010) 849–899. doi:10.1016/j.jfluidstructs.2010.07.001.

[116] C.H.K. Williamson, Evolution of a single wake behind a pair of bluff bodies, J. Fluids Mech. 159 (1985) 1–18. doi:10.1017/S002211208500307X.

[117] D. Sumner, S.S.T. Wong, S.J. Price, M.P. Paidoussis, Fluid behaviour of side-by-side curcular cylinders in steady cross-flow, 13 (1999) 309–338.

[118] M. Alam, M. Moriya, H. Sakamoto, Aerodynamic characteristics of two side-by-side circular cylinders and application of wavelet analysis on the switching phenomenon, 18 (2003) 325–346. doi:10.1016/j.jfluidstructs.2003.07.005.

[119] H. Tabkhi, A. Nayebzadeh, On the Distribution of Velocity Gradients, Viscosity and Reynolds Stresses in Varied Bed Elevation Turbulent Flow, in: APS Div. Fluid Dyn., Boston, MA, USA, 2015.

[120] G.L. Pankanin, The vortex flowmeter: various methods of investigating phenomena, Meas. Sci. Technol. 16 (2005) R1–R16. doi:10.1088/0957-0233/16/3/R01.

[121] A. Nayebzadeh, H. Tabkhi, Y. Peles, Hydrodynamic Cavitation Downstream a Micropillar Entrained Inside a Microchannel — A Parametric Study, ASME J. Fluids Eng. 141 (2019) 1–13. doi:10.1115/1.4040374.

[122] A. Nayebzadeh, H. Tabkhi, Y. Wang, Y. Peles, Study of Cavitation Phenomenon for a Micro Pillar in a channel, in: Second Therm. Fluids Eng. Conf., Las Vegas, NV, USA, 2017.

[123] M. Carini, F. Giannetti, F. Auteri, On the origin of the flip-flop instability of two side-by-side cylinder wakes, J. Fluid Mech. 742 (2014) 552–576. doi:10.1017/jfm.2014.9.

[124] J. Thapa, M. Zhao, L. Cheng, T. Zhou, Three-dimensional simulations of flow past two circular cylinders in side-by-side arrangements at right and oblique attacks, J. Fluids Struct. 55 (2015) 64–83. doi:10.1016/j.jfluidstructs.2015.02.003.

[125] X.D. Bai, W. Zhang, A.X. Guo, Y. Wang, The flip-flopping wake pattern behind two side-by-side circular cylinders: A global stability analysis, Phys. Fluids. 28 (2016). doi:10.1063/1.4944685.

[126] B.L. da Silva, R.D. Luciano, J. Utzig, H.F. Meier, Flow patterns and turbulence effects in large cylinder arrays, Int. J. Heat Fluid Flow. 69 (2018) 136–149. doi:10.1016/j.ijheatfluidflow.2017.12.013.

[127] P. Ausoni, Turbulent Vortex Shedding from a Blunt Trailing Edge Hydrofoil, EPFL, 2009.

[128] D.A. Bourgoyne, S.L. Ceccio, D.R. Dowling, Vortex shedding from a hydrofoil at high Reynolds number, 531 (2005) 293–324. doi:10.1017/S0022112005004076.